Effect of FRCM Repair on the Bond Behavior of Corroded Reinforced Concrete Beams Subjected to Static and Cyclic Loading

A THESIS
SUBMITTED TO THE FACULTY OF
UNIVERSITY OF MINNESOTA
BY

MIRANDA ANDERSON

IN PARTIAL FULFILLMENT OF THE REQUIREMENTS
FOR THE DEGREE OF
MASTER OF SCIENCE

Dr. Rania Al-Hammoud

August 2017

Acknowledgements

I would like to acknowledge my family and my fiancé for their support and encouragement. You motivated me to continue through the many stressful times encountered during the research project. Thank you for listening to me talk endlessly about my work and for spending countless hours with me in the lab.

I would also like to thank my advisor, Dr. Rania Al-Hammoud, for her ongoing assistance, inspiration, and encouragement. Thank you for motivating me to work hard and complete this research. Your insight on the topic and comments during the review process were indispensable in writing this thesis. I would also like to thank my committee members, Dr. Manik Barman and Dr. Ona Egbue for their time spent in helping me work towards the completion of my degree.

I would like to thank Dr. David Saftner for his support in writing the essential Matlab code used to analyze my data. Your assistance was highly valuable to my progress during the analysis.

I would like to acknowledge and give special thanks to the Civil Engineering Department staff at the University of Minnesota Duluth for their support throughout this research and my academic career. From ordering materials and lab equipment to helping with final paperwork, I could not have done it without all of you.

Dedication

I dedicate this thesis to my biggest supporters: my parents, Keith and Luanne, my sisters, Krista and Laura, and my fiancé, Bryce for all of the support and encouragement throughout the years I spent on this research.

Abstract

Existing structures may become structurally deficient due to age, an increase in required load capacity, or exposure to certain environmental conditions. Replacing deficient structures is expensive; therefore, finding a way to effectively repair the damage caused by corrosion is desired. Fiber Reinforced Cementitious Matrix (FRCM) is an emerging method of repair in which the fibers are applied to the concrete surface with the use of a cementitious mortar.

The objective of this study was to evaluate the effectiveness of Fiber Reinforced Cementitious Matrix (FRCM) repair in improving the bond behaviour of corroded reinforced concrete beams under both static and fatigue loading. Thirty full-scale beams (10”x6”x78”) were constructed for analysis in this study. Six beams were left uncorroded to be used as control. The remaining twenty-four beams experienced an accelerated corrosion process. The variables used in this study were corrosion level based on mass loss, repair method used, type of loading (monotonic or repeated loading), and load range applied.

Corrosion was found to reduce the fatigue strength of reinforced concrete beams by introducing internal stresses in the concrete that ultimately cause reduction in the bond between the reinforcement and the surrounding concrete. FRCM was found to increase the fatigue strength of corroded concrete beams by providing confinement, thus making it an effective method for repairing beams damaged from corrosion. The use of a cementitious substrate with FRCM allowed for easier monitoring of the cracks developed in the concrete while testing.

Table of Contents

List of Tables

List of Figures

Chapter 1 - Introduction

1.1 General

Reinforced concrete (RC) is a highly used composite material in the construction world due to it being both durable and cost-effective. Concrete is strong in compression, but weak in tension. Steel has high tensile strength; which makes it a great reinforcement for the concrete to increase its tensile capacity. It is essential that the bond between the reinforcement and the concrete be sufficient in order to transfer the load from the concrete to the steel effectively. The bond of reinforcement to concrete results from chemical adhesion, friction forces, and mechanical anchorage/bearing of ribs (ACI 408 2003). One of the major contributors to bond strength is confinement, either passive or active. Concrete cover and internal stirrups offer passive confinement, while external pressure offers active confinement. With insufficient confinement and short development length, the bond will fail in pullout due to the lack of shear resistance of the concrete between the ribs of the reinforcement (Choi 2010).

Corrosion is a major problem that leads to the deterioration of reinforced concrete structures. RC structures are often exposed to environmental conditions that promote corrosion in the steel reinforcement, which leads to cracking and reduced strength in the concrete member. Exposure to chloride ions can cause corrosion rates to increase significantly. Structures, such as bridges and parking garages, are commonly exposed to chloride ions through the presence of deicing salts. These structures endure cyclic loading from vehicles; therefore, the fatigue behavior needs to be assessed. Repeated loading causes material deterioration at a microscopic level, even at loads well below the

material's ultimate static capacity. In reinforced concrete, the bond of the reinforcement to the concrete can be deteriorated resulting in failure at load lower than the expected ultimate static capacity. (ACI 408, 2003).

Existing structures may become structurally deficient due to age, an increase in required load capacity, or exposure to certain environmental conditions. Replacing deficient structures is expensive; therefore, finding a way to repair a structure has become increasingly popular. Fiber reinforced polymer (FRP) repair has become increasingly popular over the past two decades. FRP involves adhering randomly arranged fibers to the concrete member using a polymer epoxy binder. Several issues have been discovered regarding FRP repair caused by its use of epoxy including compatibility to substrate, failure mode, and fire resistance. Fabric Reinforced Cement Matrix (FRCM) has been introduced as an alternative repair method that involves wrapping the concrete member in a fibrous grid that is adhered to the substrate using a cementitious matrix, which is generally a cement grout. The use of a cementitious material in place of the epoxy as a binder resolved the issues with the FRP repair method.

The present study investigated the effect of corrosion and confinement from fiber reinforced cementitious matrix (FRCM) on the bond behavior of reinforced concrete beams under monotonic and repeated loading. The use of FRCM as a repair method has gained popularity recently due to its advantages over traditional repair methods, such as fiber reinforced polymer (FRP), especially its compatibility with the concrete substrate. The effect of FRP confinement has been found to improve bond behavior in many studies, but the effect of FRCM confinement has not yet been studied.

1.2 Thesis Organization

This thesis is divided into five chapters. Chapter 1 introduces the topic of the research study. Chapter 2 provides an overview of the subjects seen in the study including bond between the steel reinforcement and the concrete, corrosion, fatigue loading, and the use of FRCM. This chapter presents a review of the available literature on the topics related to this study and the research needs and objectives based on the literature review. Chapter 3 presents the methods used for the research study including the experimental test program, the material properties, the design and construction of the specimens, corrosion technique, and the test setup. In Chapter 4, the experimental results are presented, analyzed, and discussed. Chapter 5 provides conclusions from the current study and recommendations for future studies.

Chapter 2 - Background and Literature Review

2.1 General

This chapter provides an overview of the subjects seen in the study including the bond between the steel reinforcement and the concrete, the corrosion of steel reinforcement, the basics of fatigue loading, and the use of FRCM as a repair method. A review of the available literature on the effects of corrosion, fatigue, and external confinement on bond is included. Following the literature review, an assessment of research needs and objectives for this study are provided.

2.2 Background

2.2.1 Bond

To fully utilize the properties of the reinforcement, the transfer of the load through bond between the reinforcement and the concrete needs to be sufficient. The earliest recorded experimental study on bond was by Thaddeus Hyatt in 1877. In the 1910s, Duff Abrams heavily studied the bond of reinforcement to concrete and contributed greatly to the early development of the understanding of bond mechanics (Abrams, 1913). Over the last century, numerous research studies have analyzed the interaction between concrete and the reinforcement under static and dynamic loads (ACI 408, 2012; FIB, 2000).

Research has made major strides in determining the mechanics and influencing factors of bond behavior, but there are still several gaps in the understanding. Most of the knowledge of bond is primarily empirical due to the specific testing conditions and the large scatter in results (FIB, 2010). It is well accepted that the bond of reinforcement to

concrete results from chemical adhesion, friction forces, and mechanical anchorage/bearing of ribs (ACI 408, 2012) (Figure 2.1).

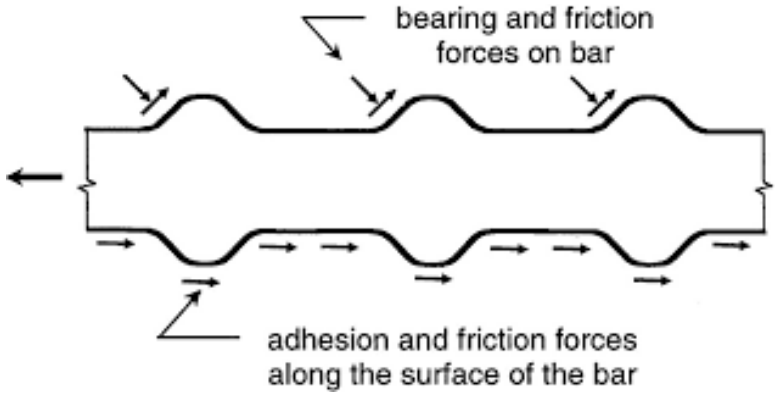

Figure 2.1: Components of Bond (ACI 408, 2012)

The mechanics behind bond behavior has been well established in the literature. For low bond stresses up to 200 psi, the main resisting mechanism is chemical adhesion (Malvar, 1991). Once slip is initiated, the adhesion force is negligible and bearing and friction forces are mobilized. As slip increases, the friction force along the surface of the bar decreases and the bearing of the ribs against the concrete becomes the main mechanism of force transfer. Compressive and shear stresses in the concrete resist the forces from the reinforcement. The stresses in the concrete resolve into circumferential tensile stresses, which cause radial pressure.

There are two main bond failures: splitting failure and pullout failure. When the concrete cover is small (≤ 3 bar diameters) or the spacing between bars is insufficient, the radial pressure will cause the longitudinal cracking in the concrete and result in a splitting failure. When the cover and spacing are adequate, or when the bonded length is small, the longitudinal cracks cannot fully develop. Instead, the concrete keys cast between each

pair of lugs shear off resulting in a pullout failure or the reinforcing bar will yield. Bond stresses are the highest at the end of the beams; therefore, this is generally where bond failures occur.

The efficiency of bond is represented through stress-slip curves. Since bond stress cannot be measured directly, the strain in the reinforcement is measured and correlated to stress through Hooke's Law, which states that the stress (σ) is linearly proportional to the strain (ε) by the modulus of elasticity (E). Bar slip is the measurement of the movement of the bar compared to the surrounding concrete and can be measured at the end of the bar or near the application of load (ACI 408.2, 2012). Generally, the beginning of the stress-slip curve is steep due to adhesion forces. Once adhesion is lost and crack growth increases, the curve will decrease until bond failure at ultimate slip. Ultimate bond stress, slip at the ultimate bond stress, and ultimate slip can be determined from the stress-slip curve and used to model the bond behavior. The initial bond stiffness, the slope of the stress-slip curve upon loading, influences the magnitude of the slip at the ultimate bond stress (ACI 408.2, 2012).

ACI 408 (2012) specifies four different types of test specimens for the analysis of the bond of reinforcement in concrete: pullout, beam-end, beam anchorage, and splice specimens. The two main bond tests found in the literature are beam test and pullout test. For beam tests, when the reinforcement is experiencing tension so is the surrounding concrete. For pullout tests, the surrounding concrete is in compression when the reinforcement is in tension. For this reason, the pullout specimen is the least realistic to actual conditions. Despite this fact, the pullout test is still the most frequently used for

research because it is simple to perform. Splitting failures are more common in most structural applications. Therefore, research studies with conditions that result in splitting failures provide more valuable information for practical applications.

Research has established that bond behavior is influenced by several factors including structural characteristics of the reinforced concrete member, the properties of the reinforcement, and the properties of the concrete (ACI 408, 2012).

Influence of Structural Characteristics

The structural characteristics that influence bond include concrete cover, bar spacing, development and splice length, transverse reinforcement, and bar casting position.

- Large cover and bar spacing tends to result in a pullout failure with higher bond strength. The opposite results in a splitting tensile failure with lower bond strength.
- As development or splice length increases, the bond capacity increases as well.
- The confinement that transverse reinforcement provides limits the progression of splitting cracks, which increases the bond force required to cause failure.
- Bars cast towards the top of the member have lower bond strengths than bars cast towards the bottom of the member due to the higher chance of bleeding and settlement in this region. Bleeding causes water to collect in the void and lower the bond strength. Since there is less room for settlement towards the bottom of the concrete member, the lower bars are less affected by changes in slump, which can influence the bond strength.

Influence of Reinforcement Properties

The properties of the reinforcement that influence bond include size, geometry, and surface condition of the reinforcing bar.

- Larger bars provide higher bond strength with similar confinement. However, larger bars also require longer bonded lengths to yield the bar. In general, it is more favorable to use more smaller diameter bars than a few larger diameter bars to achieve the same desired area of steel. Smaller diameter bars are generally less expensive, easier to transport, and require less development length than larger diameter bars.
- The main measurement for bar geometry in terms of bond performance is relative rib area, which is the ratio of the bearing area to the shearing area. As the relative rib area increases, the bond performance increases.
- The surface condition of the bar affects bond due to its influence on the transfer of force through friction between the concrete and the reinforcement. The bond strength is negatively affected if the bar is not clean. Epoxy coatings are used for corrosion resistance, but reduce bond strength.

Influence of Concrete Properties

The properties of the concrete that influence bond include compressive strength, aggregate type and quantity, tensile strength, fracture energy, lightweight concrete, concrete slump, workability admixtures, fiber reinforcement, and consolidation.

- The bond force is dependent on the tensile strength of the concrete, which can be correlated to the compressive strength of the concrete. Bond strength increases as

the compressive strength of the concrete increases. Research has traditionally represented bond strength using the square root of the compressive strength of the concrete. More recent research shows that the third root and the fourth root of the compressive strength may give a better representation of the bond strength. This approximation takes into account fracture energy.

- For beams with no transverse reinforcement, aggregate size and strength has little influence. However, for beams with transverse reinforcement, the strength and quantity of the aggregate tend to increase the contribution of the transverse reinforcement to bond strength.
- Fracture energy is defined as the capacity of the concrete to dissipate energy as a crack opens. Higher fracture energies result in increased bond strength.
- The bond strength in lightweight concrete is less than that of normal weight concrete because the strength of the aggregate is lower resulting in lower tensile strength, fracture energy, and local bearing capacity.
- Higher slump and the use of workability admixtures lower the bond strength due to the increase of settlement and bleeding.
- The use of fibers allows the concrete to resist load after cracking, which decreases the probability of splitting cracks and the required development length.
- Settlement causes voids below rigidly held bars and bleeding causes water to collect in the void, which negatively affects bond strength. Consolidation reduces the effects of settlement and bleeding.

2.2.2 Corrosion

Corrosion has become a topic of research interest due to the large number of aging reinforced concrete structures experiencing corrosion damage and the high repair cost associated with the damage. According to the analysts at G2MT Laboratories, a metallurgical failure analysis and consulting company, the direct cost of corrosion incurred by owners or operators is currently over $500 billion annually, up from $276 billion in 1998 (Jackson, 2015). The individuals that are not owners or operators also incur cost from corrosion as well; this is referred to as indirect costs. These costs are caused by outages, delays, failures, and litigation due to corrosion damage. The indirect cost is roughly equal to the direct cost, which makes the total annual cost over $1 trillion. At 6.2% of the United States annual GDP, the total cost associated with corrosion is one of the largest single expenses of the U.S. economy.

The corrosion of reinforcement in concrete is electrochemical, which involves the transferring of charge from one component to another (ACI 222, 2001). For the process to take place, an anode and a cathode must be present. The anode produces electrons from the oxidation of iron to form ferrous ions. The cathode consumes electrons from the reduction of oxygen to form hydroxyl ions. These reactions can occur on separate bars, macrocell corrosion, or on the same bar, microcell corrosion (Figure 2.2). In the presence of moisture and oxygen, the hydroxyl ions from the cathodic reaction react with the ferrous ions from the anodic reaction to form a rust product, Fe_2O_3, ferric oxide.

The reactions are as follows (Hunckeler, 1994):

Anodic reaction: $2Fe \rightarrow 2Fe^{2+} + 4e^-$

Cathodic Reaction: $O_2 + 2H_2O + 4e^- \rightarrow 4OH^-$

Sum of the Reactions: $2Fe + 2H_2O + O_2 \rightarrow 2Fe(OH)_2$

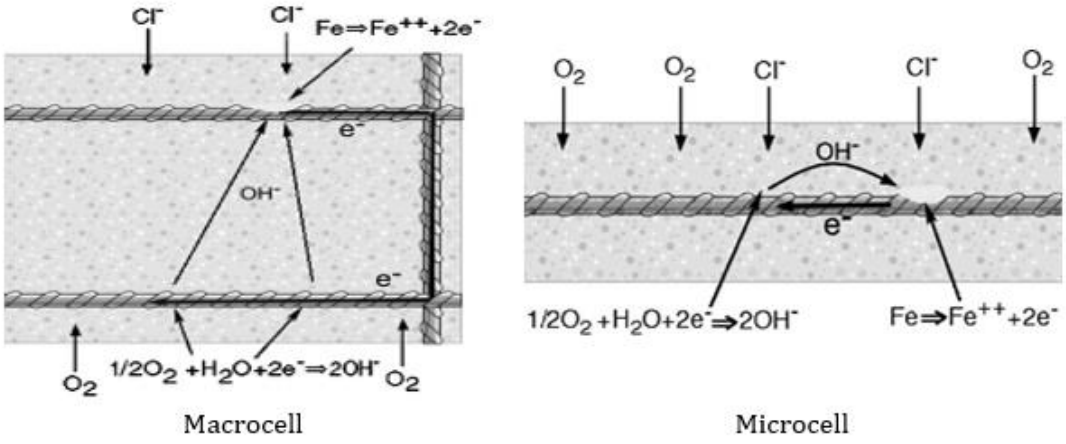

Figure 2.2 - Macrocell versus microcell corrosion (Hansson et al., 2006)

When unhydrated, the ferric oxide occupies two times the volume of the original steel. When the rust product becomes hydrated, it can occupy almost ten times the volume of the original steel (Broomfield, 1997). The expansion caused by the rust product induces large internal stresses on the concrete and can lead to cracking, spalling, and loss of bond between the steel reinforcement and the concrete (Abosrra, 2011). These cracks allow an increased exposure to oxygen, moisture, and chlorides leading to an increase in the corrosion rate. The cracking also affects the bond between the steel reinforcement and the concrete. In addition, the bar diameter is reduced thus negatively affecting the flexural strength, deformational behavior, ductility, and mode of failure in reinforced concrete members (El Maaddawy & Soudki, 2003).

There is not a way to completely prevent corrosion from occurring; however, there are many factors that can accelerate the rate at which the corrosion occurs. The factors include: availability of oxygen, the electrical resistivity, the relative humidity, pH of the concrete, compressive strength of the concrete and temperature (ACI 222, 2001). In order for significant corrosion to occur, moisture and oxygen must be present.

Concrete is basic in nature with a pH between 13.0 and 13.5. This allows for a passive layer of iron oxide to form that protects the reinforcement by limiting the oxidation of iron. Cover-to-bar diameter ratio has a large effect on corrosion (Al-Sulaimani et al., 1990). The additional concrete provides an increased protection to the reinforcement. The larger the cover-to-bar diameter ratio, the higher the corrosion level needed to be to initiate cracking. Once the concrete is cracked, the exposure of the corroded reinforcement to moisture and oxygen is increased thus increasing the corrosion rate. Two processes that can damage this layer of protection are carbonation of concrete and chloride attack.

Corrosion from Carbonation

Carbonation occurs when alkaline components of the cement paste react with the carbon dioxide from the atmosphere to lower the pH of concrete to values between 6 and 9. Lowering the pH of the concrete damages the passive protective layer around the reinforcing steel and allows environmental conditions to negatively impact the reinforcement. According to ACI 222 (2001), the neutralization is most aggressive when the concrete is exposed to intermittent wetting and drying cycles in addition to high temperatures.

Corrosion from Chloride Attack

The concrete cover surrounding the steel bar in reinforced concrete members provides protection from external contaminants, such as, chlorides, sulfates, and alkalis. Cracks in the concrete cover allow increased exposure to harmful conditions such as chloride ions. The chloride is introduced through exposure to chloride-containing water from sources such as dissolved deicing salts, admixtures, chloride contaminated aggregates, and sea water from marine environments. Intermittent wetting and drying cycles increase the rate of chloride penetration. Chloride has a negative effect in reinforced concrete in four main ways (Hunkeler, 2005): (1) it destroys the passive protective film of the steel rebar and makes corrosion attack possible; (2) it reduces the pH of the pore water since it reduces the solubility of Ca(OH)2; (3) it increases the moisture content because of the hygroscopic properties of salts present in concrete; (4) it increases the electrical conductivity of the concrete. Numerous variables affect the corrosion due to chloride attack making an acceptable chloride threshold hard to determine. In general, the accepted chloride content by mass of cement for corrosion risk is around 0.4% (ACI 222, 2001).

Accelerated Corrosion Process

Corrosion occurs naturally at a rate between 10 and 25 $\mu A/cm^2$ (FIB, 2000). To obtain results similar to those found in the field, research would take decades. The percentage of mass loss in the metal is the accepted measure to quantify corrosion. In order to achieve the desired mass loss in a timely and controlled manner, an accelerated corrosion process has been implemented in research. The accelerated corrosion process utilizes chloride

ions and electrical polarization of the steel reinforcement to accelerate the reaction. The chloride ions are introduced to the concrete either through addition of salt in the concrete mix or through submergence of the member in salt water. An external power source is used to supply a positive electrical potential to the steel reinforcement (the anode), which promotes the dissolution of Fe^{+2} ions. An additional stainless steel bar is embedded into the concrete to act as a cathode. The maximum recommended current density to be used is 200 $\mu A/cm^2$ because levels higher than this result in a significant strain in the concrete members (El Maadawy & Soudki, 2003).

2.2.3 Fatigue

Fatigue loading is a repeated cyclic loading resulting in a slow progression to failure. Concrete members fail in fatigue at a lower maximum load than the static capacity of the member. There are two main types of fatigue: low cycle fatigue (high loads with low number of cycles) and high cycle fatigue (low loads with high number of cycles). Low cycle fatigue represents ultimate conditions such as earthquake or storm events with less than 100 cycles and bond stress ranges greater than 600 psi. High cycle fatigue represents service conditions such as traffic loading, vibrating machinery, or wind loads with cycles in the thousands or millions and bond stress ranges typically less than 300 psi (ACI 408.2 2012).

One property that is used for design is the endurance or fatigue limit. If the stress level is kept below this limit, the material will exhibit an “infinite” life. It has been found that concrete does not have a fatigue endurance limit; however, the deformed bar reinforcement does have a limit. Therefore, the forces in the reinforcement are the

determining factor of the flexural fatigue strength. For reinforced concrete members, material properties and loading conditions also influence fatigue life.

Static strength of concrete is highly dependent on its material properties. Since fatigue strength is represented as a proportion of the static strength of the concrete, its material properties are highly important for fatigue strength. A few variables that affect static and fatigue strength include cement content, water cement ratio, curing conditions, age at loading, amount of entrained air, and type of aggregates.

Research has shown that the steel reinforcement is the main determining factor in flexural fatigue strength; therefore, the material properties of the reinforcement are important when analyzing fatigue strength. Deformations in the reinforcement create a better bond between the concrete and steel. Despite this, the deformations also produce stress concentrations at their base, which have been found to be the root of the fatigue fractures. Some testing has shown that yield and tensile strength of the reinforcement has a slight influence on the fatigue strength in the serviceability limit state; however, most research conducted has shown that those factors do not make a measurable difference (ACI 215, 1997).

In experimental tests, the load is alternated between a maximum and a minimum at a set rate. The maximum load is generally a portion of the static load and the minimum a small load to ensure the member does not bounce or slip during testing. In most of research found in the literature, the stress range used for testing was kept at less than 40 percent of the compressive strength to encourage a fatigue failure over a static failure (ACI 215, 1997). It has been found that the rate of loading does not affect the fatigue

strength with frequencies between 70 and 900 cycles per minute and maximum stresses less than 75 percent of the static strength. For stresses above this level, the rate of loading more strongly influences the fatigue strength through creep effects (ACI 215, 1997).

Using Hooke's law, the stress and strain in a material can be linearly related to each other in the elastic range. Stress-strain curves can be used to analyze the behavior of a material under monotonic or repeated loading. The shape of the response for a material under cyclic inelastic loading is considered a hysteresis loop. From the shape of the loop, the total stress range and total strain range can be determined. The height of the loop is the total stress range and the width of the loop is the total strain range. The total energy per unit volume can be determined by calculating the area enclosed within the loop. Plastic deformation can be analyzed using the hysteresis loop. It has already been determined that stress-life data can be linearly plotted on a log-log scale. The same is true for plastic strain-life data. The equation used to relate the plastic strain to the number of cycles is very similar to the equation used to relate the stress to the number of cycles.

2.2.4 FRCM

Composite materials involve reinforcement for additional strength and a matrix to hold the reinforcement to the repaired member. There are many composite materials available, but this review will be focused on the use and research of FRP and FRCM. Arboleda (2014) provides a comprehensive overview of composite materials used for strengthening/repairing concrete.

In the 1990's, Fiber Reinforced Polymer (FRP) repair started to replace traditional methods due to its high strength to weight ratio, high fatigue resistance, ease and speed of

installation, minimal change to geometry, and corrosion resistance (ACI 440.2, 2008). FRP involves attaching reinforcing fibers, either continuous or dispersed, to the concrete surface with the use of an epoxy resin. Research has found that FRP has some limitations due to the epoxy resin including: low heat tolerance, long-term durability uncertainty, inability to apply on wet surfaces or at low temperatures, and poor compatibility with the concrete surface (Al-Salloum et al. 2012). FRP composites have a linear stress-strain curve and do not exhibit yielding prior to failure (Figure 2.3). Since there is no yielding, FRP failure tends to be abrupt, which is not ideal for structures.

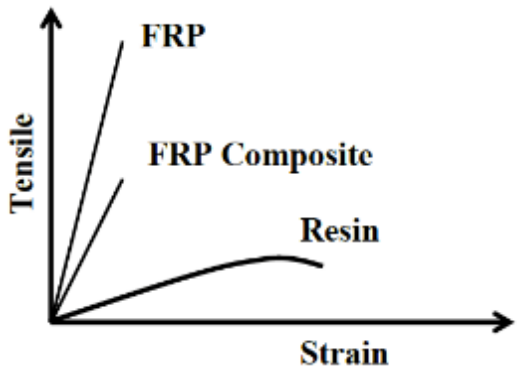

Figure 2.3 - FRP stress-strain behavior (Al-Hammoud, 2012)

Fiber Reinforced Cement Matrix (FRCM) is an emerging externally bonded, composite repair method that involves adhering a fibrous grid textile to the substrate using an inorganic, cementitious matrix. FRCM is similar to fiber reinforced polymer (FRP) composites; however, the cementitious matrix used with FRCM provides several benefits that FRP does not (Sneed et al., 2013; ACI 549, 2013):

(1) High resistance to fire and high temperatures

(2) Resistance to UV radiation

(3) Ease of handling during the application because inorganic binder is water-based

(4) Ease of cleanup and reuse of tools

(5) Low odor and toxin emissions during application and curing

(6) Compatibility with the concrete substrate for chemical, physical, and mechanical properties (especially permeability compatibility)

Every FRCM system is made of two main components: a dry fiber mesh fabric and a cementitious matrix. The reinforcing fibers, made of carbon, alkali-resistant (AR) glass, or poliparafenilenbenzobisoxazole (PBO), are bundled into rovings that are either arranged in two-dimensional or three-dimensional woven textiles. The rovings that run along the main fabric direction are referred to as the warp, and the rovings that run orthogonal to the warp are referred to as the weft (Arboleda 2014). Unlike FRP, the fibers used in FRCM are not fully penetrated or impregnated with a polymeric resin; therefore, they are referred to as "dry fibers" (ACI 549.4, 2013). The cementitious matrix is generally a cement grout or mortar that contains a low dosage of dry polymers (Arboleda 2014).

FRCM is a subset of textile reinforced concrete (TRC) and has also been referred to in the literature as textile reinforced mortar (TRM), mineral-based composites (MBC), and fiber-reinforced cement (FRC) (ACI 549.4, 2013). D'Ambrisi and Focacci (2011) have concluded that the main failure mode for FRCM is debonding of the fibers and the matrix. The matrix will crack before the fabric yields. FRCM composites follow a bi-linear stress-strain curve (Figure 2.4). The two segments correspond to the linear elastic behavior before and after the matrix has cracked. Upon notice of cracking, the appropriate actions can be performed to prevent failure.

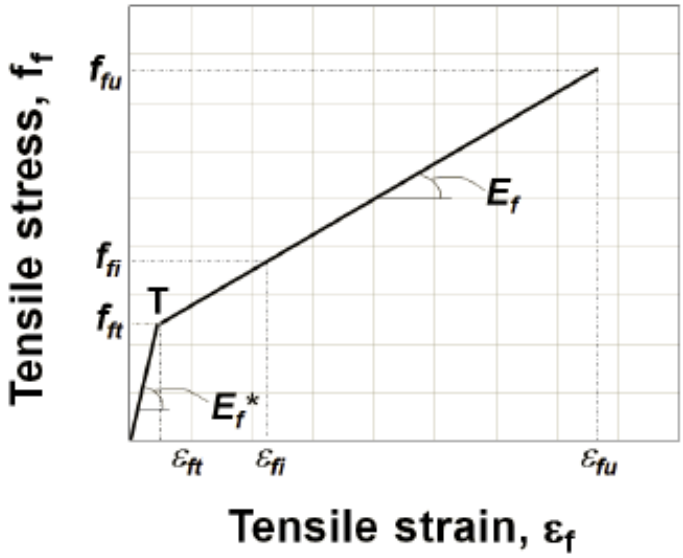

Figure 2.4 - Idealized FRCM stress-strain curve (ACI 549.4R-13)

2.3 Effect of Corrosion on Bond

Structural deterioration most often involves corrosion. Corrosion causes a combination of damage: loss of cross sectional area of the reinforcement, reduction of bond strength, and loss of concrete section from longitudinal cracking and spalling. Most often, the reduction in the bond capacity becomes of concern before the loss of cross sectional area causes a critical loss in flexural capacity resulting in a catastrophic failure. Auyeung, Balaguru, & Chung (2000) have found that specimens can fail in bond with mass loss as low as 2%. The increase in the reinforcement volume can result in cracking, spalling, and delamination of the concrete (Figure 2.5), all which decrease bond strength.

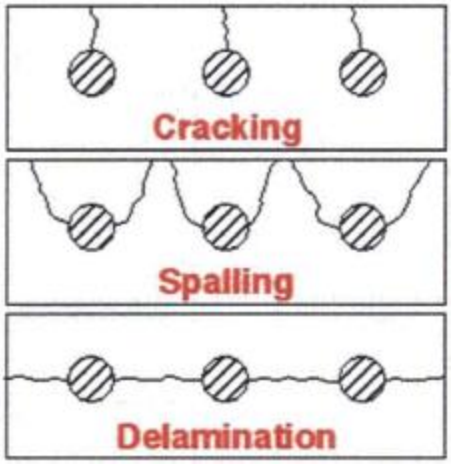

Figure 2.5 - Visible forms of corrosion (Naus 2007)

The effect of corrosion on bond has been researched heavily. Most of the research was conducted using pullout specimens (Al-Sulaimani et al., 1990; Almusallam et al., 1996; Cabrera, 1996; Fu & Chung, 1997; Amleh & Mirza, 1999; Auyeung et al., 2000; Lee, Noguchi & Tomosawa, 2002; Fang et al., 2004; Ouglova et al., 2008; Yalciner, Eren & Sensoy, 2012; Choi et al., 2014; Coccia et al., 2014; Tondolo et al., 2015). In pullout tests, the lateral confinement provided from the testing supports tends to falsely increase the measured bond strength. Studies have been performed on flexural specimens as well (Al-Sulaimani et al., 1990; Mangat & Elgarf, 1999; Stanish, Hooton & Pantazopoulou, 1999; Castel et al., 2000; Chung et al., 2004; Cairns et al., 2005; Lin et al., 2014; Lundgren et al., 2014; Rteil et al.,2010; Al-Hammoud et al.,2010). For both types of test specimens and a variety of conditioning techniques, it has been reported that bond strength reduces and bar slip increases due to corrosion.

Pre-existing corrosion has little to no effect on bond; therefore, research has been focused on corrosion after the concrete has been cast (ACI 222, 2012). The studies have found that there is a slight increase in bond strength in the early stages of corrosion, up to

about 1% mass loss (Figure 2.6). After the initiation of corrosion, the slight increase in bar diameter from the rust product increases radial stresses around the bar, which provide additional friction and bond improvement. As corrosion progresses, high radial tensile stresses develop in the concrete which produce longitudinal cracking, a reduction in frictional resistance, and ultimately a reduction of bond strength.

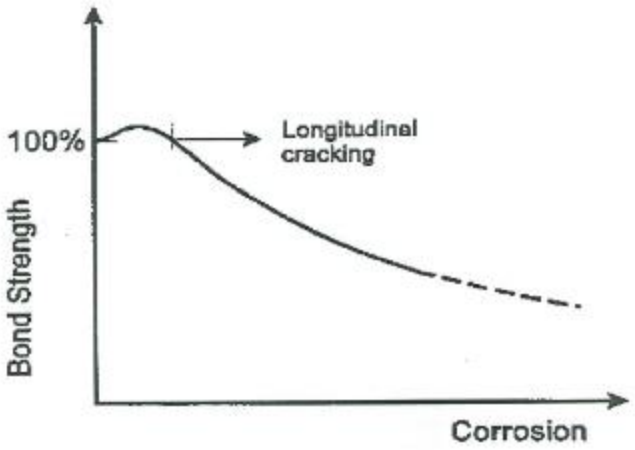

Figure 2.6 - Variation of bond strength with corrosion (FIB 2000)

The research reports a moderate loss of bond strength up to 5% mass loss, a significant loss of bond strength for corrosion between 10 to 15% mass loss, and an almost complete loss at 20% mass loss (Bilcik & Holly, 2013). The loss in bond due to corrosion mass loss is influenced by confinement. The reduction has been found to be less severe in members with stirrups, as opposed to members without stirrups, because the crack development is controlled by internal confinement through stirrups (Lin et al., 2014; Al-Hammoud et al., 2013). The effect of external confinement on bond behavior will be discussed in a later section.

Since corrosion causes both reduction of steel cross-section and loss of bond strength, prediction of corrosion degradation is often difficult to quantify. Many researchers

investigated the different analytical and empirical models for studying the bond strength degradation caused by corrosion in reinforced concrete (Bhargava et al., 2007; Hanjari et al., 2011; Bilcik & Holly, 2013; Guneyisi et al., 2015). The large variance of material properties and environmental conditions that influence the corrosion degradation make it difficult to create a model applicable to every situation. There are similarities between proposed models; however, currently there is not a universally accepted model.

2.4 Effect of Fatigue on Bond

Verna & Stelson (1962) found that failure under fatigue loading is most likely to be caused by damage to the bond between the reinforcement and the surrounding concrete. Failure under repeated loading is caused by the progressive deterioration of bond through propagation of micro-cracks and progressive crushing of concrete in front of the lugs (FIB, 2000; ACI 215, 1974). Fatigue bond failure occurs at lower loads than the static bond capacity of the member.

2.4.1 Uncorroded Specimens

Due to its importance to structural integrity, several researchers have studied the effect of fatigue loading on bond behavior. A large amount of the research performed on fatigue bond behavior used pullout specimens, which are not ideal in assessing bond due to additional compressive force acting on the member. Research has also been conducted on bond-beam specimens. The following conclusions have been made from the conducted studies:

- Beams that fail in bond under static loading will also fail in bond under fatigue loading (Verna & Stelson, 1962).

- Bond behavior under fatigue was related to the material properties of the concrete, especially concrete strength (Verna & Stelson, 1962).
- After initial cracking of the concrete cover, internal cracks develop at the interface between the steel and concrete, which prevent their composite behavior (Goto, 1971).
- If a beam does not fail in fatigue under repeated loading, the static loading and deformation will be unaffected (Rehm & Eligehausen, 1979).
- Bond behavior can be improved with larger spacing between lugs, which increases size of the concrete keys (Pochanart & Harmon, 1989).
- The rate at which bond is damaged, also referred to as slip progression, is greater towards the beginning and end of specimen loading. After initial loading phase, the rate of slip tends to increase at a constant rate until the final loading phase where it increases rapidly again (Balazs, 1991).
- Deformation is increased under repeated loading due to the deterioration of the bond slip relationship (Balazs, 1991; Zanuy, Albajar & Fuente, 2010; Higgins et al., 2013).
- As the number of cycles increases, the crack width increases and the bond strength decreases (Oh & Kim, 2007; Zanuy, Albajar & Fuente, 2010).
- Under repeated loading, slip of the bar causes the concrete between the bar lugs ("concrete key") to crush and shear, which results in reduced bond strength and eventually failure (Rehm & Eligehausen, 1979; Rteil, Soudki & Topper 2010; Al-Hammoud, 2013).

- The bond failure modes, pullout failure and splitting failure, have been found to be similar under fatigue loading as they are under static loading (ACI 408.2, 2012).
- For larger bar diameters (>#11/ 36mm bars), pullout failures tend to control. As the bar diameter increases, the bond strength increases as well (Murcia-Delso, Stavridis & Shing, 2013).

2.4.2 Corroded Specimens

Often times, reinforced concrete structures subjected to fatigue loading are also exposed to environmental conditions that promote corrosion. The combination of corrosion and cyclic loading has been found to cause a significant reduction in bond capacity of reinforced concrete beams (Fang et al., 2006; Sekhar & Raghunath, 2013; Guo et al., 2015; Sun et al., 2015).

Al-Hammoud, Soudki & Topper (2010) studied the fatigue bond behavior of corroded reinforced concrete beams with loading conditions representative of service conditions. They concluded that corrosion can reduce the bond strength by as much as 30% under fatigue loading. Yi et al. (2010) determined that the fatigue lives for mildly corroded and heavily corroded beams decreased by 70% and 99%, respectively, compared to the control beam.

2.5 Effect of External Confinement on Bond

Research on the use of Fiber Reinforced Polymer (FRP) systems as external confinement for concrete in compression began in the mid-1980s (Fardis, 1981). It was found that the FRP laterally restrained the concrete specimens and increased the compressive capacity.

Until the early 2000s, FRP research on flexural members focused on flexural and shear strengthening with the effect of external confinement on bond enhancement left unstudied. Starting in the early 2000s, research on the use of FRP confinement for improving bond behavior in reinforced concrete beams was initiated. In the late 2000s and early 2010s, research began on the use of Fiber Reinforced Cementitious Matrix (FRCM) systems on flexural members for flexural and shear strengthening and on compression members for load capacity strengthening. Research has not yet been conducted to determine the effectiveness of FRCM for improving bond behavior of reinforced concrete beams. This review will focus on the confinement effect of externally bonded repair on the bond behavior of the member for both uncorroded and corroded flexural members.

2.5.1 Uncorroded Specimens

Many studies have investigated the confinement effect of externally bonded FRP laminates to repair flexural members under static loading (Hamad, Ali, & Harajli, 2005; Ozden & Akpinar, 2007; Tastani & Pantazopoulou, 2010) and fatigue loading (Harajli, 2006; Harajli, 2007; Rteil, Soudki, & Topper, 2007; Garcia, Hajirasouliha, & Pilakoutas, 2010). Some research has been performed using pullout specimens (Yasojima & Kanakubo, 2004; Torre-Casanova et al., 2013). While the results can be useful, pullout bond specimens are not the best way to assess bond due to an additional compressive force on the member. The most effective way to analyze bond performance is to use a beam specimen designed to fail in bond.

The overall conclusion from all of the testing performed is that confinement from FRP sheets has the ability to increase the bond resistance substantially under both static and fatigue loading in flexural members. Confinement decreases the rate at which the bond degrades and switches the failure mode from bond splitting to pullout (Xiao-dong, Xiao-hui & Xin-jian, 2013). At this time, there are no studies that confirm that external confinement from FRCM repair has a similar effect as FRP sheets in flexural members.

Trapko (2012) studied the effect of CFRP and FRCM confinement on the compressive strength of cylinders. He found that when the CFRP reached its ultimate load-bearing capacity the failures were catastrophic with the fibers bursting. In the case of the FRCM, the mesh never burst and the damage occurred slowly. The FRCM system remains load bearing after the matrix cracks, which makes this system more desirable. After notice of cracking, appropriate measures can be taken to prevent a catastrophic failure.

2.5.2 Corroded Specimens

Even though most repaired members have corrosion damage; few studies have investigated the effect of external confinement on the bond performance of specimens containing corroded reinforcement (Al-Hammoud, 2012; Xiao-dong, Xiao-hui, & Xin-jian, 2013; Rteil et al., 2007). Numerous studies have been performed on FRP confinement on corroded concrete members by Soudki and his research team (Soudki, et al. 2006). Static and fatigue testing were completed on flexural beams, bond-beams, pullout specimens, and shear critical beams. They have concluded that the structural performance of the repaired member is improved based on the combination of the

following mechanisms: “(1) confinement of the concrete section, thereby lessening corrosion cracking and bond splitting cracks, (2) prevention of further chloride ingress into concrete, thereby reducing rate of corrosion, and (3) increased flexural and shear resistance to overcome the loss in the steel cross-section.”

Gadve et al. (2010) studied the potential of FRP sheets to provide passive and active corrosion protection in pre-corroded concrete beams. Externally bonded FRP sheets were used to provide passive protection. Active protection was provided from electrically conductive carbon fiber wraps acting as an anode while the reinforcing bar is acting as the cathode. Both protection methods were successful in lowering the continuing damage from corrosion. Others have also found that repairing the member with FRP systems retards the rate of post-repair corrosion (Lee et al., 2000).

2.6 Research Motivation

2.6.1 Research Needs

Based on the literature review, it is apparent that confinement from FRCM systems for enhancing bond behavior in flexural members has yet to be studied.

Most research studying bond behavior has used pullout specimens. It is well known that this type of bond test does not yield accurate results due to the additional compressive forces applied to the concrete from the test supports. It has been proposed by several researchers that beam specimens yield more accurate results for bond behavior and bond strength values. Several researchers have studied the effect of fatigue and corrosion on bond, separately and together. Additional testing must be performed to

provide data to further develop reliable models relating bond damage to corrosion and fatigue conditions.

The use of externally bonded FRP systems has been confirmed to enhance the bending, shear, and bond capacities of flexural members, as well as concrete confinement in compression members. The effectiveness of FRCM to improve bending, shear, and compressive capacities has been confirmed by several researchers, but more research needs to be done to better understand the effects of FRCM repair on bond behavior. There have been several studies on the effect of FRP confinement on the fatigue bond behavior of corroded reinforced concrete beams. However, FRCM confinement has not been studied in the same manner.

2.6.2 Research Objectives

The main objective of this study is to determine the effect of FRCM confinement on bond behavior of corroded reinforced concrete beams under static and fatigue loading. The data from this study will also further the understanding of the effects of corrosion and fatigue on bond behavior in flexural members.

Chapter 3 - Methods

3.1 Introduction

The experimental program in this study consisted of testing thirty reinforced concrete bond beams. The purpose of the testing was to study the effect that FRCM repair has on the static and fatigue bond behavior of concrete beams with corroded reinforcement. This chapter describes the test program, the material properties, the design of the specimens, the concrete placement, the FRCM repair, the accelerated corrosion, the evaluation of corrosion, and the test setup.

3.2 Test Program

Thirty full-scale beams that are 10 in. by 6 in. by 6 ft. 6 in. were constructed for analysis in this study. Six beams were left uncorroded. The remaining twenty-four beams experienced an accelerated corrosion process to induce a specified theoretical mass loss (either 5% or 15%). The variables used in this study were corrosion level based on mass loss, repair method used, type of loading, and load range. The two repair materials varied in grid size, which will be discussed in Section 3.3.3. Table 3.1 shows the test matrix that was used for the testing. The nomenclature used for the beams is as follows:

- The first letter was used to identify the level of corrosion induced.
  - N = None (0% mass loss)
  - M = Mild (5% mass loss)
  - H = High (15% mass loss)
- The second letter was used to identify the repair condition and material used.
  - U = Unrepaired
  - R1= Repair with material 1
  - R2 = Repair with material 2
- The third letter was used to identify the type of loading.
  - S = Static loading
  - F = Fatigue or repeated loading

Table 3.1: Test Matrix

Beam Notation	Corrosion	Repair	Loading
N-U-S	None (0%)	Unrepaired	Static
N-U-F-1			Fatigue
N-U-F-2			Fatigue
N-U-F-3			Fatigue
N-U-F-4			Fatigue
N-RP1-S		Repair 1	Static
M-U-S	Mild (5%)	Unrepaired	Static
M-U-F-1			Fatigue
M-U-F-2			Fatigue
M-U-F-3			Fatigue
M-U-F-4			Fatigue
M-R1-F-1		Repair 1	Fatigue
M-R1-F-2			Fatigue
M-R1-F-3			Fatigue
M-R1-F-4			Fatigue
H-U-S	High (15%)	Unrepaired	Static
H-U-F-1			Fatigue
H-U-F-2			Fatigue
H-U-F-3			Fatigue
H-R1-S		Repair 1	Static
H-R1-F-1			Fatigue
H-R1-F-2			Fatigue
H-R1-F-3			Fatigue
H-R1-F-4			Fatigue
H-R1-F-5			Fatigue
H-R2-F-1		Repair 2	Fatigue
H-R2-F-2			Fatigue
H-R2-F-3			Fatigue
H-R2-F-4			Fatigue

3.3 Material Properties

3.3.1 Concrete

Ready mix concrete was supplied by Arrowhead Concrete. The concrete strength was specified as 5000 psi. The 28-day compressive strength, slump, and air for each set are shown in Table 3.2: Concrete properties for the different sets. The concrete mixture proportions (per cubic yard) for all of the beams were: 486.5 lb of portland cement, 151 lb of slag, 1073.6 lb of fine aggregate, 1996.2 lb of coarse aggregate, 31.8 fl. oz. of water reducer, 24.4 fl. oz. retarder, and 32.2 gallons of water. The water to cementitious materials ratio of the concrete used was 0.52.

Table 3.2: Concrete properties for the different sets

		Salted Concrete	Unsalted Concrete
Set One	Compressive Strength (psi)	4188 ± 221	6459 ± 122
	Slump (in)	8.25	8.92
	Air (%)	1.5	1.1
Set Two	Compressive Strength (psi)	6018 ± 73	6809 ± 116
	Slump (in)	4	3.75
	Air (%)	3.75	2.5
Set Three	Compressive Strength (psi)	5802 ± 164	5559 ± 148
	Slump (in)	7.75	6.5
	Air (%)	2.15	3.9

3.3.2 Steel

The concrete beams were reinforced with #6 deformed bars in the tension zone and 5/16 in. smooth bars in the compression zone. Both the #6 deformed bars and the 5/16 in. smooth bars were made of Grade 60 steel with a yield strength of 60 ksi. For the beams that were to be corroded, a 5/16 in. hollow stainless steel bar was placed in the middle of the beam to act as a cathode in the accelerated corrosion process. The 5/16 in. hollow stainless steel bar were made of Grade 304 steel with an outside diameter of 5/16 inch and a wall thickness of 0.035 in.

3.3.3 FRCM

The FRCM composite used in this study consisted of a polyparaphenylene benzobisoxazole (PBO) fiber mesh textile held to the substrate with a polymer-modified cement-based repair mortar. The PBO textiles used for the repair were SITgrid008VB and SITgrid017VB made by V.Fraas in Germany. The two repair materials varied in grid size (Figure 3.1: (a) Repair material 1 (b) Repair material 2). The SITgrid008VB had a 0.4 in. (10 mm) by 0.6 in. (15 mm), and the SITgrid017VB had a 0.4 in. (10 mm) by 0.33 in. (8.5 mm) grid size. Two grid sizes were used to determine if there was a difference in their behavior. The concept is that more fibers would provide more strengthening to the beam. The mortar used, MasterEmaco N 300 CI from BASF, is a one-component thixotropic polymer-modified cement-based mortar with an integral corrosion inhibitor.

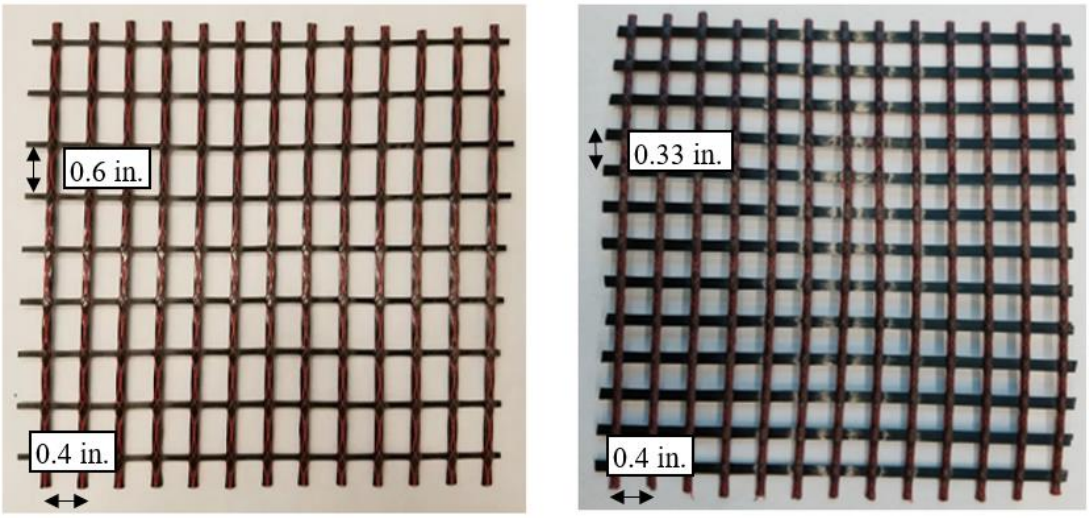

Figure 3.1: (a) Repair material 1 **(b) Repair material 2**

3.4 Design of Specimens

All thirty beams in this study were the same size with a rectangular cross section of ten inches by six inches and a length of six feet six inches. The beam reinforcement and dimensions were based on beam specimens used in a previous study (Al-Hammoud, 2012). Each beam was reinforced with two #6 deformed steel bars in the tension zone with a clear cover of 1.5 inches. Two 5/16 in. smooth bars were placed at 1.75 inches from the top of the beam and 1.5 inches from the sides to provide reinforcement in the compression zone. To prevent shear failure, 5/16 in. stirrups were placed at a spacing of 4.92 inches (125 mm) in the shear zone and 7.87 inches (200 mm) in the flexure zone. The stirrup configuration was kept the same for all of the beams. Figure 3.2 shows the schematic drawing of the beam with stirrup configuration.

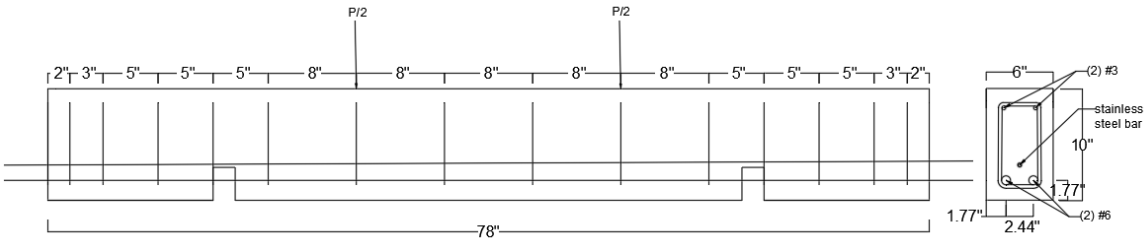

Figure 3.2: Stirrup Configuration

For the beams experiencing corrosion, salt water was added to the mix in the bonded regions to initiate corrosion (see section 3.4). To prevent corrosion of the stirrups in the bonded regions, the stirrups in this region were coated with a chemical resistant epoxy coating and the corners were wrapped with electrical tape (Figure 3.3). A hollow 5/16 inch stainless steel bar, Grade 304, was placed fat 3.15 inches from the bottom of the beams experiencing corrosion to provide a cathode for the accelerated corrosion process. Holes were drilled into the ends of the #6 tension bars and the stainless steel bars to be used as connection points when wiring the beams to the power supply. The accelerated corrosion process is discussed in section 3.7.

Figure 3.3: Epoxy coated stirrups with electrical tape at the corners

To ensure bond failure, the beams were designed as modified anchorage specimens, in which the bonded zone is controlled. Low-density polyethylene (LDP) tubing was applied to the reinforcing bars to create unbonded and bonded portions (Figure 3.4). The debonded zones serve two purposes. The debonded zone in the middle of the bar is used to reduce the bonded length in order to ensure a bond failure. The debonded zone at the ends of the bar eliminates the additional confining effect from the support reaction that can affect the bond behavior (Ahlborn & DenHartigh 2002).

Figure 3.4: Low-density Polyethylene Tubing on the Reinforcing Bars

Extruded polystyrene, a high-density foam (Figure 3.5), was used to create an open pocket to expose the reinforcing bars in the tension zone (Figure 3.6). Prior to testing, the foam was removed to leave an exposed section for easy instrumentation to measure both slip and strain of the reinforcement.

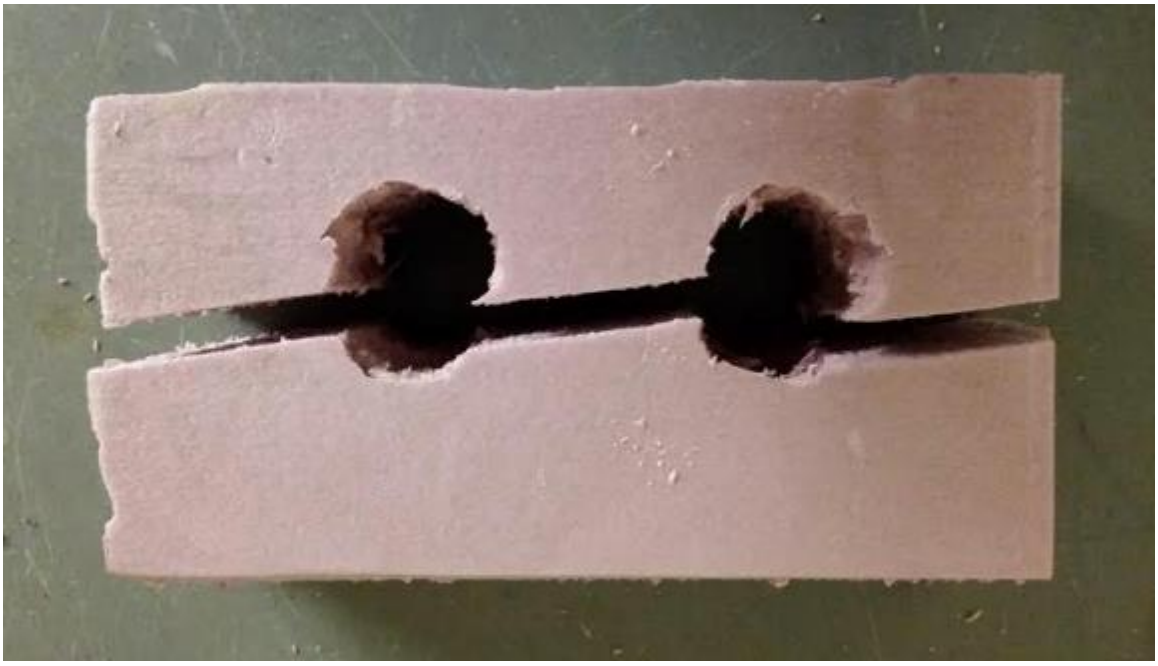

Figure 3.5: High-Density Foam Pieces

Figure 3.6: Beam Cage Layout

3.5 Concrete Placement

Thirty full-scale beams were cast in three sets. Sets one and three contained five beams each and set two contained twenty beams. Four reusable wooden forms, each holding five beams, were built for use in the concrete placement. Holes were drilled into the end pieces of the forms to allow for the extension of the steel reinforcement and stainless steel bars beyond the beam length. Saltwater was added to the concrete in the bonded portions of the beams located in the region near the support up to midlevel of the beam. The amount of salt (NaCl) added to the water was based on 2.15% chloride (Cl^-) of the cement amount by mass; this level has been determined to help initiate the corrosion process. The salted concrete was placed in the bonded regions first. To keep the salted concrete in the desired region, plastic separator pieces were constructed to act as a barrier until the unsalted concrete was added to the unbonded region (Figure 3.7a). Below the bars, the foam pocket acted as the barrier. Once the beam was filled to mid level, the plastic separators were removed and the rest of the beam was filled with unsalted concrete. Figure 3.7b shows the placement of the plastic separator pieces.

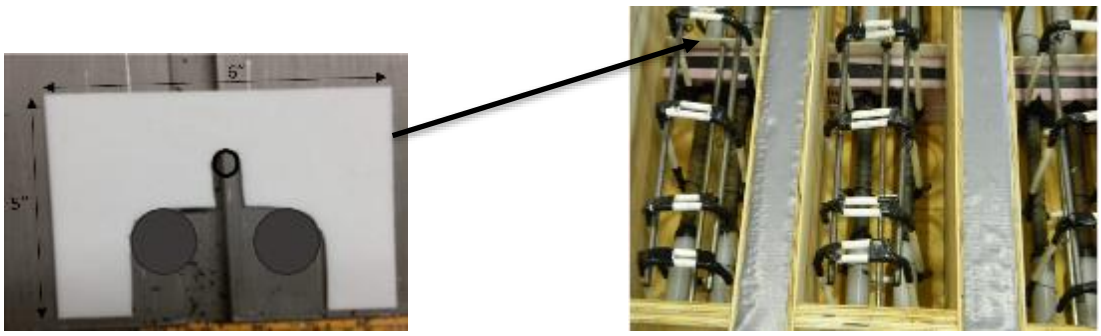

Figure 3.7: (a) Plastic Separator Pieces (b) Placement of Plastic Separators

The water-cement ratio used for the concrete mix was 0.52. The process for the concrete mixing was slightly different for the three sets.

Set One

The concrete for set one was batched and mixed on site using a five cubic foot mixer. There were a total of six batches produced for this set: two salted and four unsalted. The mixer was thoroughly rinsed between salted mixes and unsalted to prevent contamination of the unsalted mix.

Set Two

Due to the large volume of set two (20 beams), a local ready mix plant brought the concrete to the site in two trucks: one salted and one unsalted. The unsalted concrete was brought to the site with a water-cement ratio of 0.52 as specified. The salted concrete was brought to the site with a water-cement ratio of 0.42 and a calculated amount of salt water was added to the truck onsite (Figure 3.8).

Figure 3.8: Addition of Salt Water to the Ready Mix Truck

Set Three

For set three, a local ready mix plant brought the concrete to the site in one truck with a water-cement ratio of 0.42. On site, concrete was taken out of the truck in known volumes and placed in a five cubic foot mixer. Calculated amounts of salt water were added to the concrete in the mixer to reach a water-cement ratio of 0.52. Once the required amount of salted concrete was removed from the truck, a calculated amount of plain water was added to the truck to bring the water-cement ratio up to 0.52.

Hooks were made to assist with moving the beams once they were cured (Figure 3.9). The legs of the hooks were placed under the stirrups towards the ends of the beams after all the concrete was placed. After the hooks were put in place, the concrete was finished (Figure 3.10).

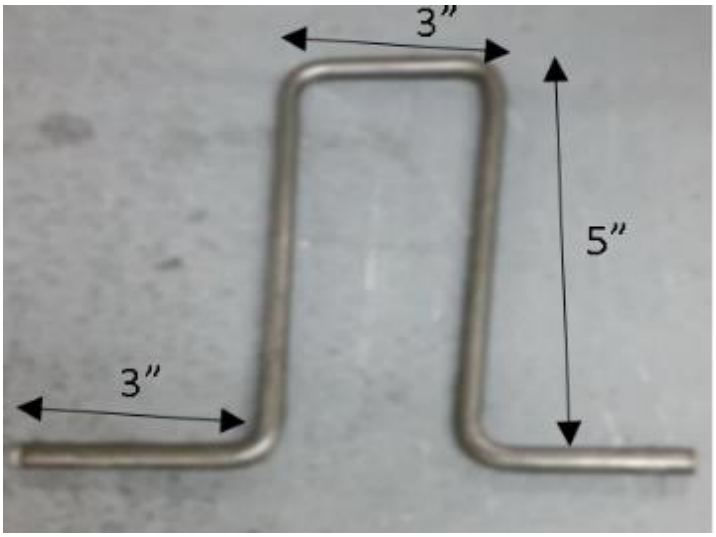

Figure 3.9: Hooks

Figure 3.10: Finished Beams with Hooks

The concrete was left to harden for a few hours, and then wetted burlap and plastic sheets were applied to the surface (Figure 3.11). The burlap was wetted multiple times a day for the first seven days of curing to ensure adequate hydration of the concrete. After seven days, the beams were removed from the forms and left to cure in normal room conditions. After 28 days, the beams to be corroded were moved into a corrosion chamber and were

wired for the accelerated corrosion process (Figure 3.12). The corrosion chamber was designed to hold six beams on each of the four shelves. It consisted of 4x4 corner posts with two intermediate supports along the back. Two intermediate supports were added to the front of the shelving once the beams were placed on the shelves. The shelves themselves were constructed of 2x4 boards, with two at each end in the one direction and one at six inches in the other direction. Simpson joist hangers were used for connecting the boards to the end boards. A heated water tank and fan were added to provide heat and humidity to the inside of the chamber. The outside of the chamber was insulated to keep the heat and moisture inside the chamber.

Figure 3.11: Concrete Curing with Burlap and Plastic

Figure 3.12: Beams Placed in Chamber with Forklift

3.6 FRCM Repair

Fourteen beams were repaired using FRCM. One uncorroded beam was repaired. The rest of the repaired beams were repaired after the corrosion process was complete. A single layer of FRCM was applied to the anchorage zone of the beam in a U-shape to confine the beam in bond (Figure 3.13). Two different fiber grid sheets were used with differing grid sizes: SITgrid008VB (repair 1) and SITgrid017VB (repair 2). The sheets were cut with a width of 8 inches and a length of 26 inches. The cementitious matrix used, MasterEmaco N 300 CI, is a one-component thixotropic polymer-modified cement-based mortar with a corrosion inhibitor.

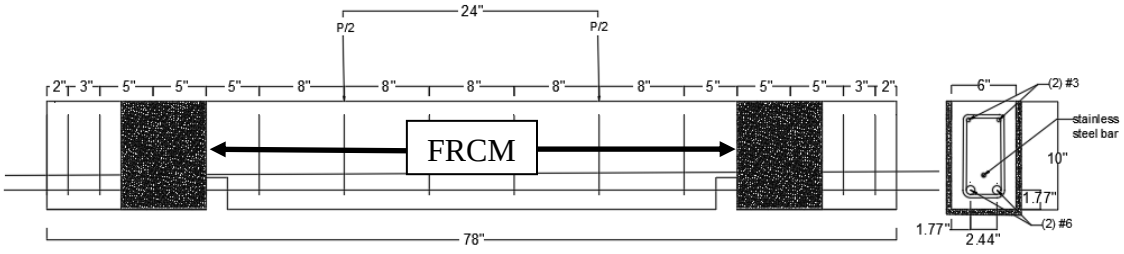

Figure 3.13: Beam FRCM repair schematic

The FRCM was applied following a procedure used in previous FRCM studies found in ACI 549.4R-13 (Figure 3.14):

a) The concrete surfaces in the anchorage zone were prepared by grinding to remove corrosion staining and provide a good bonding surface. The bottom edges of the beams were also ground to achieve a rounded corner with a radius of 1.2 inches (30 mm).
b) The surface was wetted to a saturated surface dry condition to ensure proper bonding of the FRCM repair to the concrete.
c) A quarter-inch thick layer of mortar was used to repair cracks and create a base for the FRCM application.
d) The textile was applied to the surface and pressed into the first mortar layer.
e) An additional quarter-inch thick layer of mortar was applied over the textile.
f) The repair system was wrapped with wet burlap and plastic to assist with curing.

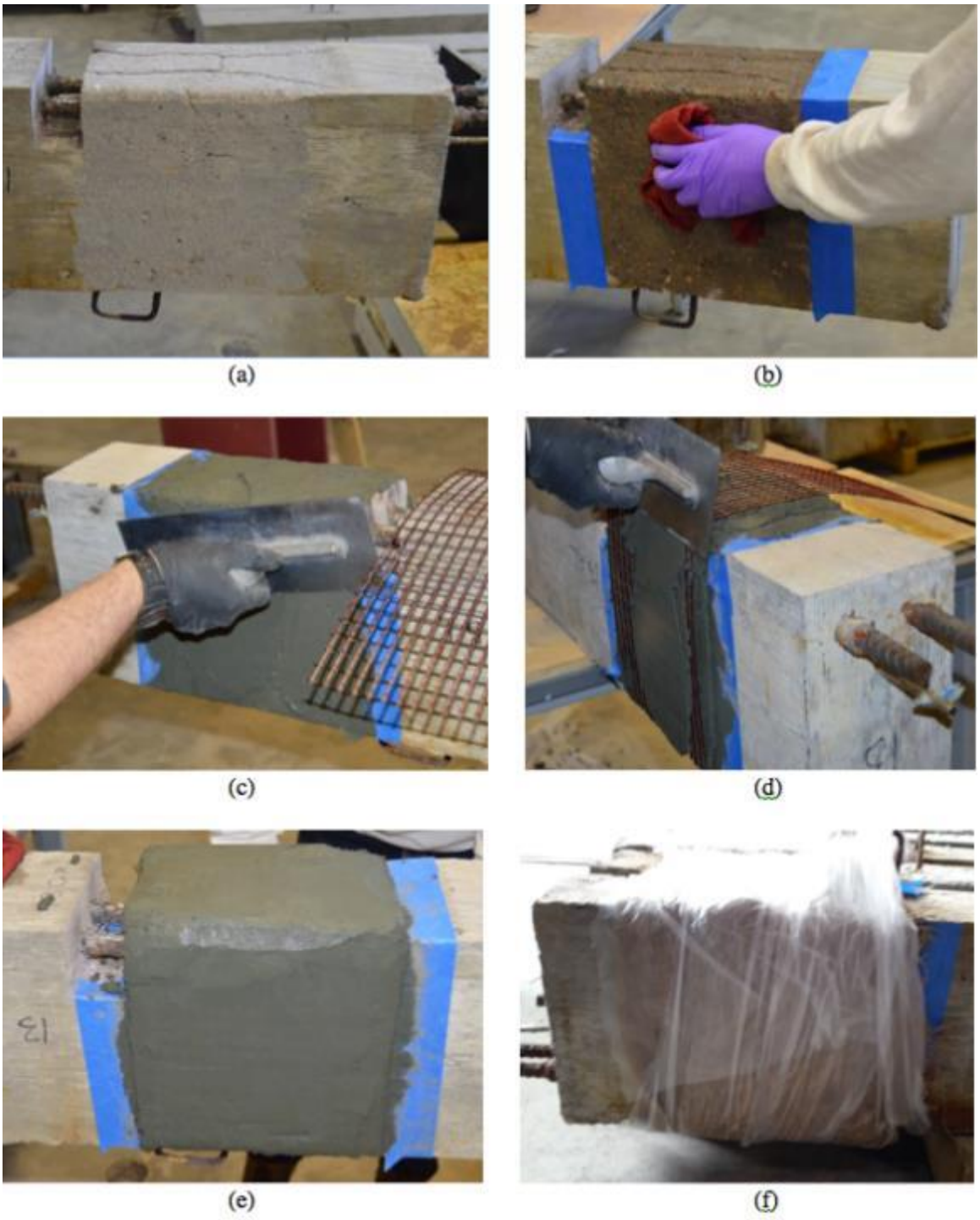

Figure 3.14: FRCM Beam Repair Procedure

3.7 Accelerated Corrosion

An accelerated corrosion technique was utilized to reach the required levels of corrosion in a more timely and controlled manner. This technique involves the use of chloride salts in the concrete to activate the corrosion process. Numerous variables affect corrosion making an acceptable chloride threshold hard to determine; however, 0.4% is an accepted threshold for chloride content by mass of cement (ACI 222, 2001). In this study, the amount of chloride salt (NaCl) was based on 2.15% chloride (Cl^-) of the cement amount by mass. Since this amount is greater than the chloride threshold for corrosion, it is sufficient for the depassivation of the reinforcing steel (ACI Committee 222, 2001). In the presence of moisture and oxygen, electrical polarization of the steel reinforcement is used to accelerate the corrosion reaction. Faraday's Law was used to determine the time required to reach the desired mass loss:

$$m = \frac{Ita}{ZF}$$

where: m = mass loss (g)

I = corrosion current (A)

t = corrosion time (s)

a = atomic weight (56 g for iron)

Z = valence of the corroding metal (2 for iron)

F = Faraday's constant (96,500 A.s.)

In accordance with previous studies, a current density of 967.5 μA/in^2 (150 μA/cm^2) was used for the accelerated corrosion process (El Maadawy & Soudki, 2003). The corrosion current was determined by multiplying the current density by the surface area of the

reinforcing bars within the salted region. The surface area of the stirrups in this region was not included since they were epoxy coated. It was determined that it would take 50 days for the mild corrosion (5% mass loss) and 150 days for the high corrosion (15% mass loss). Previous studies (Al-Hammoud, Soudki & Topper, 2011; Badawi & Soudki, 2005) have found that Faraday's law underestimates the time needed to reach higher levels of mass loss; therefore, an additional 30% was added to the time for the high corrosion level (195 days).

The beams were connected in series to ensure constant current flow. The direction of current flow was set so that the tension steel would act as the anode and stainless steel bar would act as the cathode. A diagram of the wiring and more detailed corrosion calculations can be found in Appendix A and Appendix B, respectively. The current allowed for an accelerated corrosion of the reinforcement in the salted region of the beams. Throughout the corrosion process, the beams were kept in a chamber that supplied the reaction with sufficient moisture and oxygen levels to ensure corrosion.

3.8 Testing

3.9.1 Instrumentation

Linear variable differential transducers (LVDTs), with a range of 1 in (50 mm), were placed on the ends of the reinforcing bars and in the pocket to measure the slip of the reinforcement relative to the concrete. An additional LVDT, with a range of 2 in (100 mm) was used to measure the beam deflection at midspan. The LVDTs were manufactured by TransTek, Inc.

Strain gauges, with a resistance of 350 Ω and a gauge length of 5 mm, were used to measure the strain in the #6 tension reinforcement. The strain gauges were manufactured by Tokyo Sokki Kenkyujo Co., Ltd. in Japan. A small portion of the reinforcement in the pocket was ground to provide a smooth surface for the application of the strain gauges as shown in Figure 3.15. Once the surface was cleaned, conditioned, and neutralized; the strain gauges were applied to the surface using an adhesive (Loctite #496).

Figure 3.15: Strain gauge applied to bar at notch

A servo-controlled hydraulic actuator controlled by a ShoreWestern SC6000 controller was used to apply the load to the beams. A 100 kip (445 kN) load cell was used to measure the applied load throughout the testing. The readings of the strain gauges, LVDTs, and load cell were recorded using the National Instruments data acquisition system at a sampling rate of 10 readings per second and saved in a computer. This study was the first to use this testing equipment; therefore, a great deal of development of the testing system was involved during this study.

3.9.2 Loading Procedure

To produce a constant moment region in the middle third of the beam, four-point bending was used for both the static and fatigue loading. The load was transferred to the beam using a steel spreader beam with two contact points that are two feet apart. Figure 3.16 shows the test setup used.

Figure 3.16: Test setup

The static tests were conducted under displacement at a rate of 0.001 in. per second until the beam failed, when the load reached 60% of the peak load or one of the displacement limits was met. The fatigue tests were conducted under load control. A sine wave load cycle was applied using the Shore Western SC6000 controller at a frequency of 2 Hz. To produce useful S-N curves, the maximum load levels were varied to provide fatigue lives between 10,000 and 500,000 cycles. If a test reached one million cycles, the test was stopped, the load was increased, and the test was restarted. The minimum load was set at 1.67 kips to prevent the beam from slipping or bouncing. A beam was considered to have failed when it reached the displacement limits.

3.9 Evaluation of Corrosion

After loading each beam to failure, the bonded sections of the #6 tension reinforcing bars were removed from the beam. To evaluate the actual mass loss of the steel reinforcement, a chemical cleaning procedure found in ASTM G1-03 was followed. This procedure uses hydrochloric acid baths to remove the corrosion products from the surface of the bars. This gives an accurate weight after corrosion, which can be compared to the initial weight to determine the actual mass loss. The full procedure is described in Appendix C.

Chapter 4 - Experimental Results

4.1 Introduction

In this chapter, the experimental results from the study will be presented, analyzed, and discussed. The thirty beams were corroded to three theoretical corrosion levels (0%, 5%, and 15%). One unrepaired beam from each corrosion level was tested monotonically to determine the static capacity, which was used to determine the load ranges to use in the fatigue testing. Two additional static tests were performed in beams repaired with repair 1: one uncorroded and one high corroded. The maximum load applied during the fatigue testing was varied to achieve a distribution of fatigue lives. The minimum load was fixed at 1.67 kips to prevent the beam from bouncing on the stand. The beams were grouped based on corrosion level and repair condition:

- N-U: no corrosion and unrepaired.
- N-R1: no corrosion and repaired with repair 1.
- M-U: mild corrosion and unrepaired.
- M-R1: mild corrosion and repaired with repair 1.
- H-U: high corrosion and unrepaired.
- H-R1: high corrosion and repaired with repair 1.
- H-R2: high corrosion and repaired with repair 2.

This chapter starts by discussing the corrosion results followed by an overall summary of the individual test results of the beams tested monotonically to failure. Then, the fatigue test results are presented with a summary of each set and detailed results from each test.

4.2 Corrosion Results

The actual mass loss results from the induced corrosion were higher than expected based on the theoretical calculations determined using Faraday's law. The beams theoretically corroded to 5% mass loss had actual mass loss varying between 14.27% and 17.24%. The beams theoretically corroded to 15% mass loss had actual mass loss varying between 15.95% to 25.12%. This irregularity is consistent with previous studies found in the literature (El Maaddawy et al, 2003; Al-Hammound et al., 2012).

In previous studies, Faraday's law was found to over predict corrosion at lower mass losses and under predict corrosion at higher mass loses. In this study, the required time determined to reach the theoretical mass loss was increased by 30% to account for the under prediction. However, this increase was also incorrectly applied to the beams at the lower theoretical mass loss (5%). This is most likely why the beams at this lower theoretical level corroded to a much higher level than expected. Faraday's law was also determined using reinforcing bars exposed to air. In the case of this study, the bars were embedded into concrete; therefore, the bars experience a different level of corrosion than if they were directly exposed to air.

Since the range of mass loss was not significantly different between the mild and high corroded levels, the corroded beams were lumped into one group and analyzed together. Figure 4.1 displays the variation of the actual mass loss compared expected for induced current exposure time in days. Table 4.1 shows the rearranged test matrix with the actual mass loss determined through the corrosion evaluation.

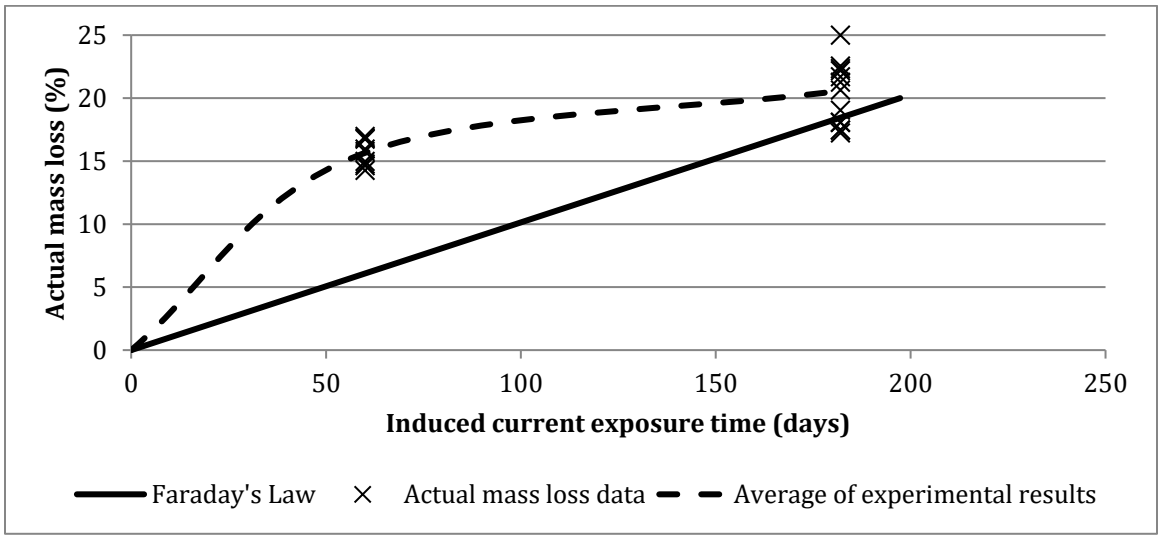

Figure 4.1: Variation of mass loss results versus induced current exposure

Table 4.1: Test matrix with actual mass loss

Beam Notation	Corrosion	Repair	Theoretical Mass Loss (%)	Actual Mass Loss (%)
H-U-S-1	Corroded	Unrepaired	15	21.69%
H-U-S-2				14.98%
H-U-F-1				20.64%
H-U-F-2				22.18%
H-U-F-3				16.83%
H-U-F-4				14.27%
H-U-F-5				14.78%
H-U-F-6				15.76%
H-U-F-7				14.63%
H-R1-S		Repair 1		19.04%
H-R1-F-1				18.09%
H-R1-F-2				17.45%
H-R1-F-3				17.24%
H-R1-F-4				18.06%
H-R1-F-5				21.27%
H-R1-F-6				17.48%
H-R1-F-7				22.35%
H-R1-F-8				16.96%
H-R1-F-9				16.74%
H-R2-F-1		Repair 2		22.55%
H-R2-F-2				25.00%
H-R2-F-3				25.12%
H-R2-F-4				15.95%

4.3 Static Test Results

Five modified anchorage specimens were tested statically to failure. In this portion, the beams differed on both corrosion level and repair conditions. Three beams for varying corrosion levels were tested in the unrepaired condition. Beams from two corrosion levels (None and High) were tested in the repaired condition. The results from this portion of the testing were used to determine the load ranges to use in the fatigue testing portion of the study. This section will provide an overview of the overall behavior and mode of failure, load vs. deflection behavior, slip behavior, and strain behavior. A more detailed discussion for each beam in this group can be found in Appendix D. The beam graphs use the following nomenclature for referring to the measurement location:

- Front side (A) or back side (B)
- Left end (L) or right end (R)
- Notch/loaded end (N) and free end (E)

4.3.1 Overall Behavior and Mode of Failure

Table 4.2 summarizes the results from the static tests performed in this study. As expected, the corroded beams had a lower static capacity than the uncorroded beam. Compared to the uncorroded beam, the one corroded beam had a 62.4% reduction in maximum load, while the other corroded beam had a 21.1% reduction in maximum load. In previous studies, static capacity was found to decrease as corrosion increases. In this study, the lower corroded beam reached a lower peak load than the higher corroded beam. This is likely due to the higher level of corrosion cracking observed on the mild corroded beam compared to the high corroded beam. In the lower corroded beam, a loss

of bond occurred at a lower loading due to more rapid crack propagation. There were also issues with the wiring during the accelerated corrosion process, which may have affected the bond deterioration due to corrosion.

The general mode of failure for each of the beams was a mixture of shear and bond failure near the support. For the unrepaired beams, the concrete cover below the bar spalled off leading to a splitting bond failure. Shear cracks near the supports affected the bond failure as well. As expected, the repaired beams reached a higher maximum load than the unrepaired beam at the same corrosion level. The uncorroded repaired beam had a 26.9% increase in static capacity compared to the uncorroded unrepaired beam. The corroded repaired beam had a 30.2% increase in static capacity compared to the corroded unrepaired beam. This is due to the increased stiffness of the repaired beam, as well, as the increased bond performance due to the additional confinement provided by the repair. Between the two repaired beams, the high corroded beam was found to be stiffer than the uncorroded beam. However, upon crack initiation the high corroded beam could no longer take an increasing load, whereas the uncorroded beam did. This ultimately led the uncorroded beam to a higher peak load. Detailed descriptions and pictures of beam failures in this group can be found in Appendix D.

Table 4.2: Results of static beam tests

Beam Notation	Maximum Load (kip)	Actual Mass Loss (%)	% Change
N-U-S	16.4	0	0
H-U-S-1	10.1	14.98	-38.4%
H-U-S-2	13.54	21.69	-17.4%
N-R1-S	22.44	0	+36.8%
H-R1-S	19.4	19.04	+18.3%

4.3.2 Load vs. Deflection Behavior

Figure 4.2 and Figure 4.3 show the load versus midspan deflection for the static tests, unrepaired and repaired, respectively. The drops in load indicate crack formation in the beam. Each beam exhibited a linear behavior until initial cracking, when the first drop occurred. After initial cracking, the load continued to increase linearly again until the beam reached its peak load. After reaching peak loading, the test continued, with decreasing load and increasing midspan deflection, until the beam reached 60% of the peak load, which was set as the end of the test. As the midspan deflection increased, the crack widths continued to increase until failure.

For the unrepaired beams (Figure 4.2), the corroded beams reached lower peak loads than the uncorroded beam, as expected. All beams experienced a slight drop in loading after initial cracking. However, the drop in load after the reaching the peak load were more extreme in the uncorroded beam than the corroded beams. For both of the corroded tests, when the load reached its peak there was a slow decline in load with increasing midspan deflection until the load reached 60% of the peak load and the test was stopped. For the uncorroded test, the load experienced a significant drop when it reached its peak followed by a slight incline in loading. As the midspan deflection continued to increase, the load eventually began to decline until it reached 60% of the peak load and the test was stopped. For all three tests, the peak load was reached at roughly 0.2 in. of midspan deflection.

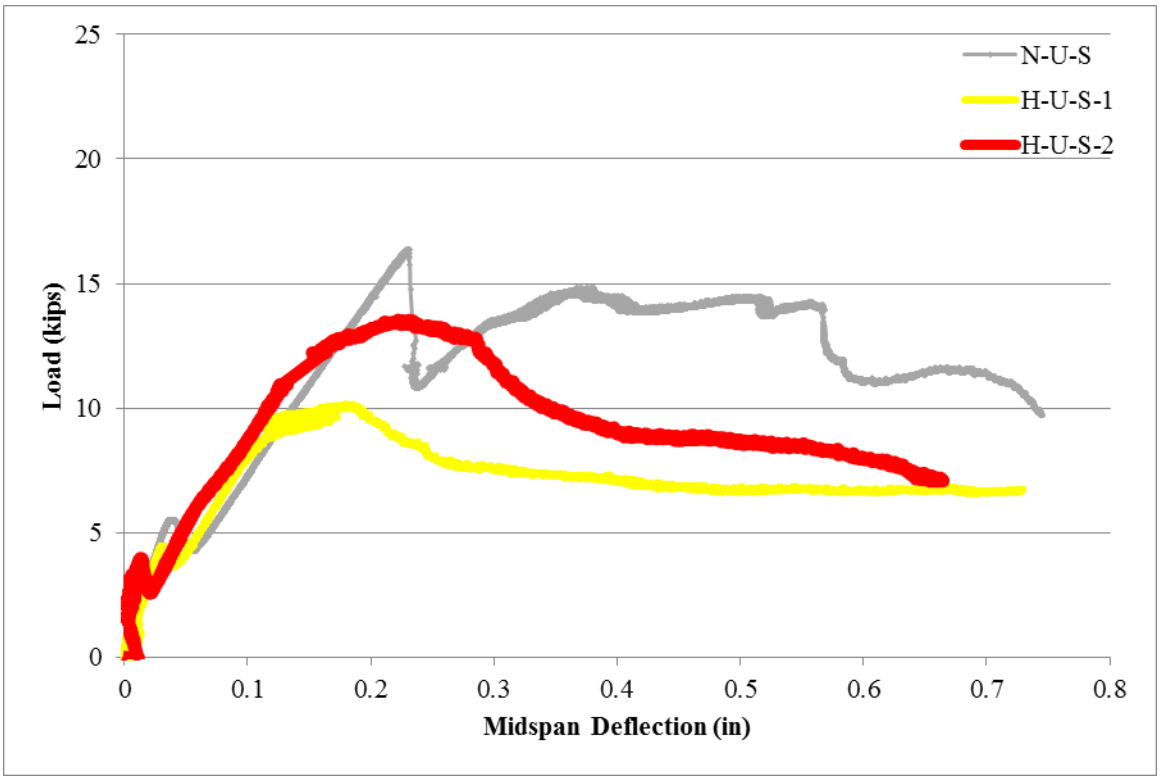

Figure 4.2: Load vs. midspan deflection for unrepaired static beams

As discussed in the previous section, between the two repaired beams, the corroded beam was found to be stiffer than the uncorroded beam at the beginning of the testing. This stiffness is represented by the steepness of the slope for the load vs. deflection curve. The slope is steeper on the corroded beam prior to crack initiation, indicating a higher stiffness. Upon crack initiation, the corroded beam could no longer resist an increasing load, whereas the uncorroded beam continued to resist increasing load after cracking, which led the uncorroded beam to reach a higher peak load than the corroded beam.

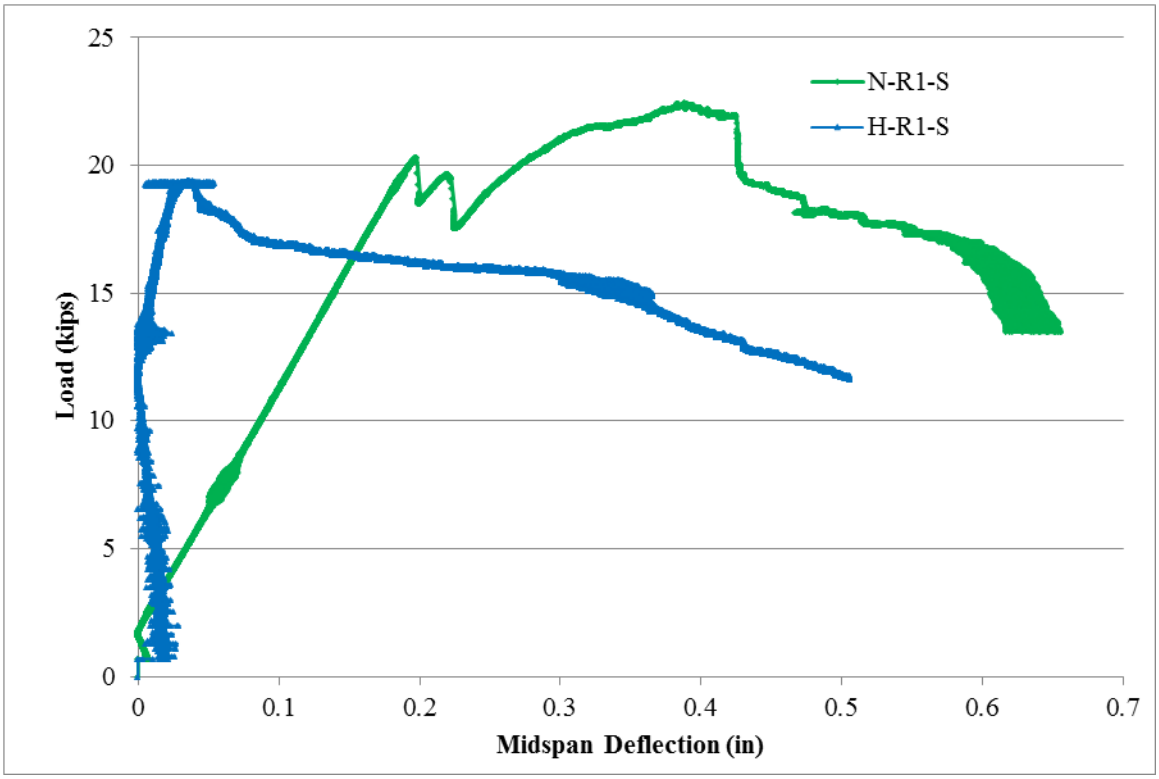

Figure 4.3: Load vs. midspan deflection for repaired static beams

Figure 4.4 shows the load vs. deflection curves for all the static beams together on the same graph. The repaired beams have a steeper slope compared to the graphs for the unrepaired beams indicating a higher stiffness of the repaired beams, as expected. The behavior after the beam reached its peak load is similar between the repaired and unrepaired sets for the both of the corrosion levels. The uncorroded beams, both unrepaired and repaired, tend to have an additional increase in loading following load drops, whereas the corroded beams, both unrepaired and repaired, tend to decrease in loading following reaching the peak load.

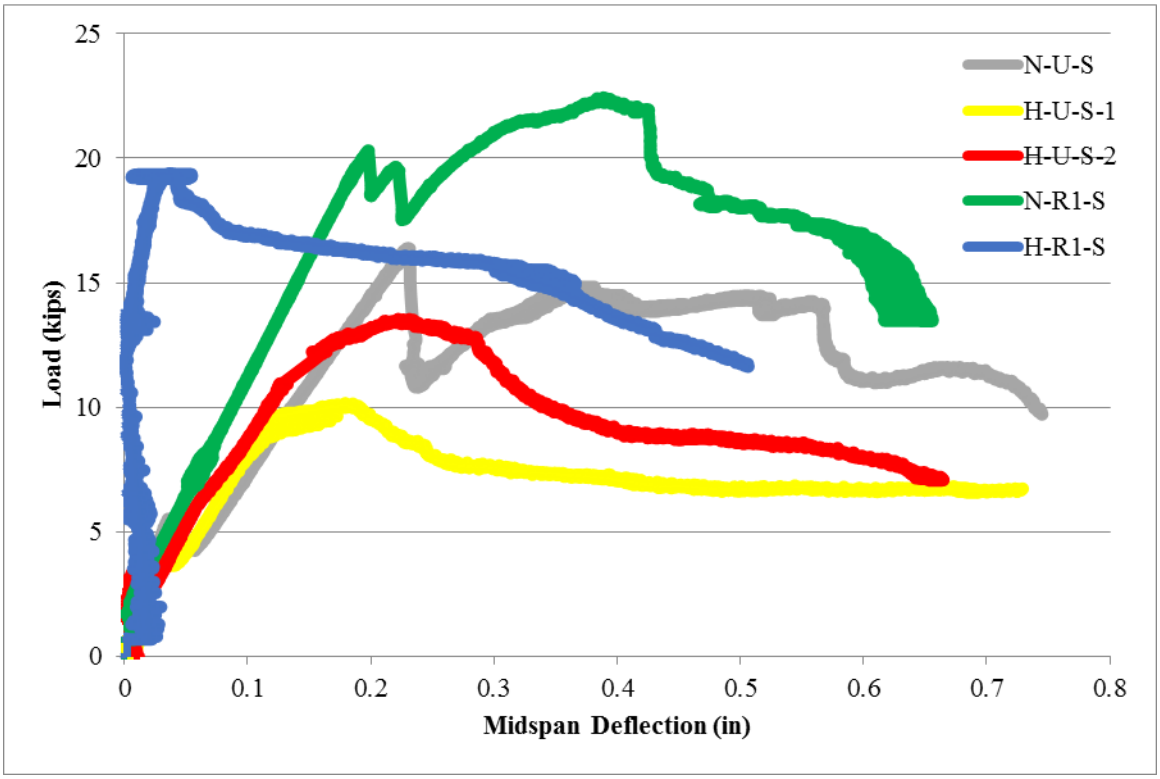

Figure 4.4: Load vs. midspan deflection for all static beams

4.3.1 Load-Slip Behavior

Figure 4.5 shows the load versus slip results for beam N-U-S. The slip measured from the notch increased slowly with increasing load up to the peak load, where it continued to increase in rate slightly. The slip at the free end of the bar was not initiated until the peak load. Under the peak load, shear cracks formed on both sides of the right support causing a loss of bond in this region. The bar slipped at this point and continued to slip at an increasing rate throughout the duration of the test. The slip at the end reached 1 in. at the failure of the beam. The measurement for the slip from the notch was done relative to the wrong end and that explains the discrepancy of the results. Thus, from here afterwards slip results were based on free end only. This was noticed after analysis of results.

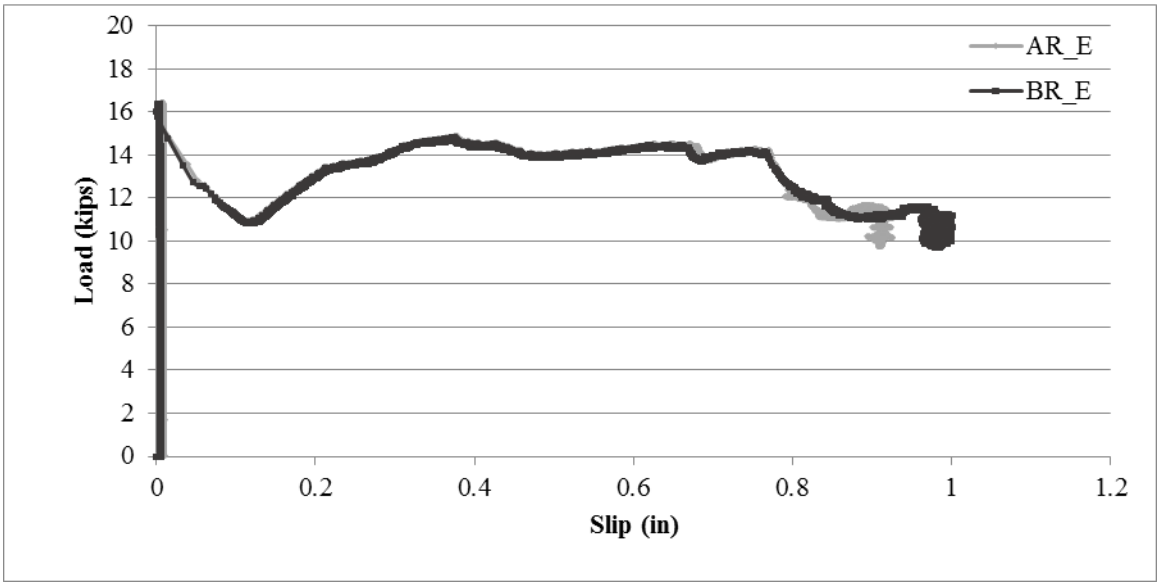

Figure 4.5: Beam N-U-S load versus slip from notch on failed side

Both unrepaired corroded beams, exhibited similar slip behavior to the unrepaired uncorroded beam, but at a lower maximum load. Figure 4.6 and Figure 4.7show the load versus slip results for beam H-U-S-1 and beam H-U-S-2, respectively.

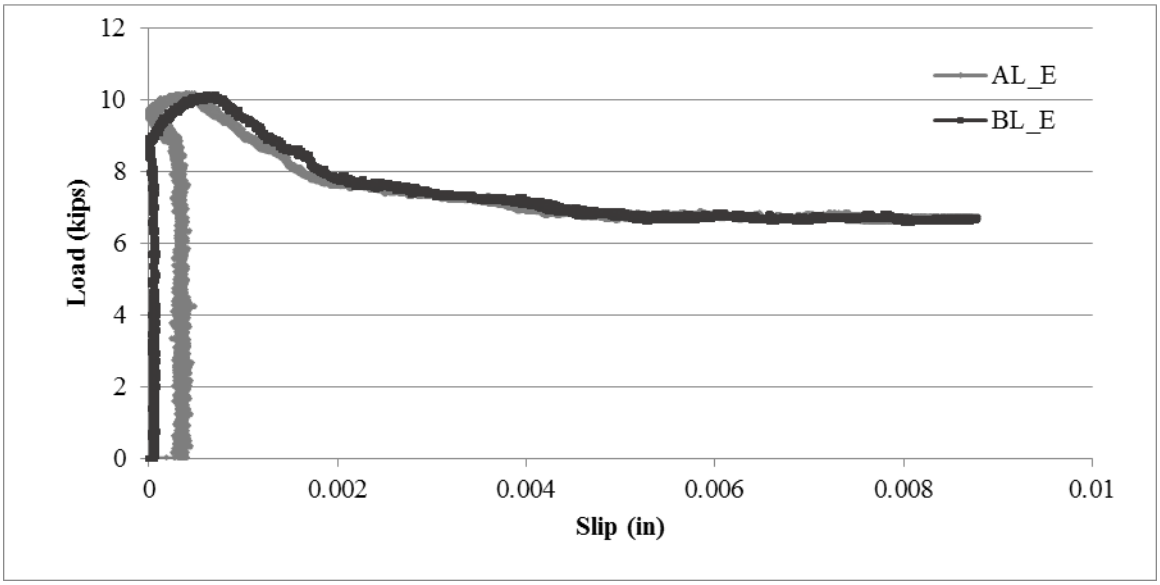

Figure 4.6: Beam H-U-S-1 load versus slip on failed end

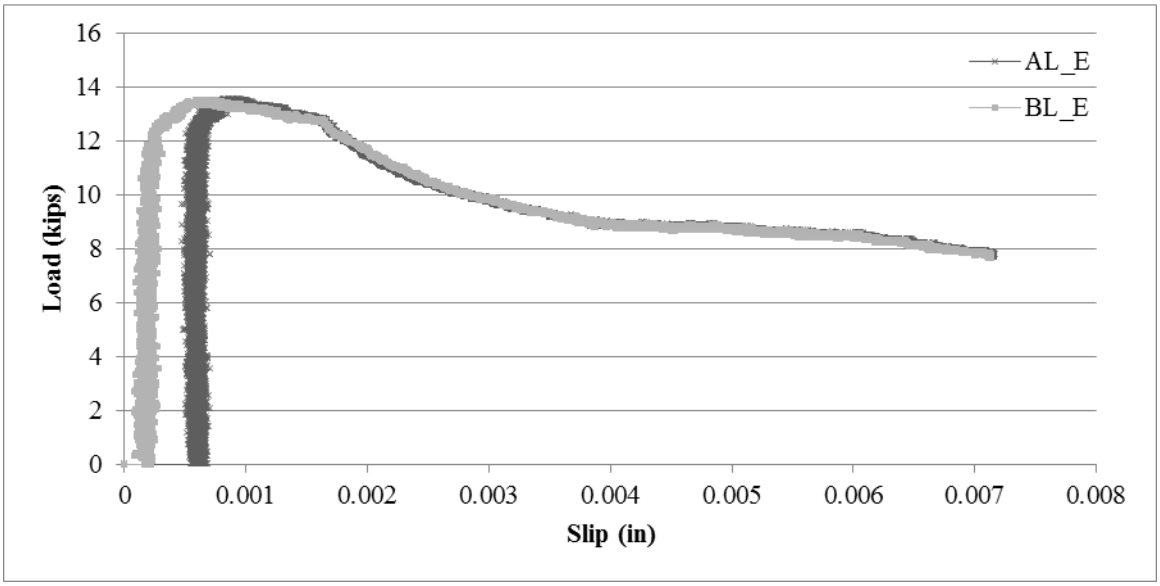

Figure 4.7: Beam H-U-S-2 load versus slip on failed end

The slip behavior of the repaired beams before slip initiation is similar to the slip behavior of the unrepaired beams, but the behavior after slip initiation is slightly different. Upon slip initiation, the load does not drop immediately, but is maintained for some time. After more loading, cracking began to occur in the repair causing an increased rate of slip as the loading decreased up to beam failure. This is due to the confining force provided by the repair that improves bond behavior even after slip initiation. Figure 4.8 shows the load versus slip results for beam N-R1-S. When the beam reached the peak load of 22.44 kips, the beam maintained this load until it reached roughly 0.22 in. and the bar continued to slip at an increasing rate under decreasing load up to beam failure. At the failure of the beam, the slip at the end reached a maximum of roughly 0.5 in. The displacement measured at the end of the bar is partially due to bending of the beam towards the end of the loading.

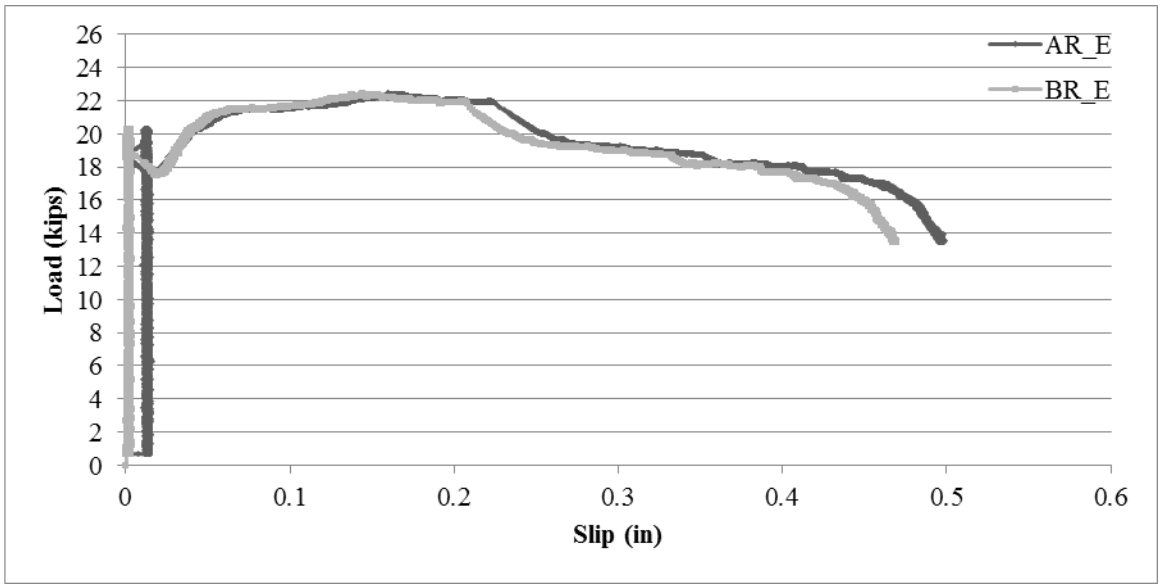

Figure 4.8: Beam N-R1-S load versus slip on failed end

Figure 4.9 shows the load versus slip results for beam H-R1-S. The peak load was not sustained for as long in the high corroded repaired beam, but it still maintained the peak load for about 0.05 in. of slip before the load began to decrease. The slip continued to increase with decreasing load up to failure.

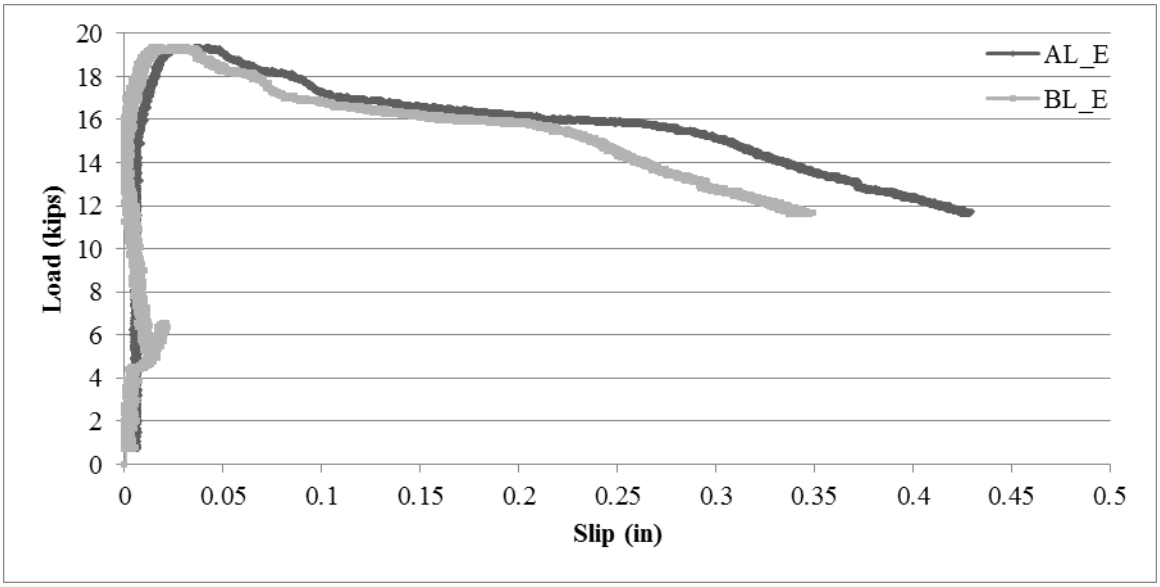

Figure 4.9: Beam H-R1-S load versus slip on failed end

4.3.2 Bond Stress Behavior

Strain gauges were applied to both bars in the notches to measure the strain through the duration of each test. The strain was then used to calculate the bond. Equation 4-1 was used to calculate the average bond stress in the bars under the loading.

$$u = \frac{A_b(\Delta f_s)}{\pi d_b l} = \frac{(\Delta f_s) d_b}{4l} \qquad \textbf{Equation 4-1}$$

where: u is the average bond strength (ksi)

A_b is the cross-sectional rea of the steel bar (in^2)

Δf_s is the change in steel stress in the bar along the length (ksi)

d_b is the bar diameter (in.)

l is the length of the bar between the reading and the free end (in.)

It is assumed that the strain in the bar at the free end is zero; therefore, the change in strain was the strain reading at the notch. The distance between the free end and the location of the strain gauge was used for the length in which to determine the average stress. The strain values were converted to stress values by multiplying the strain by the modulus of elasticity of the steel, which is equal to 29,000 ksi.

The following figures show the bond stress behavior with increasing load all four locations (AR, BR, AL, and BL) in each beam. The bond stress behavior was found to be similar for all of the static tests. In each test, the stress was shown to increase linearly with load until it reached the peak load. At this time, the bond stress dropped due to loss of bond between the reinforcement and the surrounding concrete. The portion of the stress after the beam reached the peak load was removed from the graphs for clarity.

Figure 4.10 shows the bond stress vs. load for beam N-U-S. The bond stress increases linearly until the first crack formed. The stress remains constant for this portion of the loading, and then continues to increase with continued loading until reaching the peak load. The maximum bond stress at the peak load varied between 0.225 and 0.4 ksi.

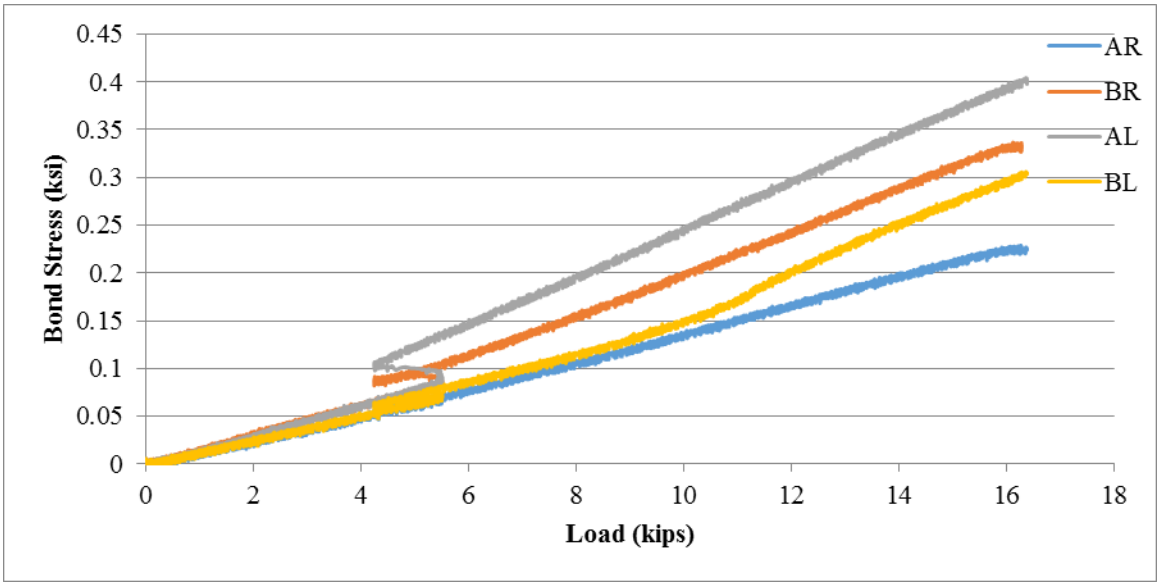

Figure 4.10: Beam N-U-S bond stress vs. load for both bars

Figure 4.11 shows the bond stress vs. load for beam H-U-S-1. Similar to beam N-U-S, the stress increases linearly until the first cracking. Upon initial cracking, the bond stress plateaus temporarily and then continues to increase until peak loading is reached. The maximum bond stress at the peak loading varies between 0.15 ksi and 0.17 ksi, which is 48.8% less than that of beam N-U-S. This indicates a bond failure at a lower bond stress level due to bond damage caused by corrosion deterioration of the reinforcement.

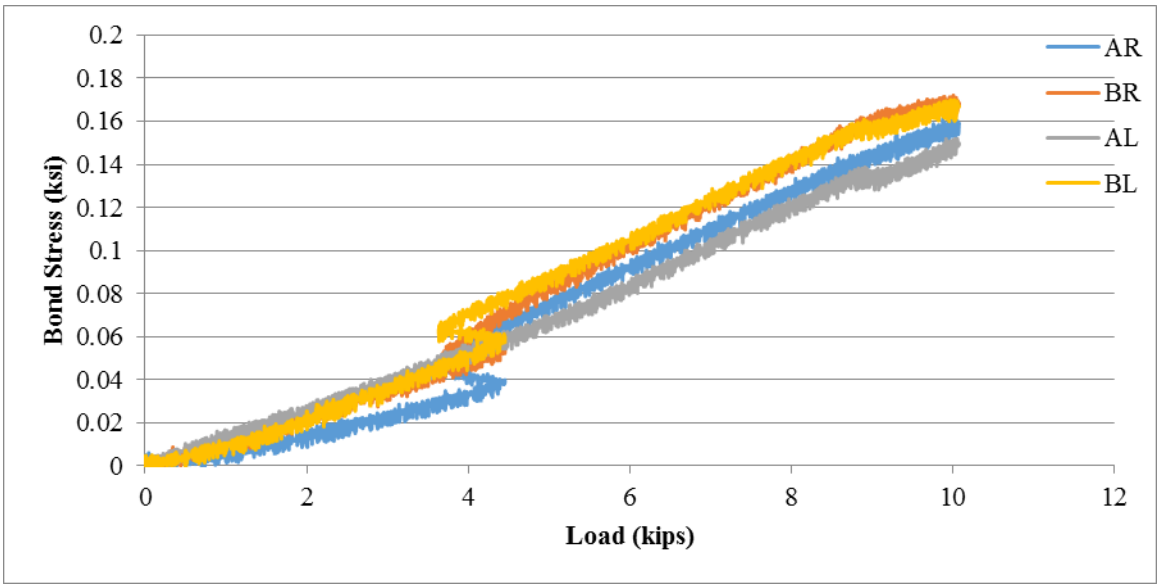

Figure 4.11: Beam H-U-S-1 load vs. stress for both bars

Figure 4.12 shows the bond stress vs. load for beam H-U-S-2. Similar to both N-U-S and M-U-S, the stress increases linearly until the first cracking. The stress plateaus momentarily upon cracking and then continues to increase until reaching the peak loading. The bond stress at peak loading varied between 0.15 ksi and 0.3 ksi for the high corroded unrepaired static test. The average maximum bond stress at the peak loading is less than that of beam N-U-S. The loss of bond stress was 28% on average less compared to the control. It was found that corrosion on average reduces the bond stress of a beam by 38.4%

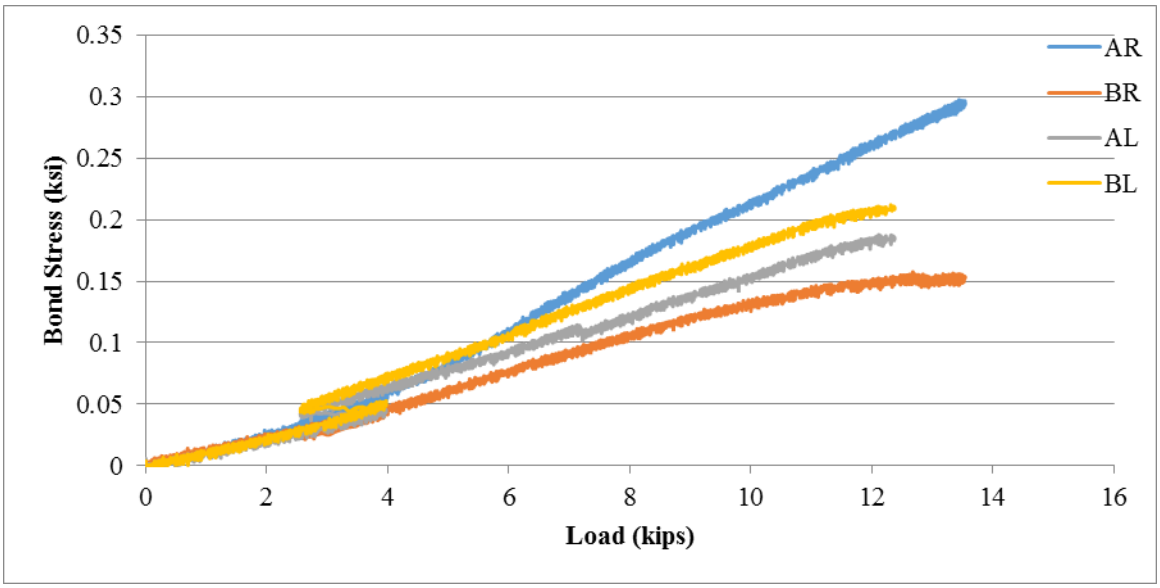

Figure 4.12: Beam H-U-S-2 load vs. stress for both bars

Figure 4.13 shows the bond stress vs. load for beam N-R1-S. Similar to the unrepaired beam tests, the bond stress increases linearly; however, it does not experience the same plateau upon cracking as the other beams did. The bond stress at peak loading varied between 0.35 ksi and 0.4 ksi for the uncorroded repaired static test. This is similar to the bond stresses at peak loading for the uncorroded unrepaired beam with an increase of 20%. The bond stress was higher than both corroded unrepaired beams, as expected. The bond stress was more evenly distributed between bars compared to the previous test results. This is most likely due to the increased stiffness of the repaired beam compared to the unrepaired beams, which allows for a more even load distribution.

Figure 4.14 shows the bond stress vs. load for beam H-R1-S. Upon initial cracking, there is a slight plateau in bond stress before it continues to increase until peak loading. The bond stress at peak loading varied between 0.29 ksi and 0.35 ksi for the high corroded repaired static test. This is higher than the bond stresses for the high corroded unrepaired

beam, roughly 42%, but only slightly higher than the uncorroded unrepaired beam, 2.4%. This indicates that the repair did benefit the stiffness of the beam to an extent, but not to its pre-corrosion condition. Similar to the uncorroded repaired beam, the stresses were more evenly distributed indicating a higher stiffness.

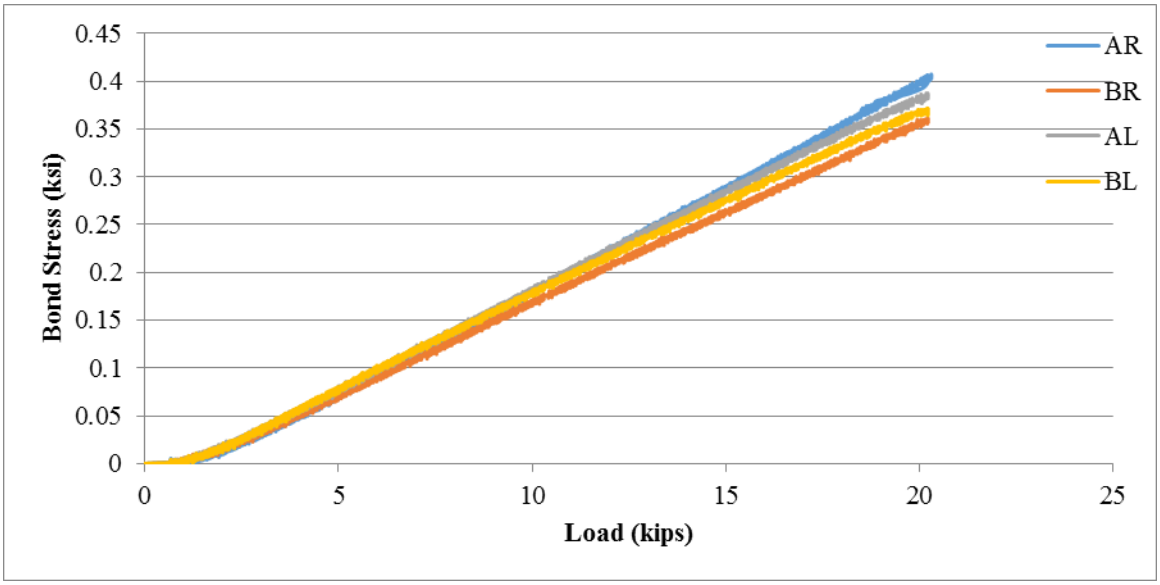

Figure 4.13: Beam N-R1-S load vs. stress for both bars

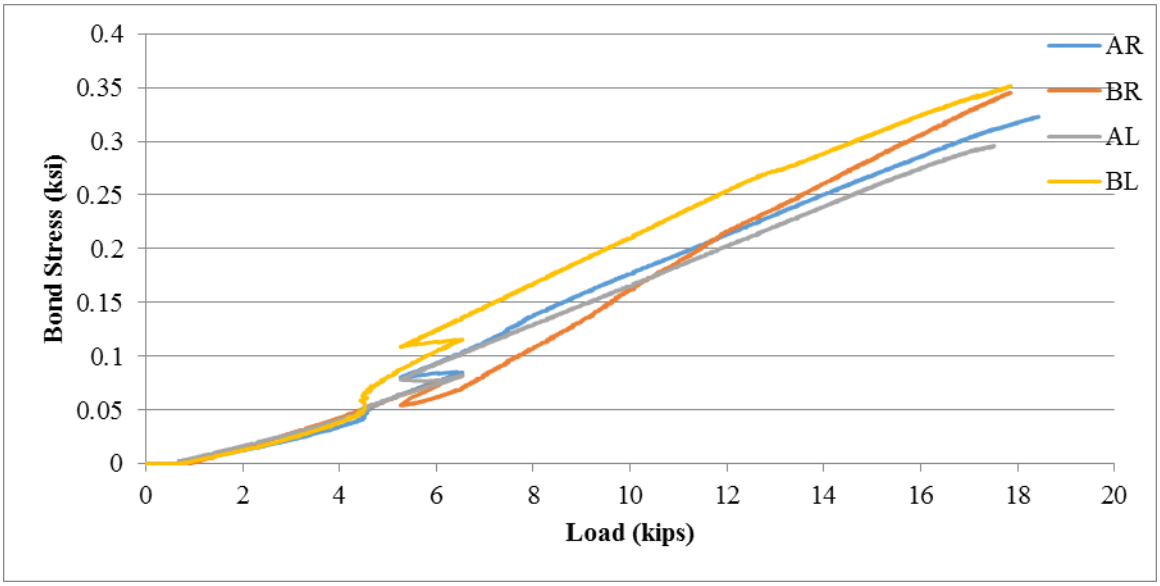

Figure 4.14: Beam H-R1-S load vs. stress for both bars

4.4 Fatigue Test Results

Twenty-four modified anchorage specimens were tested under repeated loading with varying load ranges to failure. During the testing, four beams were lost due to equipment issues. The failure behavior of these beams will be reported, but specific results will not be discussed due to the forced failure caused by equipment error. As discussed in the corrosion results section, the actual mass loss determined through the corrosion evaluation did not match the intended test matrix. The corrosion levels did not have a significant difference in mass loss results, so all of the corroded beams were lumped into one group for analysis. Figure 4.15 shows the load range vs. fatigue life curve for the unrepaired beams. The relationship between fatigue life and load range is linear, following an almost flat curve. The equations on the graph show the relationship of fatigue life to load range for each of the corrosion levels. The corroded beams were found to have a 25% reduction in fatigue strength compared to the uncorroded beam. The curve is flat, which matches the general trend of load range vs. fatigue life curves for bond behavior in the literature.

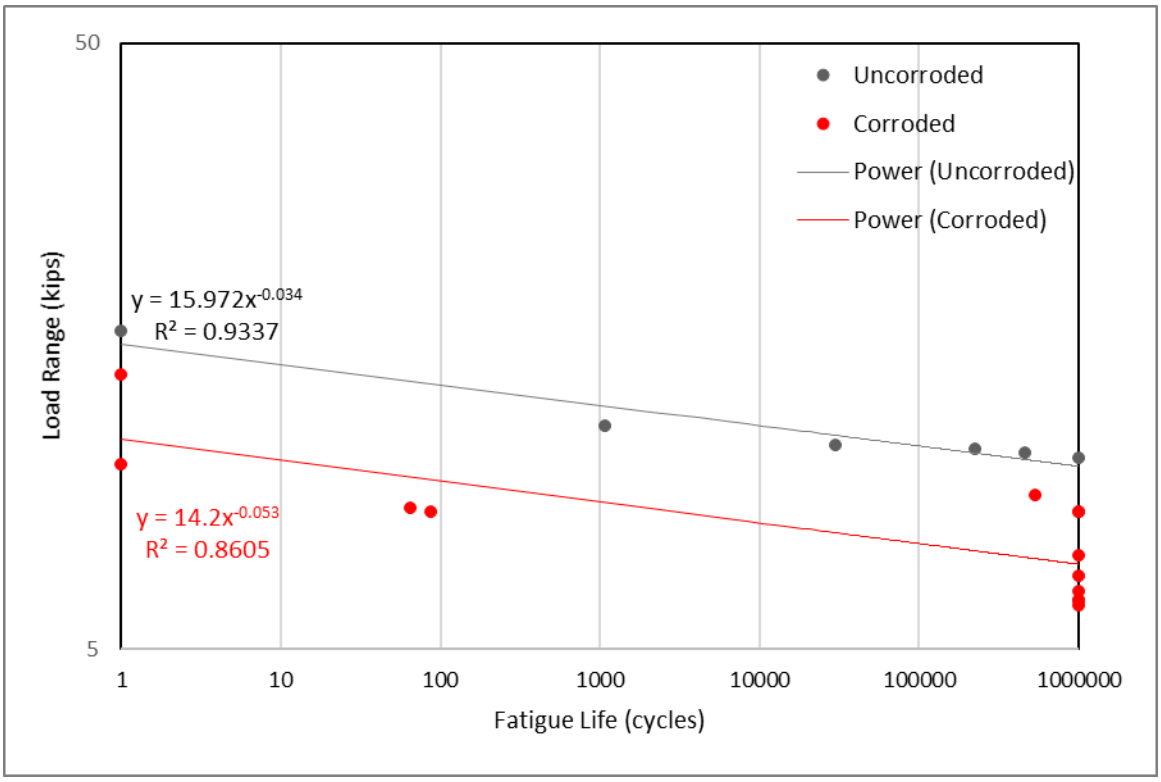

Figure 4.15: Load range vs fatigue life curve for unrepaired beams

Figure 4.16 shows the load range vs. fatigue life curve for the repaired beams. The equations at the right of the graph show the relationship of fatigue life to load range for each of tested corrosion level/repair combination. Again, the curve has a flat trendline, which is common among bond studies. The difference between high corrosion repair 1 and high corrosion repair 2 is roughly 5% indicating that there is not a significant difference in the confinement benefit provided by either grid size. The repair increases the fatigue strength by 26.6% for the high corroded beams repaired with material 1, and 20.9% for the high corroded beams repaired with material 2 compared to the fatigue strength of the uncorroded beam.

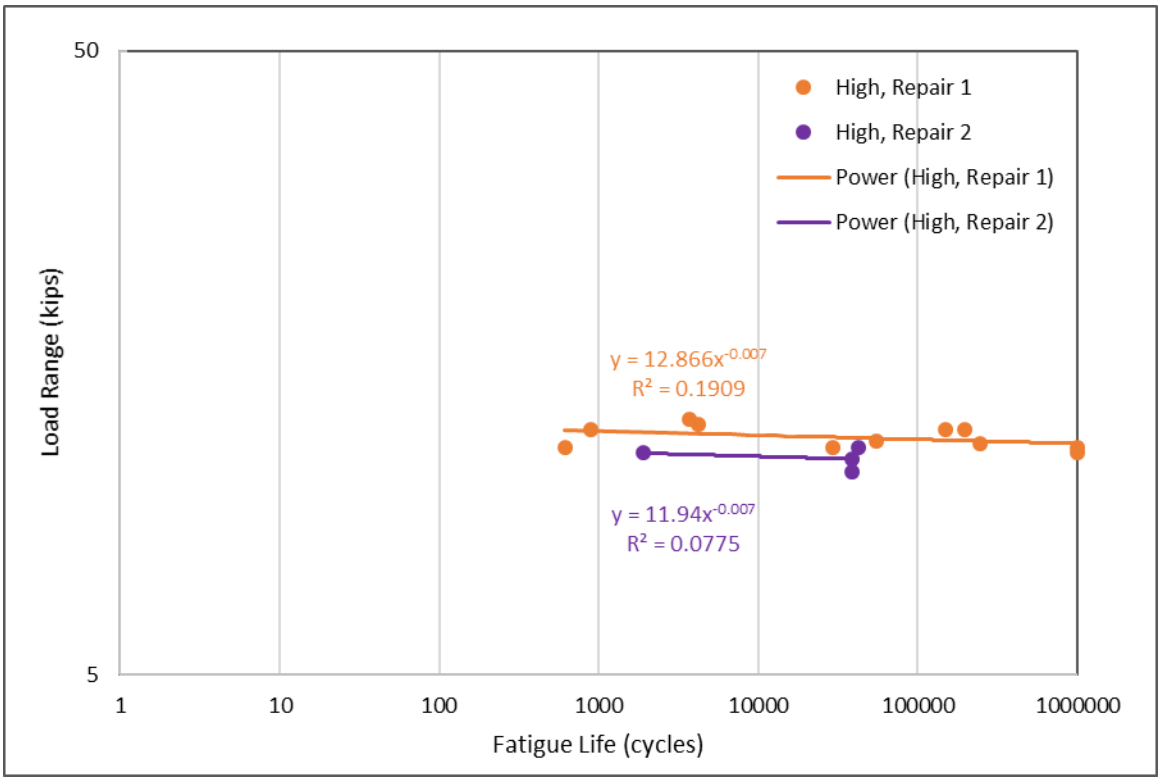

Figure 4.16: Load range vs fatigue life curve for repaired beams

The increase in fatigue strength is influenced by several factors besides corrosion level including repair mortar thickness, bond of the repair to the concrete substrate, and corrosion crack widths. These variables were not held constant between beams, but impacted the fatigue life under a given loading. The thicker the repair mortar, the easier it was for the repair to lose bond with the concrete substrate allowing the loss of bond due to corrosion crack spalling to occur. When the repair mortar was kept thin, its bond with the concrete substrate was significantly stronger. Due to the unpredictability of corrosion, the crack width and length caused by the corrosion were not kept consistent between the specimens being tested.

4.4.1 Uncorroded and Unrepaired Fatigue Beam Results

Four uncorroded and unrepaired modified anchorage specimens were tested under repeated loading with varying load ranges to failure. This section will provide an overview of the overall behavior and mode of failure, slip behavior, and strain behavior. A more detailed discussion for each beam in this group can be found in Appendix E. The beam graphs use the following nomenclature for referring to the measurement location:

- Front side (A) or back side (B)
- Left end (L) or right end (R)
- Notch/loaded end (N) and free end (E)

4.4.1.1 Overall Behavior and Mode of Failure

Table 4.3 summarizes the fatigue results for the uncorroded and unrepaired fatigue tests performed in this study. As expected, the fatigue life was directly related to the load range. Lower load ranges yielded higher fatigue lives and vice versa. The failure mode for the uncorroded and unrepaired beams was similar to the failure mode of the static beams. They showed a combination shear and splitting bond failure with shear cracking and concrete spalling caused a loss of bond of the reinforcement to the concrete.

Table 4.3: Results for uncorroded and unrepaired fatigue beams

Beam Notation	Fatigue Life (cycles)	Load Range (kip)	Maximum Load (kip)	Ratio of Load Range to Static Capacity
N-U-F-1	1,078	11.69	13.36	0.71
N-U-F-2	29,931	10.86	12.53	0.66
N-U-F-3	227,123	10.69	12.36	0.65
N-U-F-4	460,564	10.52	12.19	0.64

4.4.1.2 Load-Slip Behavior

The load-slip behavior for the uncorroded and unrepaired beams was consistent between the different beam tests in this set. The observed behavior is shown in the following figures. The graph shows a sharp bar slip near the end of the fatigue life. The failure of the beam was caused by a loss of bond due to crack propagation in the anchorage zone. Figure 4.17 displays the slip behavior over the duration of the fatigue life for beam N-U-F-1. The bar slip occurred sharply on both sides of the beam when the cracking occurred at the right support. The slip at the notch measured lower than the slip at the end of the reinforcing bar. It was determined during analysis that the LVDTs located at the loaded end were facing the center instead of the free end. Since this does not provide accurate slip readings, the values for these slips will not be used in the analysis. The slip was almost flat until just before the failure at about 99% of the fatigue life. At this time, it increased tremendously.

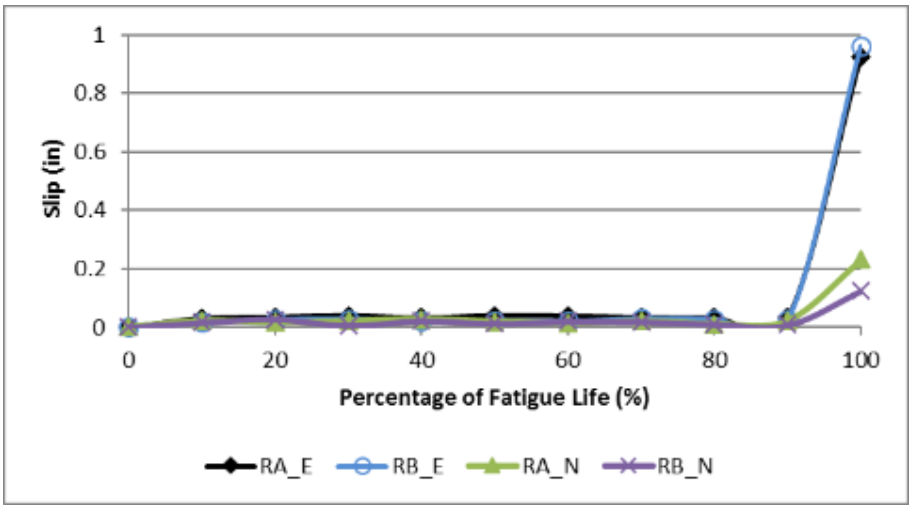

Figure 4.17: Bar slip vs. fatigue life for failed end of Beam N-U-F-1

Figure 4.18 displays the slip behavior over the duration of the fatigue life for Beam N-U-F-2. The bar slip occurred sharply on both sides of the beam when the crack at the left support increased in width.

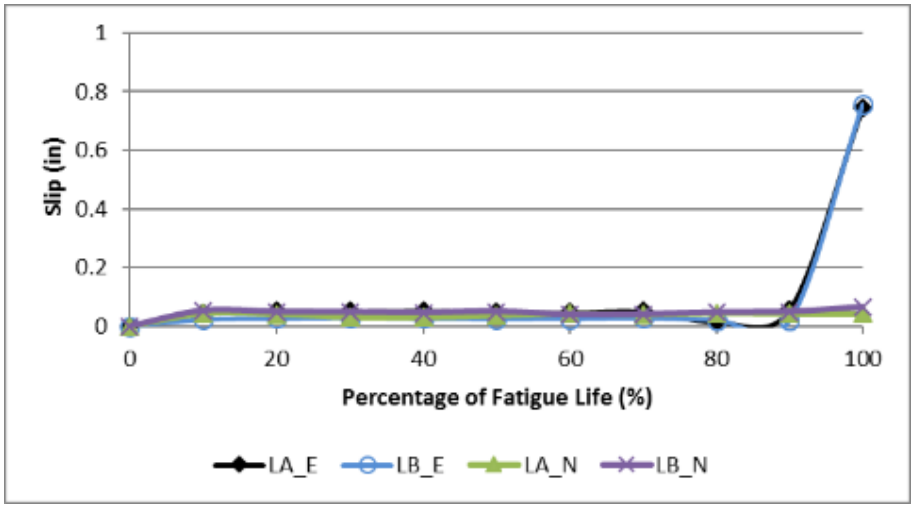

Figure 4.18: Bar slip vs. fatigue life for failed end of Beam N-U-F-2

Figure 4.19 displays the slip behavior over the duration of the fatigue life for Beam N-U-F-3. The bar slip occurred sharply on both sides of the beam when the cracking occurred at the left support.

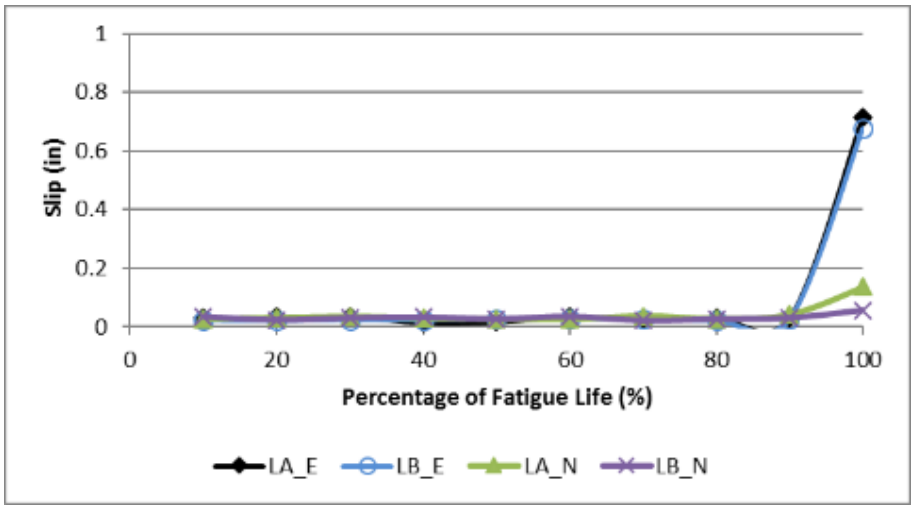

Figure 4.19: Bar slip vs. fatigue life for failed end of Beam N-U-F-3

Figure 4.20 displays the slip behavior over the duration of the fatigue life for Beam N-U-F-4. The bar slip occurred sharply on side B, whereas only a slight slip occurred on side A. This is due to a higher loss of bond on side B than on side A. The cracking on the failed side was more severe, which caused a bond failure on one side instead of both sides of the beam.

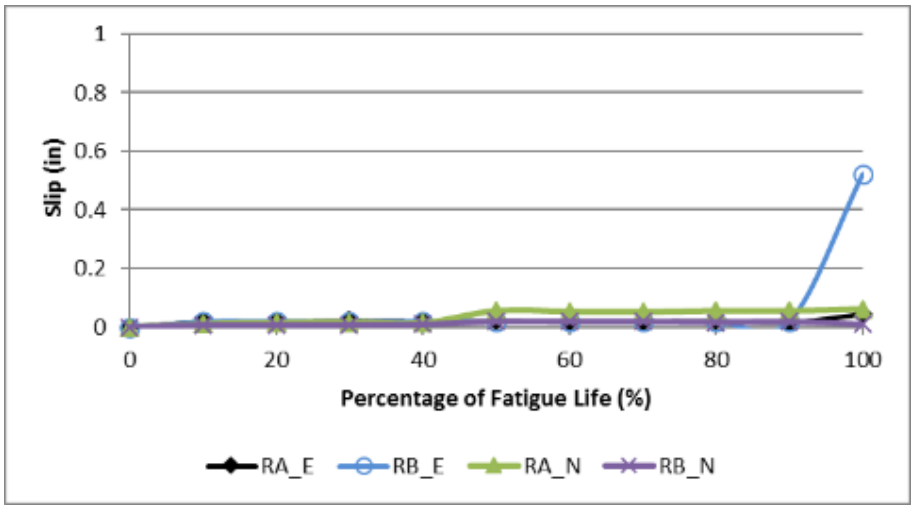

Figure 4.20: Bar slip vs. fatigue life for failed end of Beam N-U-F-4

4.4.1.3 Strain Behavior

Strain readings were taken at both bars in the notches on both ends of the beams. The following figures present the strain readings at various stages in the fatigue life for each test in this group. The beams

Figure 4.21 shows the strain behavior over the fatigue life for beam N-U-F-1. The strain remained constant between 700 and 1000 με up to the failure of the beam. At failure, the strain on the failed end increased to a maximum strain of 1800 με, while the strain on the opposite end decreased to about 300 με. Since the strain values were measured less than yield strain, the beams were in the elastic range throughout the test. Since the beams are

symmetrical, the strains were relatively the same at all readings until the slip initiated causing a drop in strain. This behavior is common for all beams in this group.

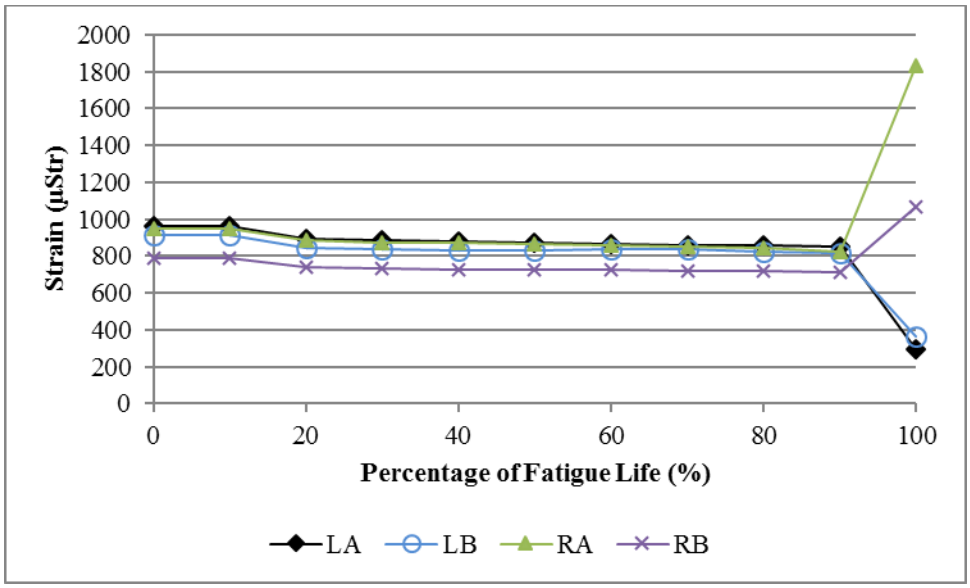

Figure 4.21: Strain vs. fatigue life for Beam N-U-F-1

Figure 4.22 shows the strain behavior over the fatigue life for beam N-U-F-2. The strain readings remain constant between 700 and 900 με up to failure and then the strain at each location decreased. The failed end decreased to between 400 and 500 με, while the opposite end decreased to between 750 and 850 με.

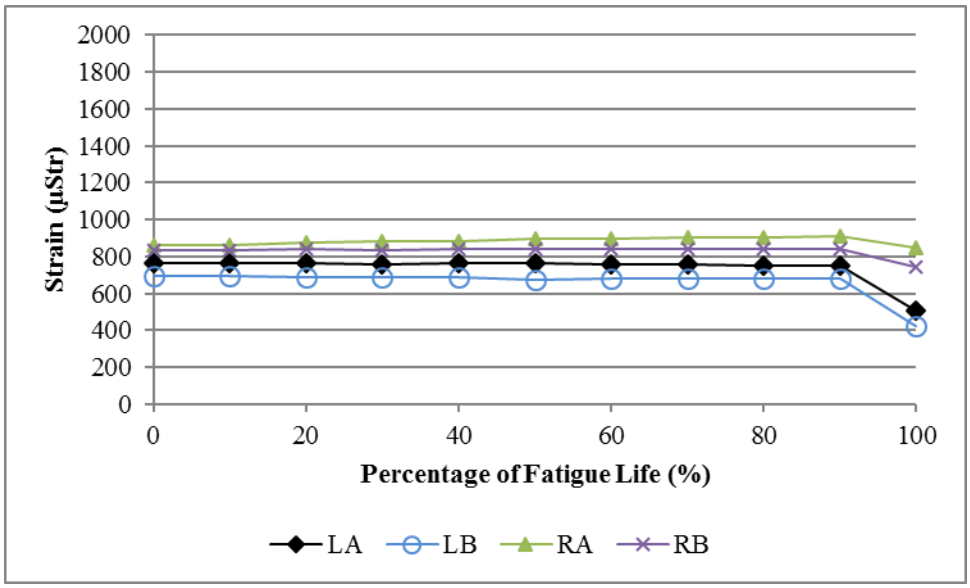

Figure 4.22: Strain vs. fatigue life for Beam N-U-F-2

Figure 4.23 shows the strain behavior over the fatigue life for beam N-U-F-3. The strain reading at the right end on side A read at 700 με, which was higher than the rest at between 450 and 500 με. Upon failure, the strain on the failed end increased to between 550 and 600 με, while the strain on the opposite end decreased to 450 με.

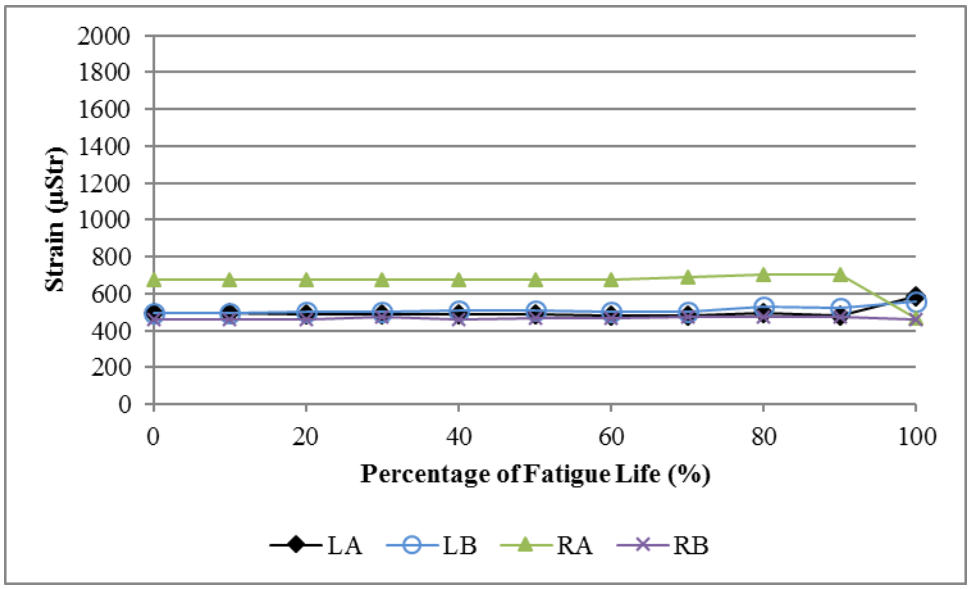

Figure 4.23: Strain vs. fatigue life for Beam N-U-F-3

Figure 4.24 shows the strain along the fatigue life for beam N-U-F-4. The strain gauge on the left end on side A failed to provide valid readings. The strain readings remained constant around 500 με until failure. At the failed end, the strain values increased reading up to 950 με whereas the opposite end remained around 500 με.

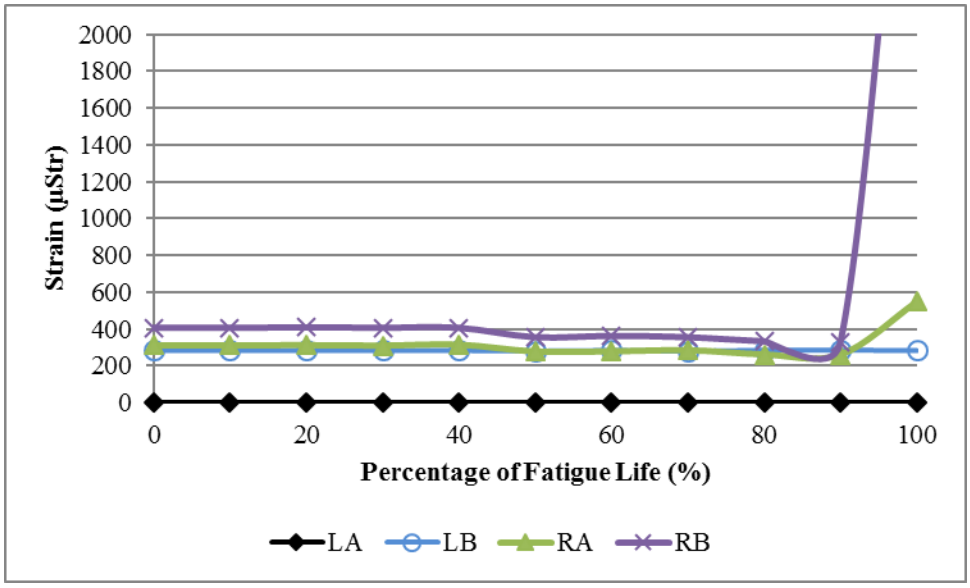

Figure 4.24: Strain vs. fatigue life for Beam N-U-F-4

4.4.2 Corroded and Unrepaired Fatigue Beam Results

Seven corroded and unrepaired modified anchorage specimens were tested under repeated loading with varying load ranges to failure. This section will provide an overview of the overall behavior and mode of failure, slip behavior, and strain behavior, followed by more detailed discussions for each beam in this group. The beam graphs use the following nomenclature for referring to the measurement location:

- Front side (A) or back side (B)
- Left end (L) or right end (R)
- Notch/loaded end (N) and free end (E)

4.4.2.1 Overall Behavior and Mode of Failure

Table 4.4 summarizes the results from the high corroded and unrepaired fatigue tests performed in this study. Four of the seven tests in this category experienced power issues; therefore, the results are inconclusive for determining fatigue behavior of corroded and unrepaired beams. The beam failure behavior is still presented in the following sections; however, the failures resulted from a large force applied at the power outage, so the results will not be discussed. Beams H-U-F-5 and H-U-F-6 failed shortly into testing. The corrosion cracks from the accelerated corrosion process caused an early loss of bond with little fatigue loading. Each of the beams in this set experienced a splitting bond failure due to the spalling of the cover below the bar and longitudinal cracking in the anchorage zone due to corrosion. Detailed descriptions and pictures for each beam in this group can be found in Appendix F.

Table 4.4: Results for corroded and unrepaired fatigue beams

Beam Notation	Fatigue Life (cycles)	Load Range (kip)	Maximum Load (kip)	Actual Mass Loss (%)
H-U-F-1	Power Outage	7.72	9.39	20.64
H-U-F-2	Power Outage	8.43	10.1	22.18
H-U-F-3	Controller Issue	8.98	10.65	16.83
H-U-F-4	539,787	8.98	10.65	14.27
H-U-F-5	65	8.55	10.22	14.78
H-U-F-6	88	8.41	10.08	15.76
H-U-F-7	Power Outage	5.60	7.27	14.63

4.4.2.2 Load-Slip Behavior

There were equipment issues with beams H-U-F-1, H-U-F-2, H-U-F-3, and H-U-F-7; therefore, these beams will not be analyzed due to skewed results. The load slip behavior for beams H-U-F-4 (Figure 4.25), H-U-F-5 (Figure 4.26) and H-U-F-6 (Figure 4.27) was

similar. There was little slip up to the point of beam failure. Once slip was initiated, the beam failed shortly after. It was determined during analysis that the LVDTs located at the loaded end were facing the center instead of the free end. Since this does not provide accurate slip readings, the values for these slips will not be used in the analysis. The maximum slip ranged from 0.15 in. to 0.6 in. between the beams in this group.

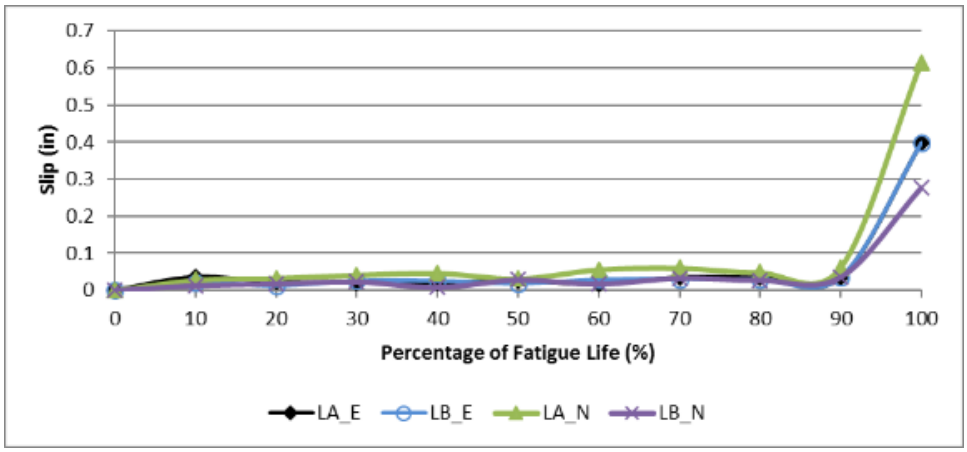

Figure 4.25: Bar slip vs. fatigue life for failed end of Beam H-U-F-4

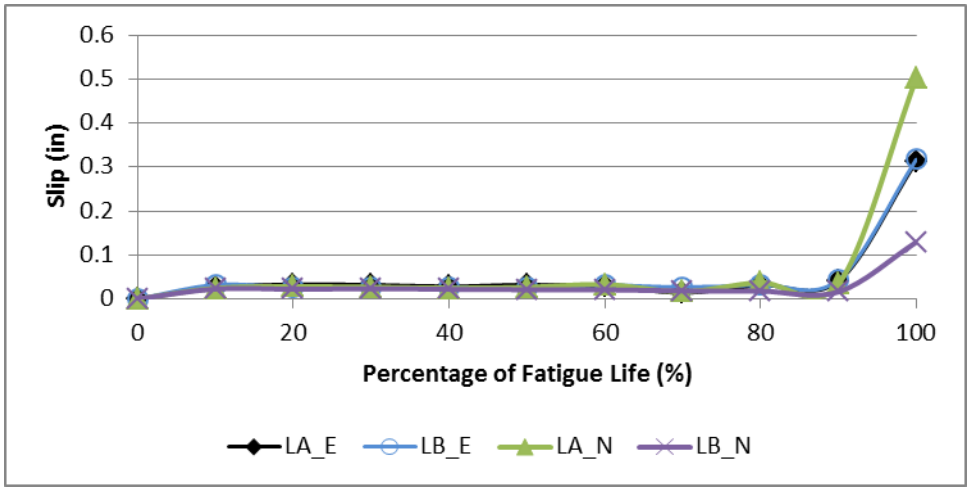

Figure 4.26: Bar slip vs. fatigue life for failed end of Beam H-U-F-5

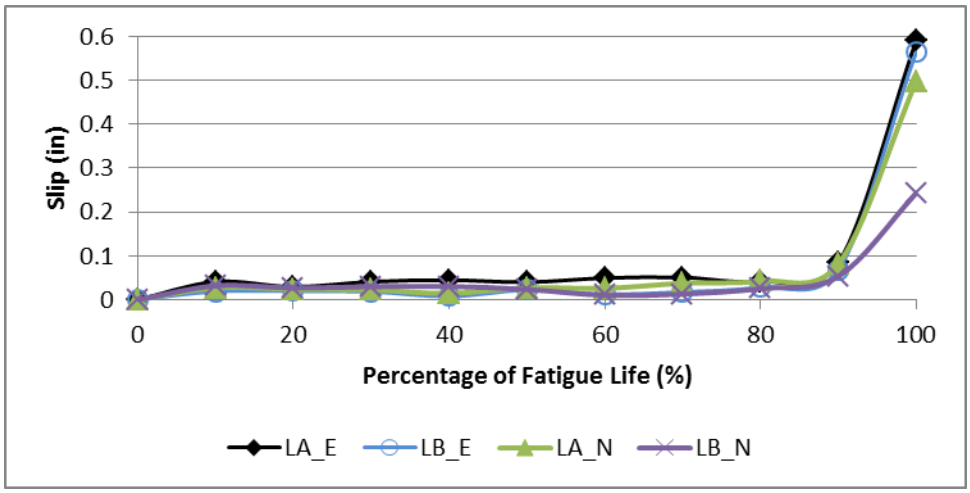

Figure 4.27: Bar slip vs. fatigue life for failed end of Beam H-U-F-6

4.4.2.3 Strain Behavior

Strain readings were taken at both bars in the notches on both ends of the beams. The following figures present the strain readings at various stages in the fatigue life for each test in this group.

There were equipment issues with beams H-U-F-1, H-U-F-2, H-U-F-3, and H-U-F-7; therefore, these beams will not be analyzed due to skewed results. Figure 4.28 shows the strain behavior over the fatigue life for beam H-U-F-4. The strain values were constant throughout the test with side A ranging from 350 to 400 με and side B ranging from 250 to 300 με. Upon failure, the failed end on side B increased to 300 με and side A remained fairly constant. On the opposite end, both sides decreased to strain values between 150 and 200 με.

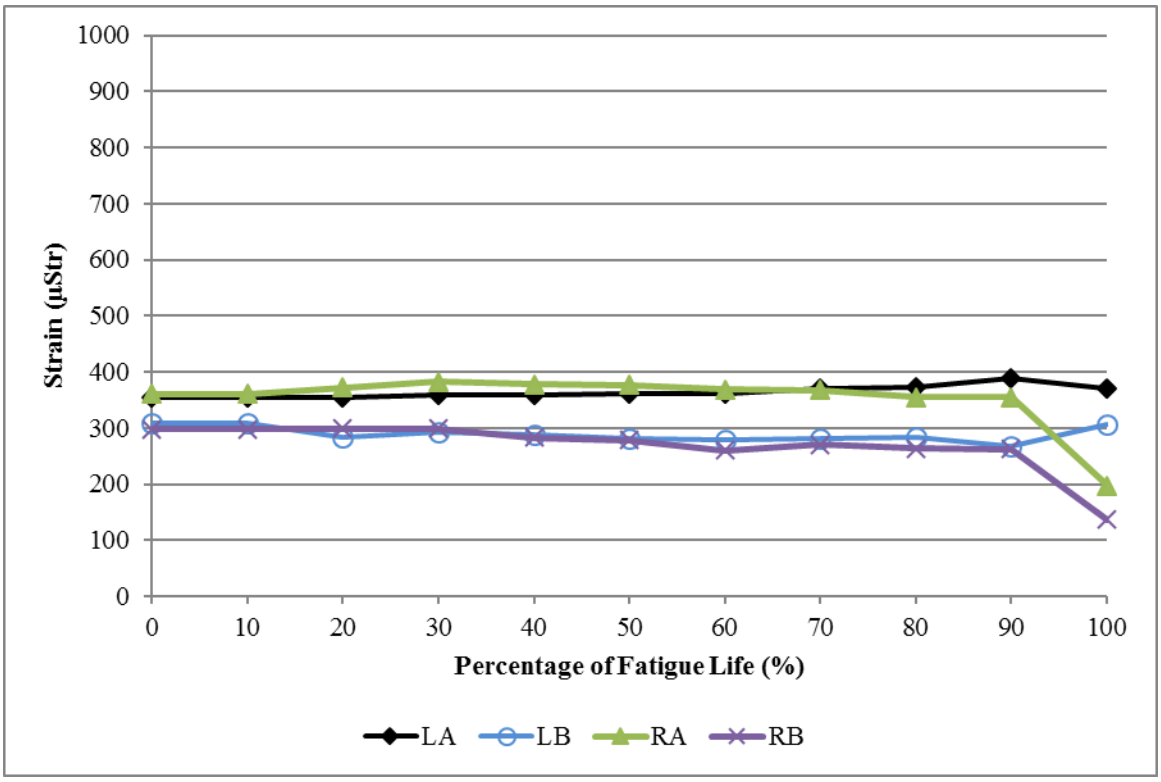

Figure 4.28: Strain vs. fatigue life for Beam H-U-F-4

Figure 4.29 shows the strain behavior over the fatigue life for beam H-U-F-5. The strain increased throughout the duration of the fatigue life up to the point of failure. Upon failure, the failed end increased in strain slightly, while the strain on the opposite end dropped. This beam failed shortly into the testing, so the strain was just developing when the bar slipped, dropping the bond stress and failing the beam.

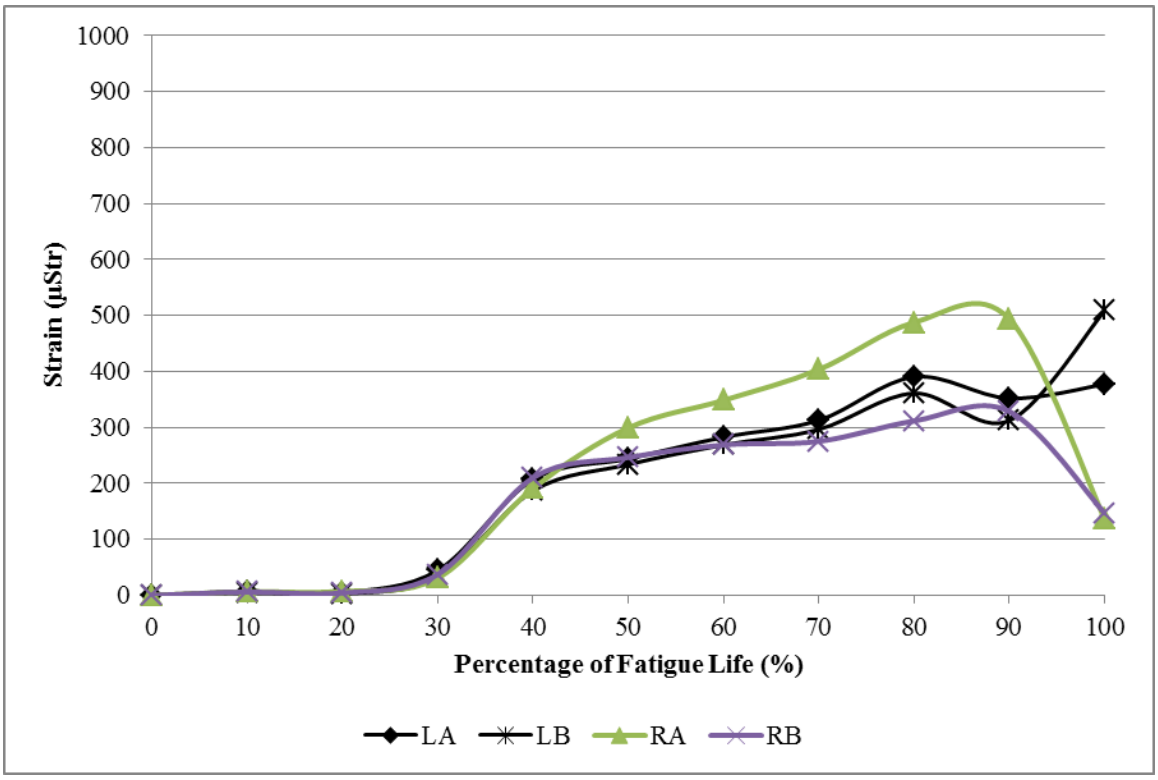

Figure 4.29: Strain vs. fatigue life for Beam H-U-F-5

Figure 4.30 shows the strain behavior over the fatigue life for beam H-U-F-6. The strain on both ends of the beam increased slightly throughout the duration of the test up to roughly 500 με. Upon failure, the strain in the failed end increased up to between 2400 and 3300 με. These strain gauges broke upon failure. The opposite end decreased in strain to roughly 250 με. Similar to beam H-U-F-5, this beam failed shortly into testing, so the strain was not able to fully develop prior to failure. This explains the low strain readings at the start of the test.

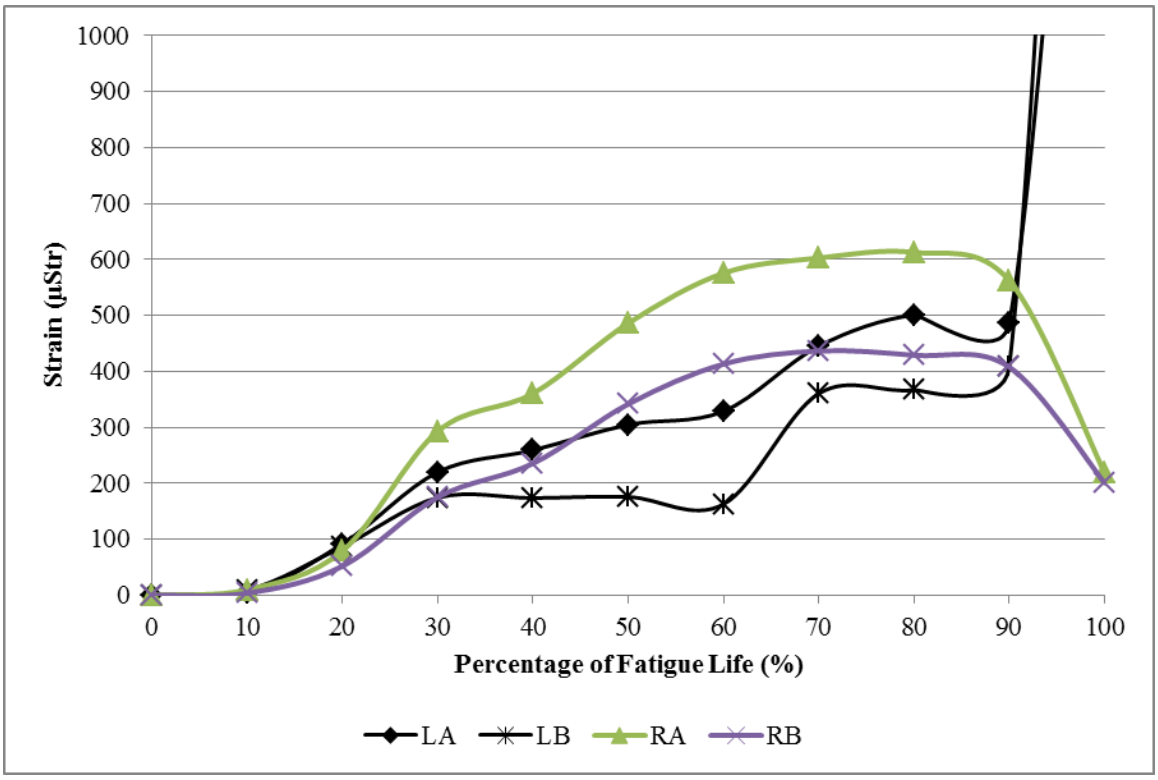

Figure 4.30: Strain vs. fatigue life for Beam H-U-F-6

4.4.3 Corroded and Repaired Fatigue Beams

Thirteen corroded and repaired (nine with repair 1 and four with repair 2) modified anchorage specimens were tested under repeated loading with varying load ranges to failure. This section will provide an overview of the overall behavior and mode of failure, slip behavior, and strain behavior. A more detailed discussion for each beam in this group can be found in Appendix F. The beam graphs use the following nomenclature for referring to the measurement location:

- Front side (A) or back side (B)
- Left end (L) or right end (R)
- Notch/loaded end (N) and free end (E)

4.4.3.1 Overall Behavior and Mode of FailureTable 4.5 summarizes the results from the mild corroded and repaired fatigue tests performed in this study. Improved post slip behavior was observed for all the beams in this group. This will be discussed in the following sections. The repair was removed after failure to observe the cracking of the beam beneath. It was found that the cracks that formed in the beam propagated through the repair to the exterior. For the beams where the repair mortar was applied too thick, the cracking in the beam caused the repair to debond from the concrete substrate instead of propagating the cracks through to the surface of the repair.

Table 4.5: Results for mild corroded and repaired fatigue beams

Beam Notation	Fatigue Life (cycles)	Load Range (kip)	Maximum Load (kip)	Actual Mass Loss (%)
H-R1-F-1	3,695	12.83	14.5	18.09
H-R1-F-2	894	12.33	14	17.45
H-R1-F-3	149,407	12.33	14	17.24
H-R1-F-4	55,109	11.83	13.5	18.06
H-R1-F-5	244,982	11.73	13.4	21.27
H-R1-F-6	29,223	11.58	13.25	17.48
H-R1-F-7	613	11.58	13.25	22.35
H-R1-F-8	4,198	12.58	14.25	16.96
H-R1-F-9	196,384	12.33	14	16.74
H-R2-F-1	1,915	11.33	13	22.55
H-R2-F-2	38,506	11.08	12.75	25.00
H-R2-F-3	39,023	10.58	12.25	25.12
H-R2-F-4	42,081	11.58	13.25	15.95

4.4.3.2 Load-Slip Behavior

The high corroded beams repaired with material 1 (Figure 4.31, Figure 4.32, Figure 4.33, Figure 4.34, Figure 4.35, Figure 4.36) experienced a slight slip around 80% to 90% of fatigue life. Data did not get collected for beam H-R1-F-6, so there is not a graph displaying the results for this beam. The maximum slips for beams repaired with material

1 range from 0.2 in. to 0.6 in. Slip initiation occurred at a lower number of cycles for the beams tested under higher load ranges. This explains the two main bar slip behaviors seen in the graphs. Beams with lower load ranges did not experience slip until later in the fatigue life (around 80 to 90%), whereas beams with higher load ranges experienced slip earlier in the fatigue life (around 20%). Both behaviors indicate that the repair successfully confined the concrete cover and prevented spalling, which extended the fatigue life of the beams after slip initiation.

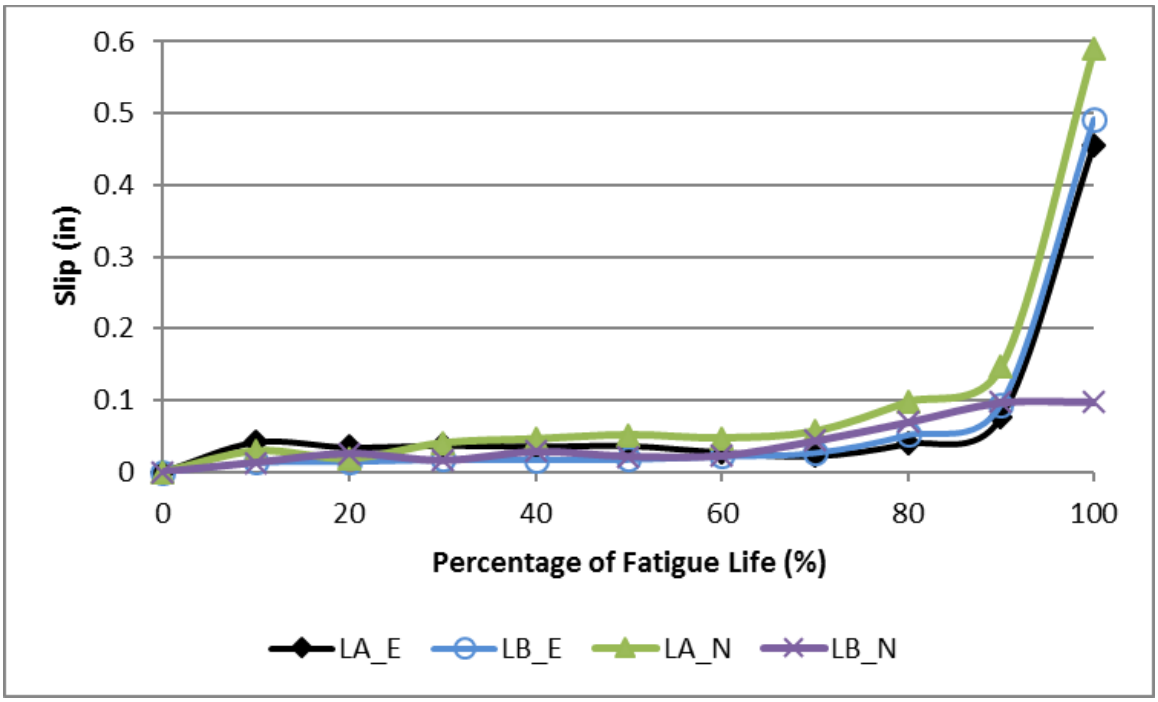

Figure 4.31: Bar slip vs. fatigue life for failed end of Beam H-R1-F-1

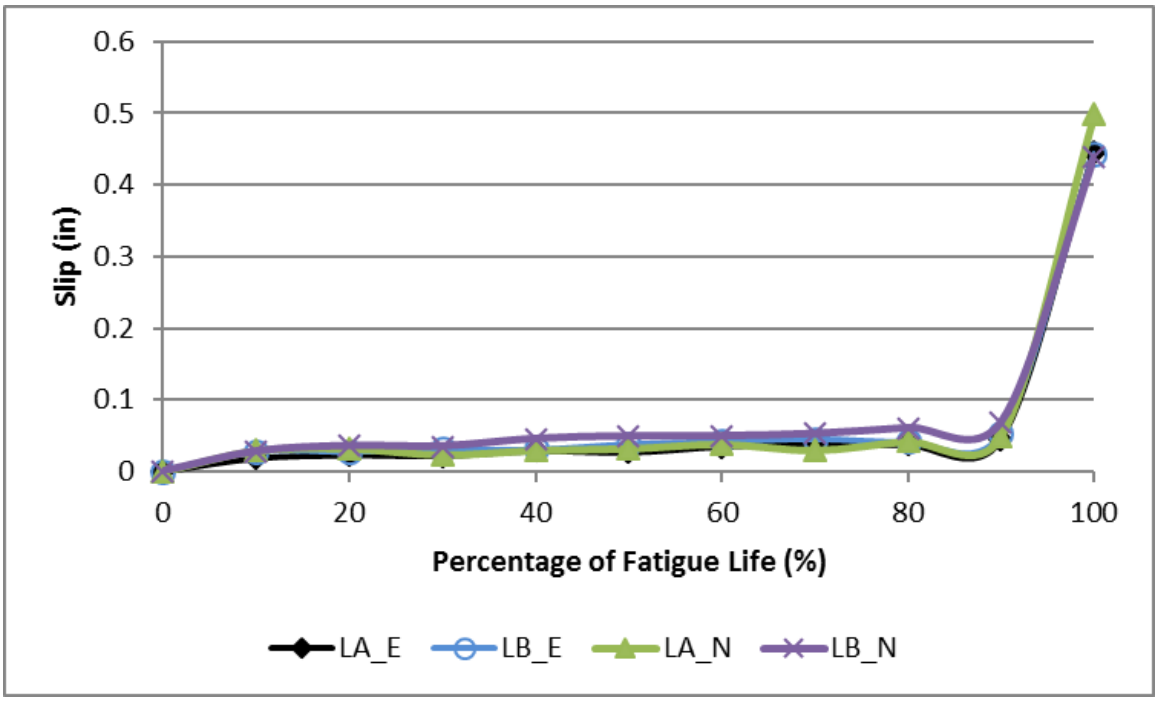

Figure 4.32: Bar slip vs. fatigue life for failed end of Beam H-R1-F-2

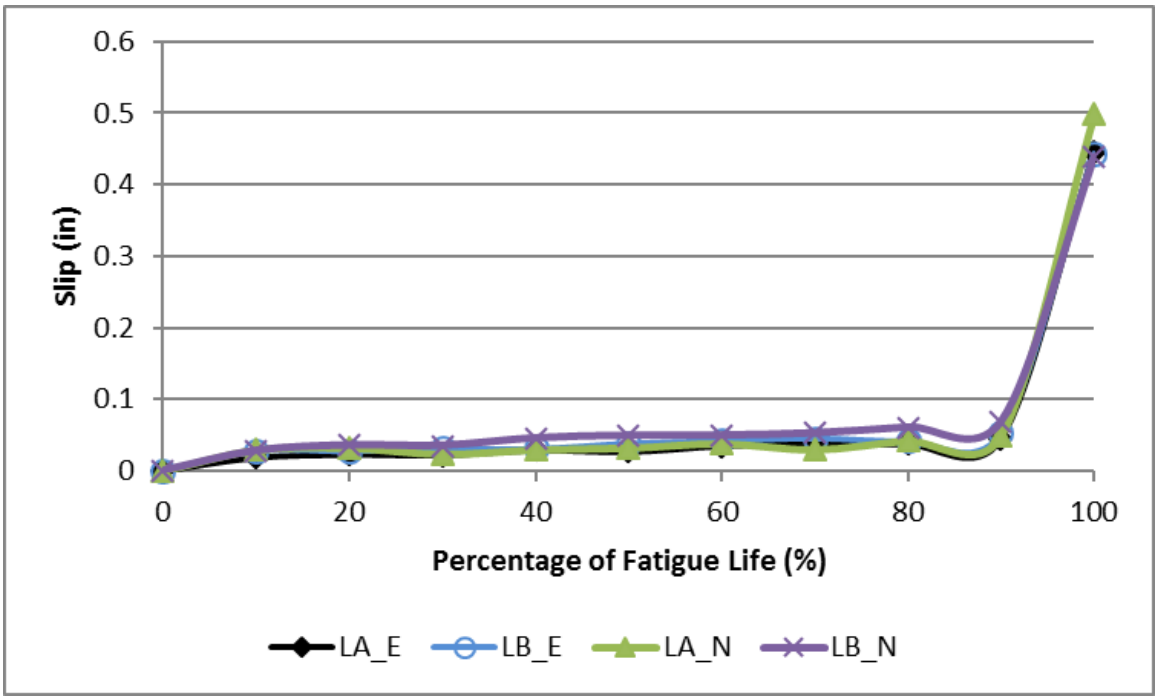

Figure 4.33: Bar slip vs. fatigue life for failed end of Beam H-R1-F-3

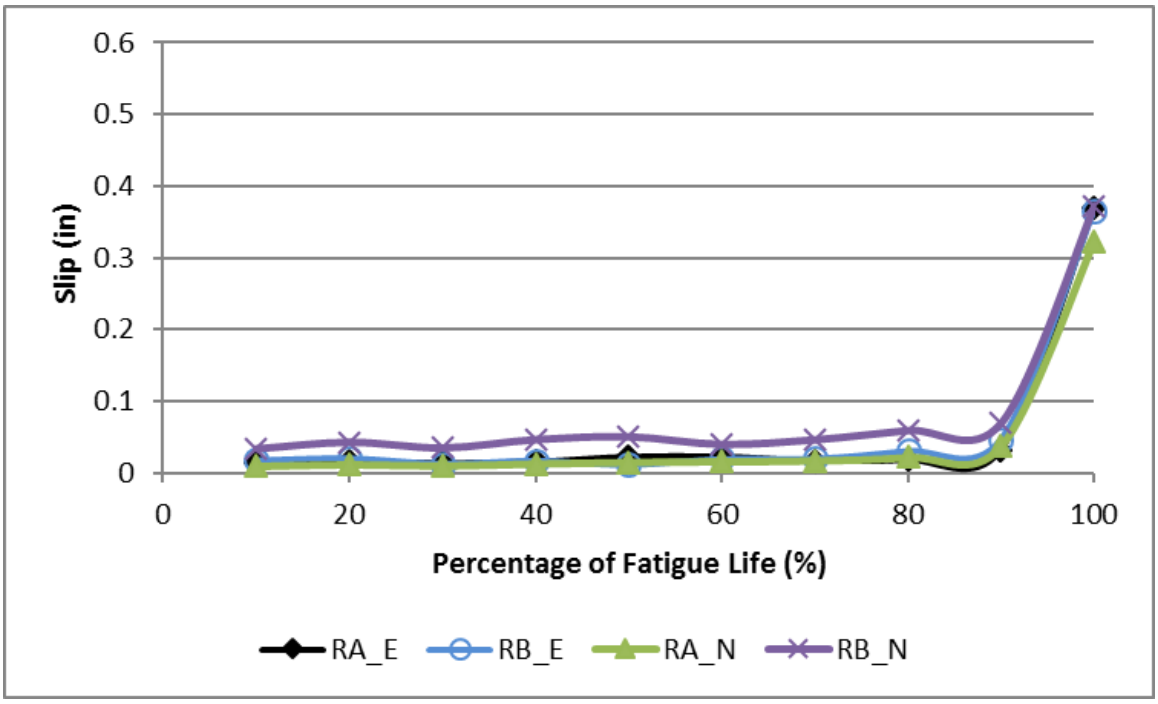

Figure 4.34: Bar slip vs. fatigue life for failed end of Beam H-R1-F-4

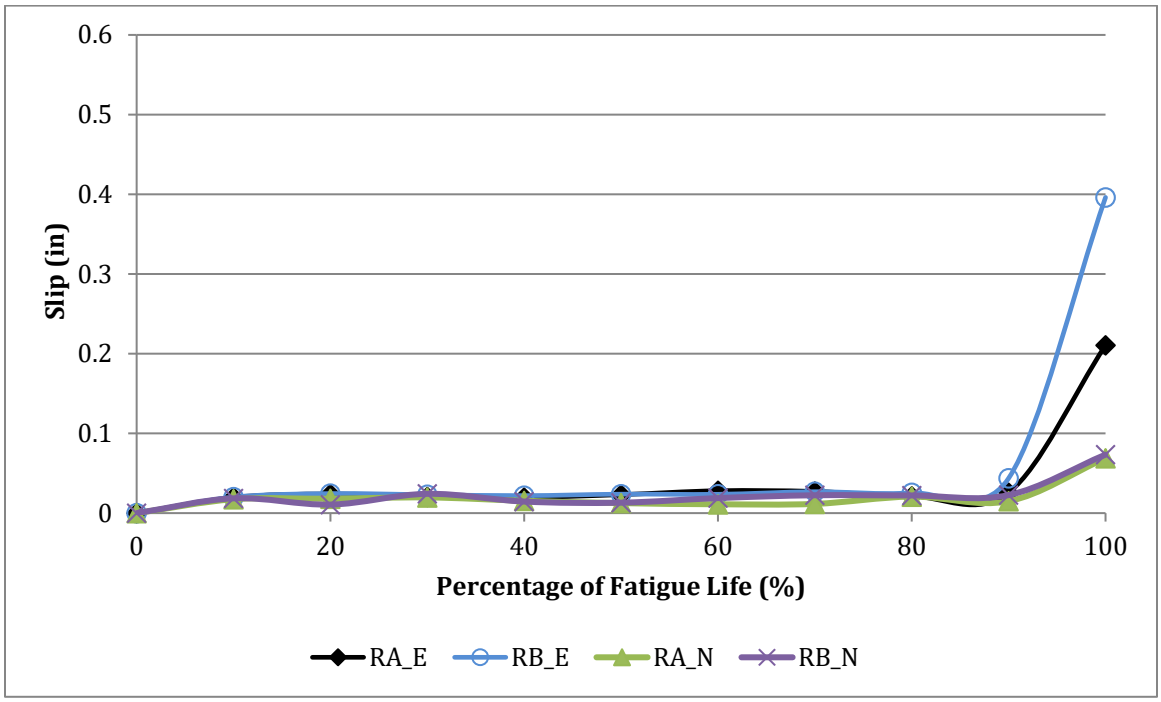

Figure 4.35: Bar slip vs. fatigue life for failed end of Beam H-R1-F-5

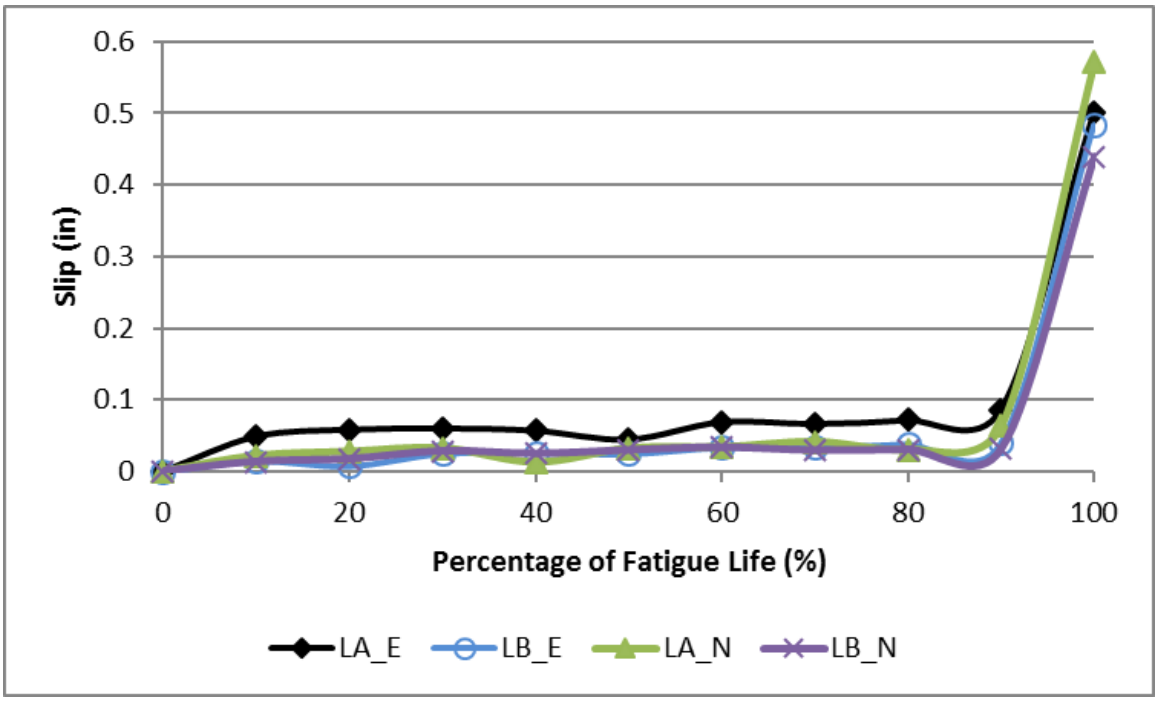

Figure 4.36: Bar slip vs. fatigue life for failed end of Beam H-R1-F-7

H-R1-F-8 (Figure 4.37) shows an increasing slip over the entire fatigue life up to the point of failure. This slow increase in slip without failure confirms the positive effect of the repair confinement on bond behavior. Shortly into the fatigue life, the bar begins to slip. Instead of the cover below the bars spalling off, the repair holds the concrete together with a confining effect extending the fatigue life after the slip was initiated slip. H-R1-F-9 (Figure 4.38) shows a slight slip at 90% of fatigue life displaying a shorter time of improved bond behavior after slip initiation

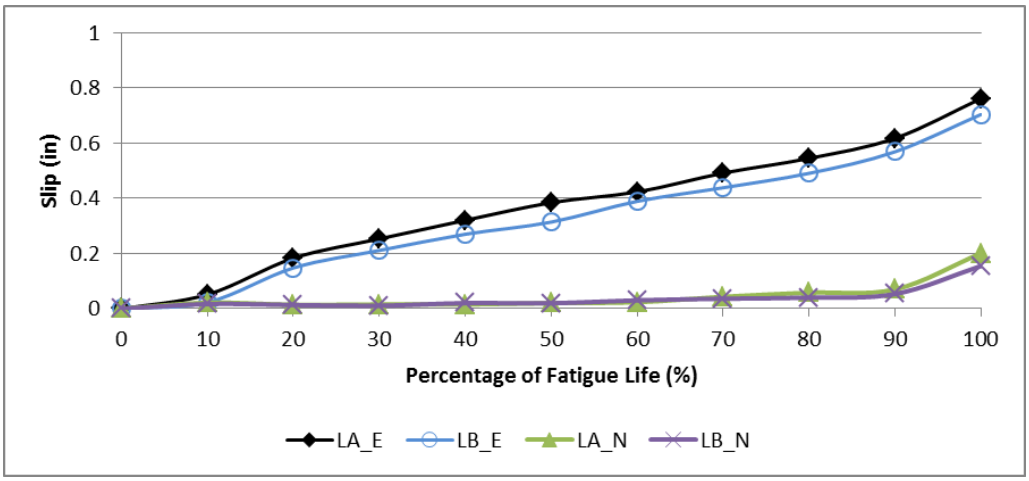

Figure 4.37: Bar slip vs. fatigue life for failed end of Beam H-R1-F-8

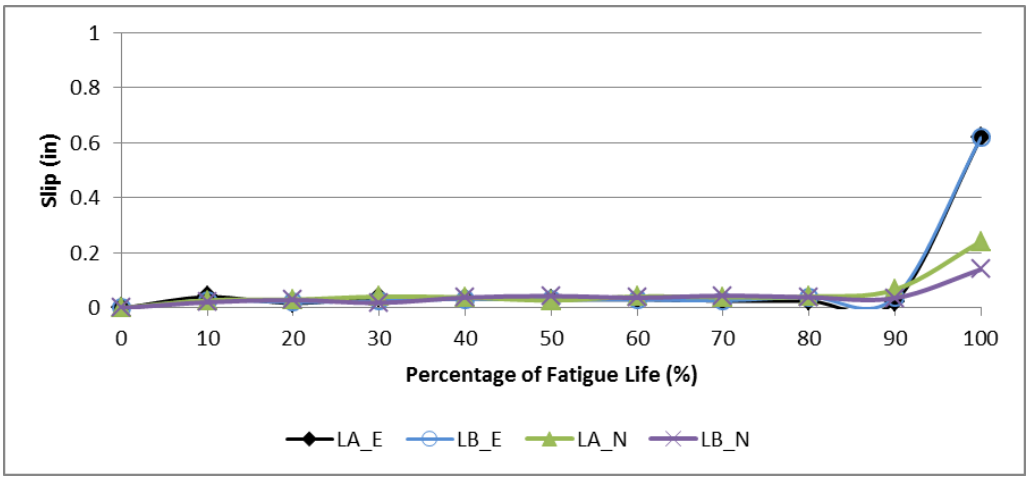

Figure 4.38: Bar slip vs. fatigue life for failed end of Beam H-R1-F-9

The high corroded beams repaired with material 2 (Figure 4.39, Figure 4.40, Figure 4.41, Figure 4.39) experienced extended fatigue life upon slip initiation due to the confinement provided by the repair. The graphs show a slow progression of linearly increasing slip with fatigue life up to the point of failure in which the slip increases sharply. The maximum slips for beams repaired with material 1 range from 0.6 in. to 0.9 in.

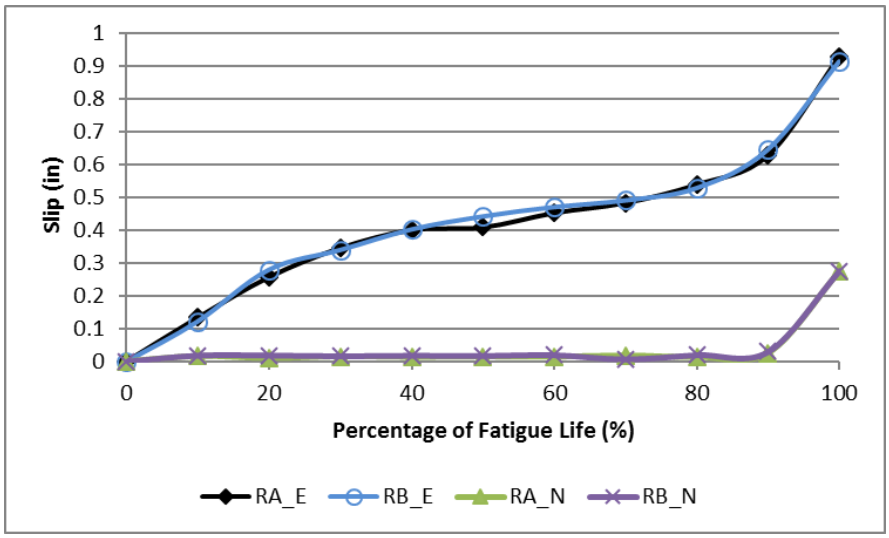

Figure 4.39: Bar slip vs. fatigue life for failed end of Beam H-R2-F-1

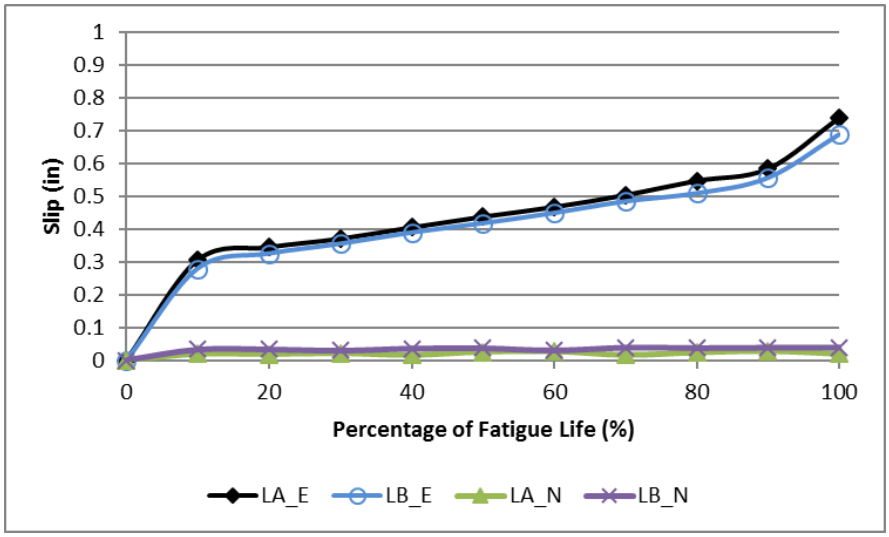

Figure 4.40: Bar slip vs. fatigue life for failed end of Beam H-R2-F-2

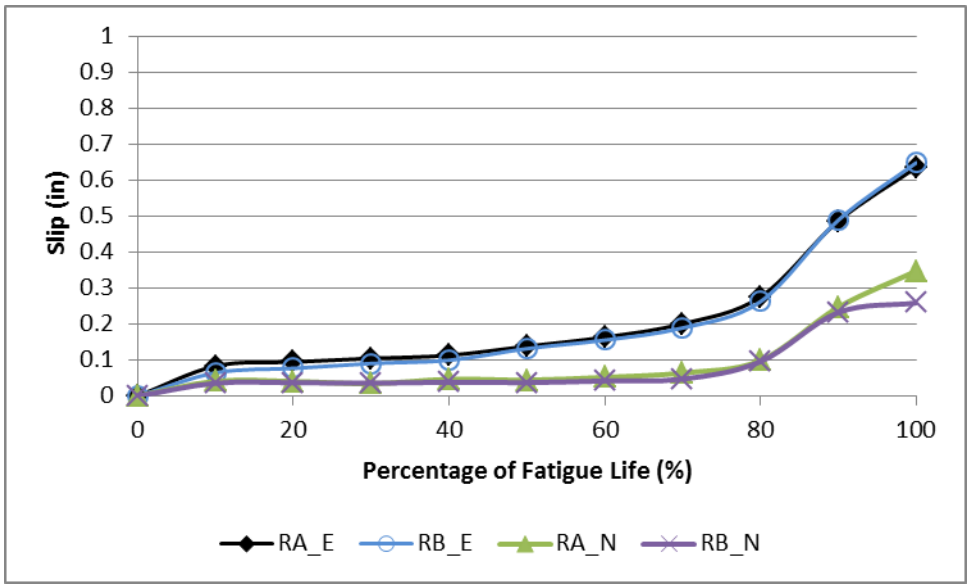

Figure 4.41: Bar slip vs. fatigue life for failed end of Beam H-R2-F-3

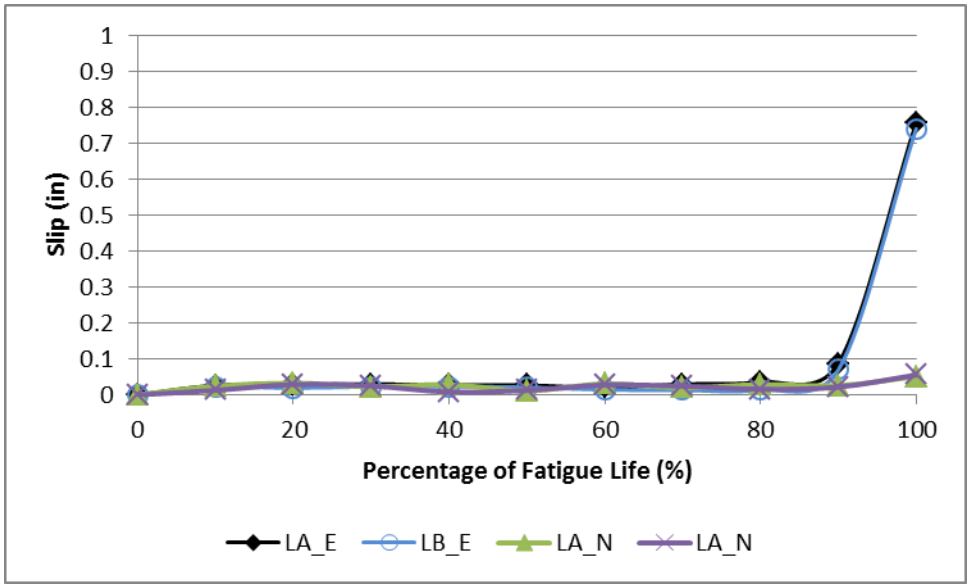

Figure 4.42: Bar slip vs. fatigue life for failed end of Beam H-R2-F-4

4.4.5.3 Strain Behavior

Figure 4.43 displays the strain over the fatigue life of beam H-R1-F-1. The strain remains constant between 700 and 800 με for the right end and between 500 and 600 με for the left end. This beam ended up failing on the left end. The strain on side A of the failed end

dropped slightly and then increased before failing, whereas the strain on side B of the failed end dropped. Both strains were between 300 and 400 με at the time of failure. The strain on the opposite end drop to between 550 and 600 με.

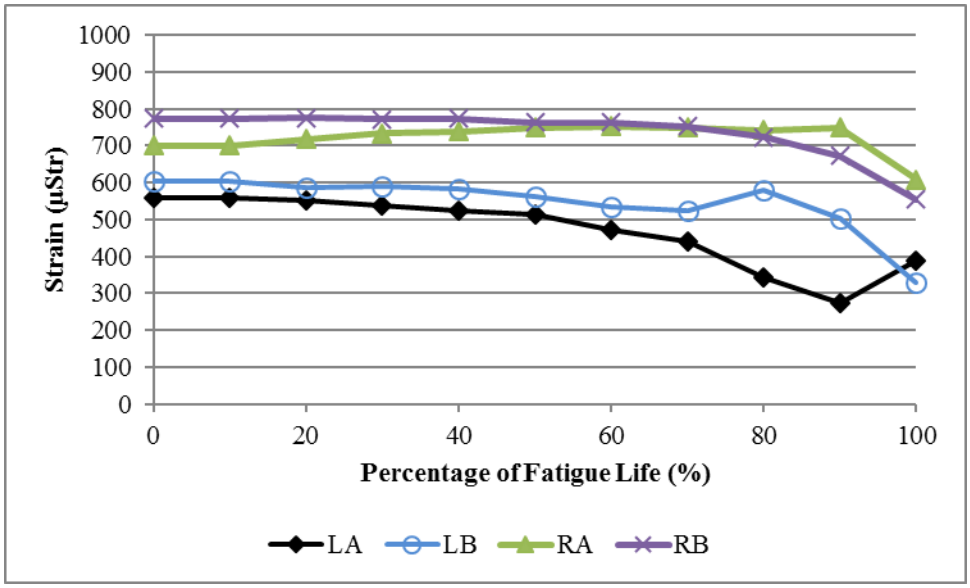

Figure 4.43: Strain vs. fatigue life for Beam H-R1-F-1

Figure 4.44 displays the strain over the fatigue life of beam H-R1-F-2. The strain remains constant around 500 με throughout the fatigue life. The strain in side A of the left end increased significantly at the point of failure to roughly 3600 με indicating the loss of bond for the other bar. As discussed previously, both bars at the left end slipped to roughly the same level upon failure. The bar on side A at the left end slipped slightly more than the bar on side B.

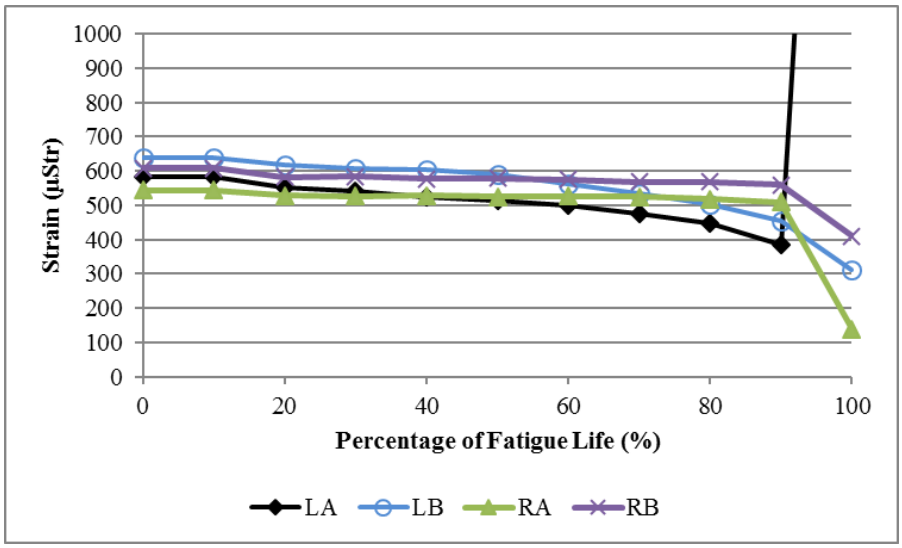

Figure 4.44: Strain vs. fatigue life for Beam H-R1-F-2

Figure 4.45 displays the strain over the fatigue life of beam H-R1-F-3. The strain remains constant for the fatigue life of the beam between 500 and 750 με, with side A on the right end slightly lower at around 250 με. Upon failure, the strain in side A of the left end (failed end) spiked and reached around 3750 με, whereas the strain in the other bars lowered slightly from the pre-failure strain.

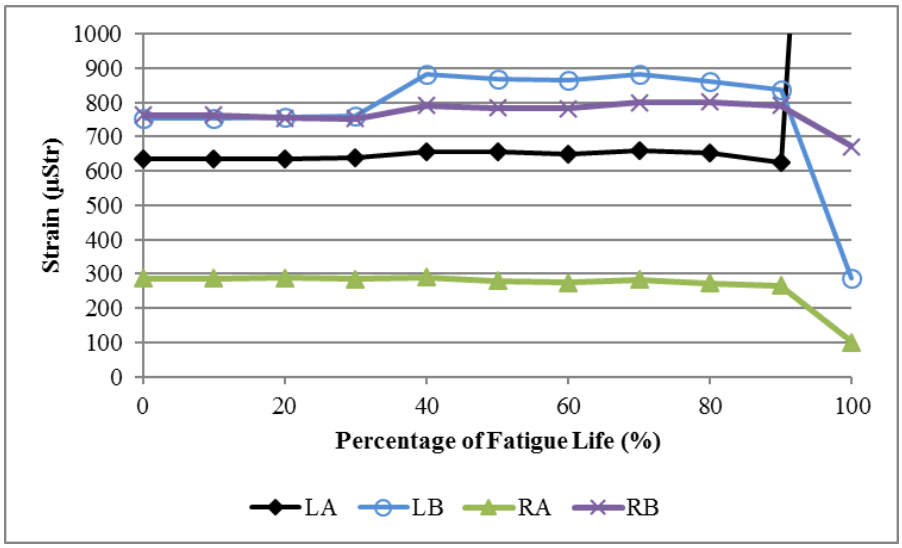

Figure 4.45: Strain vs. fatigue life for Beam H-R1-F-3

Figure 4.46 displays the strain over the fatigue life of beam H-R1-F-4. The strain on the left end remained constant between 400 and 500 με until failure and then decreased to roughly 250 με. The strain on the right end (failed end) remained constant between 590 and 710 με until failure and then decreases slightly before increasing slightly. The decrease of strain indicates a loss of bond before failure of the beam.

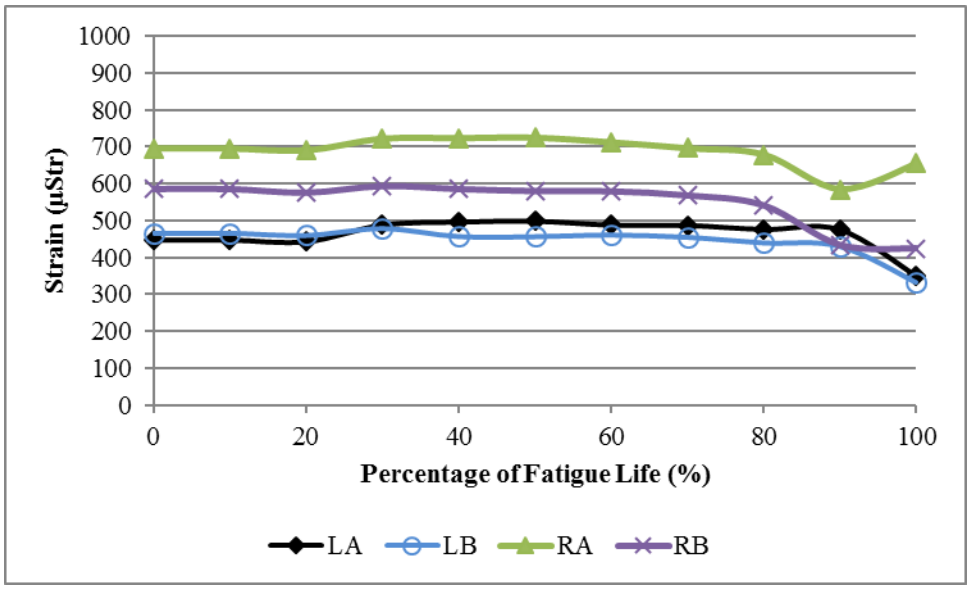

Figure 4.46: Strain vs. fatigue life for Beam H-R1-F-4

Figure 4.47 displays the strain over the fatigue life of beam H-R1-F-5. The strain remains constant for the fatigue life of the beam between 400 and 500 με, with side A on the left end slightly lower at around 300 με. Upon failure, the strain dropped at all locations to between 350 and 400 με. Data was not collected for Beam H-R1-F-6 due to a data collection error.

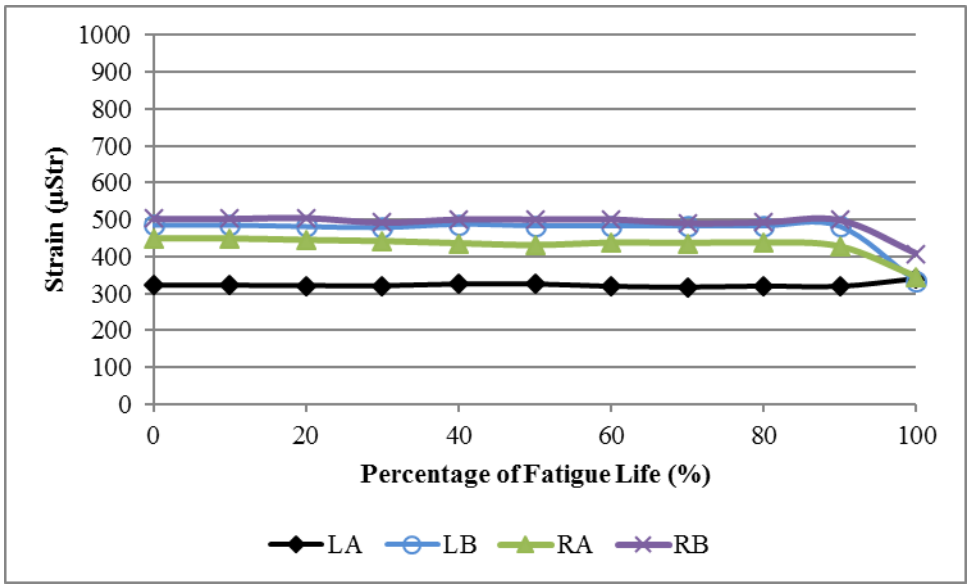

Figure 4.47: Strain vs. fatigue life for Beam H-R1-F-5

Figure 4.48 displays the strain over the fatigue life of beam H-R1-F-7. The strain remains constant between 400 and 600 με throughout the fatigue life of the beam.

Upon failure of the beam, the strain spikes to 4000 με at the failed end, whereas the strain drops slightly on the opposite end.

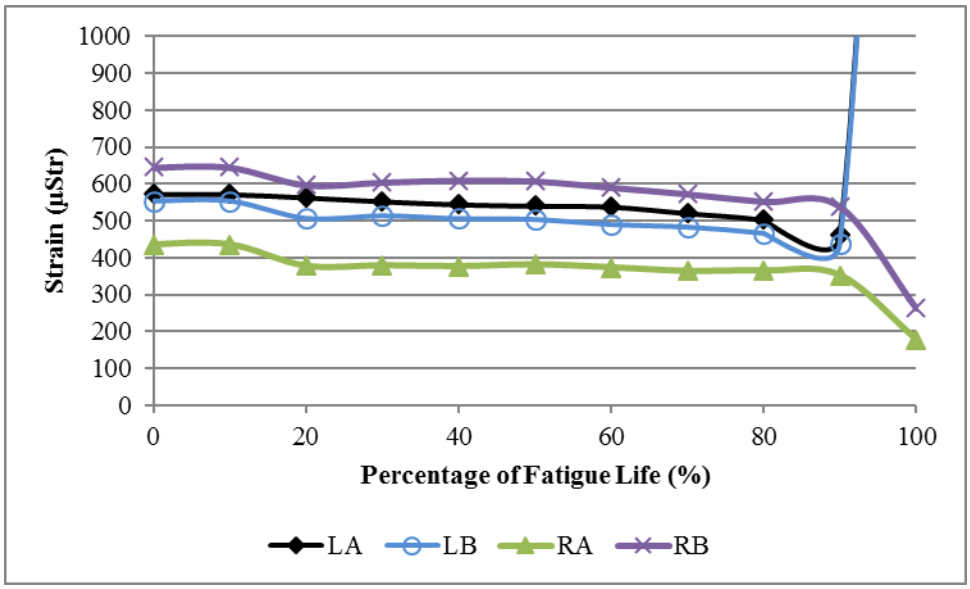

Figure 4.48: Strain vs. fatigue life for Beam H-R1-F-7

Figure 4.49 shows the strain behavior over the fatigue life for beam H-R1-F-8. The strain starts out between 750 and 950 με. Once cracking begins at the left end, the strain in the bars declines indicating a loss of bond. The strain in these bars drops to around 300 με. At failure, the bars on the failed end show an increase in strain up to 500 με. The bars on the opposite end decrease in strain to between 550 and 700 με.

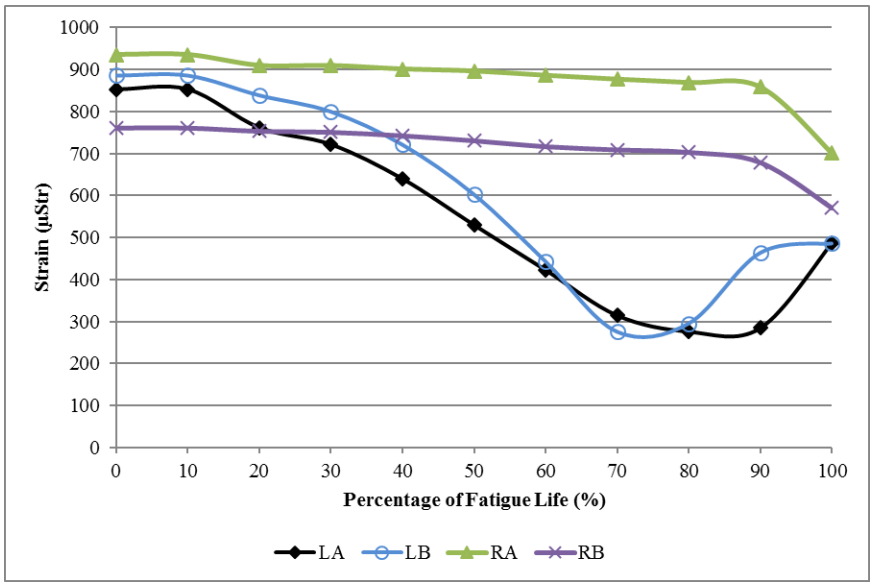

Figure 4.49: Strain vs. fatigue life for Beam H-R1-F-8

Figure 4.50 shows the strain behavior over the fatigue life for beam H-R1-F-9. The strain remains constant throughout the fatigue life up to just before the point of failure. The strain in the bars on the right end was around 600 με and the strain in the bars on left end was around 450 με. Upon failure, the strain on the failed end increased to between 1000 and 1250 με. The strain on the opposite end dropped slightly.

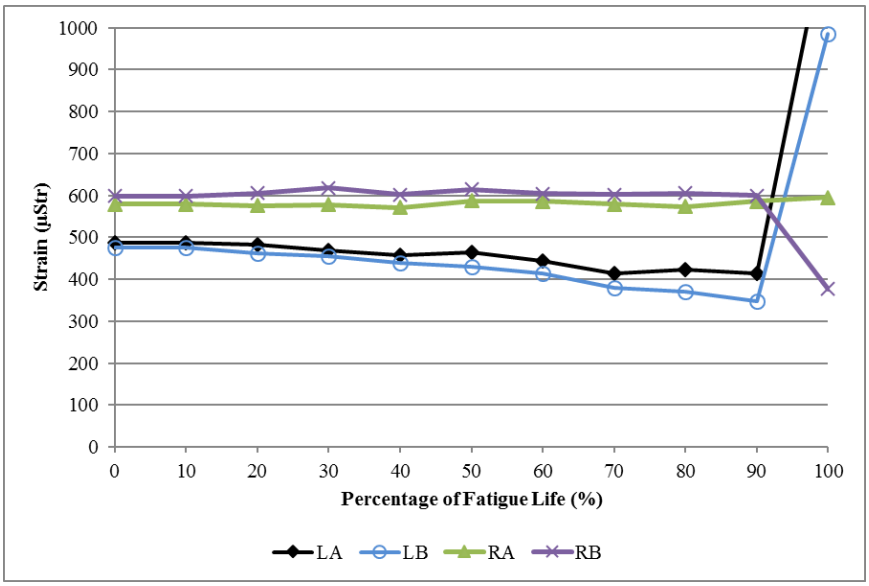

Figure 4.50: Strain vs. fatigue life for Beam H-R1-F-9

Figure 4.51 displays the strain over the fatigue life of beam H-R2-F-1. The strain at side A at the right end remained at 800 με, while the strain at the other locations varied between 450 and 550 με. Upon failure, the strain at all locations dropped to between 200 and 400 με.

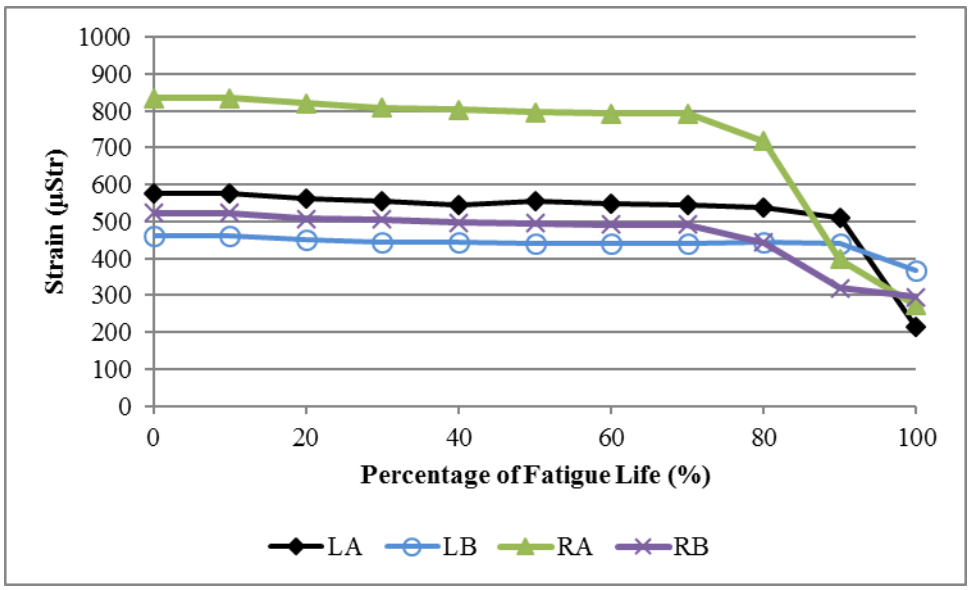

Figure 4.51: Strain vs. fatigue life for Beam H-R2-F-1

Figure 4.52 displays the strain over the fatigue life of beam H-R2-F-2. The strain remained constant between 450 and 600 με throughout the duration of the fatigue life. The strain gauge at side B on the right end had an error in reading, so there are no results at this location.

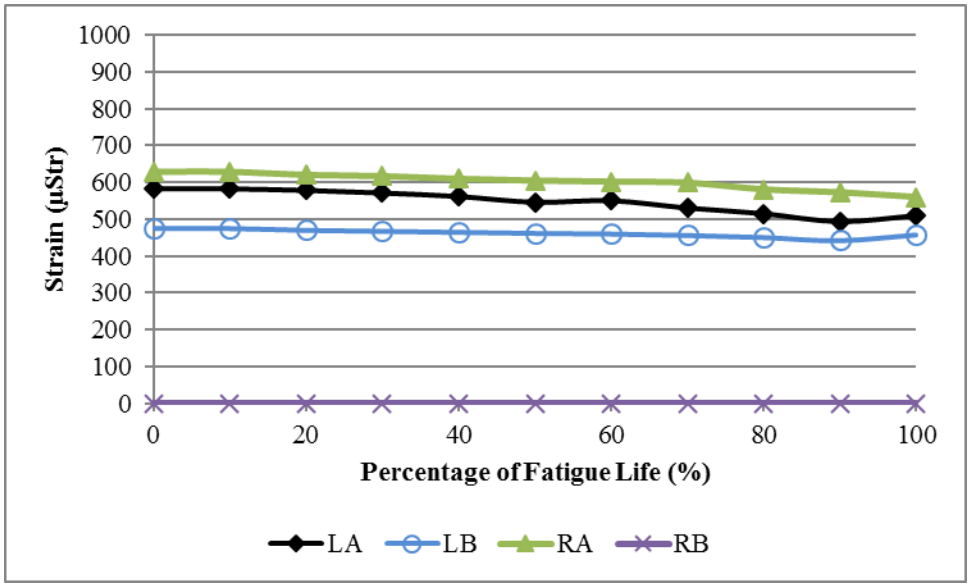

Figure 4.52: Strain vs. fatigue life for Beam H-R2-F-2

Figure 4.53 displays the strain over the fatigue life of beam H-R2-F-3. The strain decreased slightly over the fatigue life up to about 50% of the fatigue life at which point it began to increase again up to the point of failure.

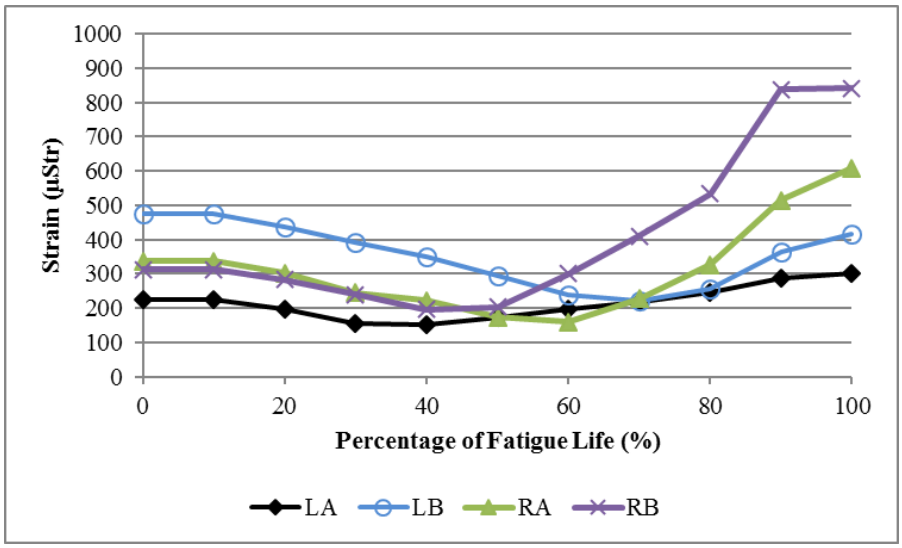

Figure 4.53: Strain vs. fatigue life for Beam H-R2-F-3

Figure 4.54 shows the strain behavior over the fatigue life for beam M-R2-F-1. The strain on the left end starts out between 600 and 700 με, while the strain on the right end starts out around 200 με. The strain gauge on side A on the right end did not read properly. Upon failure, the strain at the failed end dropped to between 200 and 300 με με. The strain at the opposite end dropped slightly as well.

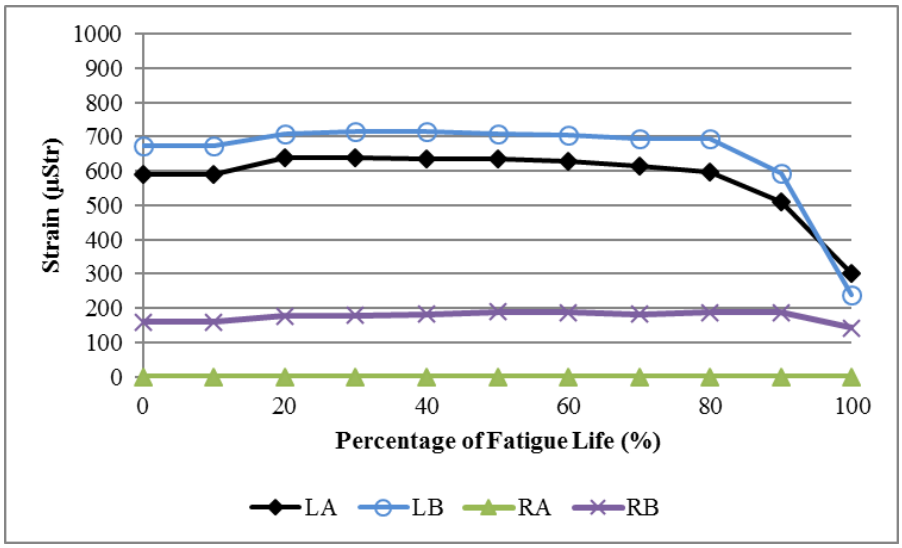

Figure 4.54: Strain vs. fatigue life for Beam H-R2-F-4

Chapter 5 - Conclusions and Recommendations for Future Work

This study included the testing of twenty-nine reinforced concrete beams with varying corrosion levels, repair methods, types of loading, and load ranges. The results from these tests were analyzed and discussed in this thesis to determine the effect of corrosion and repair method on the bond behavior of reinforced concrete beams under both monotonic and repeated loading. The conclusions from this study, along with recommendations for future work, are presented in this chapter.

5.1 Summary of Conclusions

- All of the beams in this study failed by bond, which allows for determining the effect of the variables on the bond behavior.
- Corrosion was found to reduce the static capacity and fatigue life of the beams by deteriorating the bond between the reinforcement and the concrete. This loss of bond was due to cracking caused by expansion forces from the increased volume of the corrosion product along the anchorage length of the reinforcement.
    - The corroded beams had a 21.1% reduction in static capacity and a 25% reduction in fatigue strength.
    - The actual mass loss determined from corrosion evaluation ranged from 14.27% to 25.12%, which is generally classified as high corrosion.
- The addition of the FRCM repair in the anchorage zone was found to improve the bond behavior of the reinforced concrete beams and extend the fatigue lives beyond initial bar slip.

- For the static tests, the repair allowed the beam to maintain the peak load with increasing midspan deflection before experiencing a drop in load thus increasing beam ductility.
    - The uncorroded repaired beam had a 26.9% increase in static capacity compared to the uncorroded unrepaired beam.
    - The corroded repaired beam had a 30.2% increase in static capacity compared to the corroded unrepaired beam.
- For the fatigue tests, the repair allowed the beam to maintain the load range with increasing slip without failure due to spalling of the concrete.
    - The repair increases the fatigue strength by 26.6% for the high corroded beams repaired with material 1, and 20.9% for the high corroded beams repaired with material 2 compared to the fatigue strength of the uncorroded beam.
    - The difference between high corrosion repair 1 and high corrosion repair 2 is roughly 5% indicating that there is not a significant difference in the confinement benefit provided by either grid size.
- The cementitious mortar of the repair allowed for monitoring of cracks beneath the repair prior to failure of the beam.
- The beams repaired with FRCM tended to fail in pullout bond failure. Some tests experienced debonding of repair to the concrete surface, which caused the beam to fail in a splitting bond failure. No rupture of the repair grid was observed.

5.2 Recommendations for Future Work

This study provided information currently lacking in the literature regarding the influence FRCM repair confinement on the bond behavior of reinforced concrete beams. The effects of corrosion and fatigue were addressed as well. However, the bond behavior was found to be influenced by several factors that were not captured by the test matrix in this study including repair mortar thickness, bond of the repair to the concrete substrate, and corrosion crack widths. These variables were not held constant between beams in this study, but impacted the fatigue life under a given loading. These variables require further examination in future studies:

- Various repair mortar thicknesses should be tested to determine the optimal mortar thickness in this application. In this study, the bond of the repair to the concrete substrate was directly related to the thickness of the repair mortar.
- An increased number of specimens at each fatigue level should be tested to improve the accuracy of the results observed with each variable.
- Testing with different bar diameters and beam geometries loaded monotonically and under repeated loading to determine the effect of these variables.
- Testing to compare the effect of FRCM with FRP behavior on bond behavior improvement under monotonic and repeated loading.

Bibliography

Abbas, Safeer. (2007). Analytical study of corroded steel-FRP confined concrete bond under fatigue cyclic loading. Pakistan: University of Engineering and Technology.

Abosrra, L., Ashour, A., & Youseffi. (2011, Oct). Corrosion of steel reinforcement in concrete of different compressive strengths. *Construction and Building Materials*, 25(10), 3915-3925.

Abrams, D. (1913). Tests of Bond between Concrete and Steel. Bulletin 71, Engineering Experiment Station, Universtiy of Illinois, Urbana, IL.

ACI Committee 222. (2001). Protection of metals in concrete against corrosion (ACI 222-01). Farmington Hills, MI: American Concrete Institute.

ACI Committee 408. (2012). Bond and Development of Straight Reinforcing Bars in Tension (ACI 408R-03), reapproved 2012). Farmington Hills, MI: American Concrete Institute.

ACI Committee 408.2. (2012). Report on Bond of Steel Reinforcing Bars Under Cyclic Loads (ACI408.2R-12). Farmington Hills, MI: American Concrete Institute.

ACI Committee 440.2. (2008). Guide to Design and Construction of Externally Bonded FRP Systems for Strengthening Concrete Structures (ACI 440.2R-08). Farmington Hills, MI: American Concrete Institute.

ACI Committee 549.4. (2013). Guide to Design and Construction of Externally Bonded Fabric-Reinforced Cemetitious Matrix (FRCM) Systems for Repair and

Strengthening Concrete and Masonry Structures (ACI549.4R-13). Farmington Hills, MI: American Concrete Institute.

Ahlborn, T. & Denhartigh, T. (2002, Jan). A Comparative Bond Study of Stainless Steel Reinforcement in Concrete. Houghton, MI: Michigan Technological University.

Al-Hammoud, R., Soudki, K., Topper, T. (2010). Bond analysis of corroded reinforced concrete beams under monotonic and fatigue loads. *Cement & Concrete Composites*, 32, 194-203.

Al-Hammoud, R. (2012). Effect of Anchorage Length and Confinement from Stirrups, CFRP, and Supports on the Bond Behavior of Corroded Reinforced Concrete Beams Subjected to Monotonic and Repeated Loading. Waterloo, Ontario, Canada: University of Waterloo.

Al-Hammoud, R., Soudki, K., Topper, T. (2013). Confinement effect on the bond behavior of beams under static and repeated loading. *Construction and Building Materials*, 40, 934-943.

Al-Salloum et al. (2012, Jan/Feb). Experimental and Numerical Study for the Shear Strengthening of Reinforced Concrete Beams Using Textile-Reinforced Mortar. *Journal of Composites for Construction*, 16(1), 74-90.

Al-Sulaimani et al. (1990, Mar/Apr). Influence of corrosion and cracking on bond behavior of reinforced concrete members. *ACI Structural Journal*, 87(2), 220-231.

Almusallam et al. (1996). Effect of reinforcement corrosion on bond strength. *Construction and Building Materials*, 10(2), 123-129.

Amleh, L. & Mirza, S. (1999, May/Jun). Corrosion Influence on Bond between Steel and Concrete. *ACI Structural Journal*, 96, 415-423.

Arboleda, Diana. (2014). Fabric Reinforced Cementitious Matrix (FRCM) Composites for Infrastructure Strengthening and Rehabilitation: Characterization Methods. Open Access Disserations, Paper 1282.

ASTM Standard G1-03 (2011). Standard Practice for Preparing, Cleaning, and Evaluating Corrosion Test Specimens. West Conshohocken, PA, USA.

Auyeung, Y., Balaguru, P., & Chung, L. (2000, Mar/Apr). Bond Behavior of Corroded Reinforcement Bars. *ACI Materials Journal*, 97(28), 214-221.

Balazs, G. (1971, Apr). Cracks formed in concrete around deformed tension bars. *ACI Journal, Proceedings*, 68(4), 244-251.

Bhargava, K et al. (2007). Corrosion-induced bond strength degradation in reinforced concrete - Analytical and empirical models. *Nuclear Engineering and Design*, 237, 1140-1157.

Bhuvaneshwari, P. & SaravanaRajaMohan, K. (2015). Repair of Corroded Reinforced Concrete Beams using Glass Fibre Sheets and Cementitious Composites. *International Journal of ChemTech Research*, 8(2), 579-584.

Bilcik, J. & Holly, I. (2013). Design of concrete structures for durability. London: Taylor & Francis Group.

Bilcik, J. & Holly, I. (2013). Effect of Reinforcement Corrosion on Bond Behaviour. *Procedia Engineering*, 65, 248-253.

Broomfield, J.P. (1997). C*orrosion of Steel in Concrete: Understanding, Investigation and Repair*. London: E & FN Spon.

Cabrera, J. (1996). Deterioration of Concrete Due to Reinforcement Steel Corrosion. *Cement & Concrete Composites*, 18, 47-59.

Cairns, J. (2015). Bond and anchorage of embedded steel reinforcement in fib Model Code 2010. *Structural Concrete*, 16: 45–55.

Cairns, J. et al. (2005, Jul/Aug). Mechanical Properties of Corrosion-Damaged Reinforcement. *ACI Materials Journal*, 102, 256-264.

Castel, A., Francois, R., Arliguie, G. (2000, Nov). Mechanical behavior of corroded reinforced concrete beams - Part 2: Bond and notch effects. *Materials and Structures*, 33, 545-551.

Choi, Y. et al. (2014). Effect of corrosion method of the reinforcing bar on bond characteristics in reinforced concrete specimens. *Construction and Building Materials*. 54, 180-189.

Chung, L. et al. (2004). Correction factor suggestion for ACI development length provisions based on flexural testing of RC slabs with various levels of corroded reinforcing bars. *Engineering Structures*, 26, 1013-1026

Coccia et. al. (2014). Influence of corrosion on the bond strength of steel rebars in concrete. *Materials and Structures.* 49 (1), 537-551.

D'Ambrisi, A., & Focacci, F. (2011). Flexural strengthening of RC beams with cement based composites. *Journal of Composites for Construction*, 15(2), 707-720.

El Maaddawy TA, Soudki KA. (2003). Effectiveness of impressed current technique to simulate corrosion of steel reinforcement in concrete. *Journal of Materials in Civil Engineering*, 15(1), 41-47.

Fang, C. et al. (2004). Corrosion Influence on Bond in Reinforced Concrete. *Cement and Concrete Research*, 34, 2159-2167.

Fang, C. et. al. (2006). Effect of corrosion on bond in reinforced concrete under cyclic loading. *Cement and Concrete Research*, 36, 548-555.

Fardis, M. & Khalili, H. (1981, Nov/Dec). Concrete Encased in Fiberglass-Reinforced Plastic. *ACI Journal*, 78, 440-446.

FIB. (2000). Bond of Reinforcement in Concrete, State of the art report. Switzerland: International Federation for Structural Concrete.

Fu, X. & Chung, D. (1997). Effect of corrosion on the bond between concrete and steel rebar. *Cement and Concrete Research*. 27 (12), 1811-1815.

Gadve, S. et al. (2010, July/Aug). Corrosion Protection of Fibr-Reinforced Polymer-Wrapped Reinforced Concrete. *ACI Materials Journal*, 107(4), 349-356.

Garcia, R., Hajirasouliha, I., & Pilakoutas, K. (2010). Seismic behaviour of deficient RC frames strengthened with CFRP composites. *Engineering Structures*, 32(10), 3075-3085.

Goto, Y. (1971, Apr). Cracks Formed in Concrete Around Deformed Tension Bars. *ACI Journal, Proceedings*, 68, 244-251.

Guneyisi, E., Mermerdas, K., & Gultekin, A. (2015, Oct). Evaluation and modeling of ultimate bond strength of corroded reinforcement in reinforced concrete elements. *Materials and Structures,* 1-21.

Guo, A. et al. (2015). Experimental investigation on the cyclic performance of reinforced concrete piers with chloride-induced corrosion in marine environment. *Engineering Structures,* 105, 1-11.

Hamad, B., Ali, A., & Harajli, M. (2005, Jan/Feb). Effect of Fiber-Reinforced Polymer Confinement on Bond Strength of Reinforcement in Beam Anchorage Specimens. *Journal of Composites for Construction*, 9(1), 44-51.

Hanjari, K., Kettil, P., & Lundgren, K. (2011, Sept/Oct). Analysis of Mechanical Behavior of Corroded Reinforced Concrete Structures. *ACI Structural Journal,* 108(5), 532-541.

Hansson, C., Poursaee, A., & Laurent, A. (2006). Macrocell and microcell corrosion of steel in ordinary Portland cement and high performance concretes. *Cement and Concrete Research*, 36, 2098-2102.

Harajli, M. (2006). Effect of confinement using steel, FRC, or FRP on the bond stress-slip response of steel bars under cyclic loading. *Materials and Structures*, 39, 621-634.

Harajli, M. (2007, May). Cyclic response of concrete members with bond-damaged zones repaired using concrete confinement. *Construction and Building Materials*, 21.5, 937-948.

Higgins, L. et al. (2013). Behaviour of cracked reinforced concrete beams under repeated and sustained load types. *Engineering Structures*, 56, 457-465.

Hunkeler, F. (2005). Corrosion in Reinforced Concrete: Processes and Mechanisms. Switzerland: Technical Research and Consulting on Cement and Concrete.

Jackson, J. (2015). Cost of Corrosion Annually in the US Over $1 Trillion. http://www.g2mtlabs.com/corrosion/cost-of-corrosion/

Joyce, T. (2008). The effects of steel reinforcement corrosion on the flexural capacity and stiffness of reinforced concrete beams. *Ryerson Theses and Dissertations,* Paper 296.

Lee, C. et al. (2000). Accelerated corrosion and repair of reinforced concrete columns using carbon fibre reinforced polymer sheets. *Canadian Journal of Civil Engineering*, 27, 941-948.

Lee, H., Noguchi, T., & Tomosawa, F. (2002). Evaluation of the bond properties between concrete and reinforcement as a function of the degree of reinforcement corrosion. *Cement and Concrete Research*, 32, 1313-1318.

Lin, H., Zhao, Y., & Sun, M. (2014). Effects of Stirrups on Bond Behavior Between Concrete and Corroded Steel Bars. *4th International Conference on the Durability of Concrete Structures*. Purdue University.

Lundgren, K. et al. (2014). Tests on anchorage of naturally corroded reinforcement in concrete. *Materials and Structures*, 48, 2009-2022.

Malvar, L. (1991). Bond of Reinforcement Under Controlled Confinement. Port Hueneme, CA: Office of Naval Research.

Mangat, P. and Elgarf, M. (1999). Bond characteristics of corroding reinforcement in concrete beams. *Materials and Structures*. 32, 89-97.

Masoud, S., Soudki, K., & Topper, T. (2001, Nov.). CFRP-Strengthened and Corroded RC Beams Under Monotonic and Fatigue Loads. *Journal of Composites for Construction*, 5(4), 228-236.

Murcia-Delso, J., Stavridis, A., & Shing, B.(2013, Jul/Aug). Bond Strength and Cyclic Bond Deterioration of Large-Diameter Bars. *ACI Structural Journal*, 110(4), 659-670.

Naus, D. (2007). Primer on Durability of Nuclear Power Plant Reinforced Concrete Structures – A Review of Pertinent Factors. Washington, DC: US-Nuclear Regulatory Commission.

Oh, B. and Kim, S. (2007). Advance crack width analysis of reinforced concrete beams under repeated loads. *Journal of Structural Engineering*, 133(3), 411-419.

Ouglova, A. et. al. (2008). The influence of corrosion on bond properties between concrete and reinforcement in concrete structures. *Materials and Structures*. 41, 969-980.

Ozden, S. & Akpinar, E. (2007, Jul). Effect of confining FRP overlays on bond strength enhancement. *Construction and Building Materials*, 21(7), 1377-1389.

Papakonstantinou, C., Balaguru, P., & Auyeng, Y. (2011, May). Influence of FRP confinement on bond behavior of corroded steel reinforcement. *Cement and Concrete Composites*, 33(5), 611-621.

Pellegrino and Sena-Cruz. (2016). Design Procedures for the Use of Composites in Strengthening of Reinforced Concrete Structures. State of the Art Report of the RILEM Technical Committee 234-DUC. Vol. 19.

Pochanart, S. & Harmon, T. (1989, Sept/Oct). Bond-Slip Model for Generalized Excitations Including Fatigue. *ACI Materials Journal*, 86(5), 465-474.

Rhem, G. & Eligehausen, R. (1979, Feb). Bond of Ribbed Bars Under High Cycle Repeated Loads. *ACI Journal, Symposium Paper*, 76(15), 297-309.

Rteil, A., Soudki, K., & Topper, T. (2007). Preliminary experimental investigation of the fatigue bond behavior of CFRP confined RC beams. *Construction and Building Materials*, 21, 746-755.

Rteil, A., Soudki, K., Topper, T. (2011) Mechanics of bond under repeated loading. *Construction and Building Materials*, 25, 2822-2827.

Sekhar, S. & Raghunath, N. (2013). Static and Cyclic Behaviour of High Performance Corroded Steel Concrete Beams. *International Journal of Engineering and Advanced Technology*, 2(3), 462-466.

Sneed, L. et al. (2013). Fiber Reinforced Cementitous Matrix (FRCM) Composites for Reinforced Concrete Strengthening. Missouri University of Science and Technology.

Soudki, K. (2006). FRP Repair of Corrosion-Damaged Concrete Beams - Waterloo Experience. *Advances in Engineering Structures, Mechanics & Construction*, 165-173.

Soudki, K. (2011). Using fibre reinforced polymer (FRP) composites to extend the service life of corroded concrete structures. University of Waterloo, Canada.

Stanish, K., Hooton, R., & Pantazopoulou, S. (1999, Nov/Dec). Corrosion Effects on Bond Strength in Reinforced Concrete. *ACI Structural Journal*, 96, 915-921.

Tastani, S. & Pantazopoulou, S. (2010, June). Direct Tension Pullout Bond Test: Experimental Results. *Journal of Structural Engineering*, 136(6), 731-743.

Tondolo et al. (2015). Bond behavior with reinforcement corrosion. *Construction and Building Materials*. 93, 926.

Torre-Casanova et al. (2012). Confinement effects on the steel-concrete bond strength and pull-out failure. *Engineering Fracture Mechanics*. 97, 92-104.

Trapko, T. (2013). Stress-strain model for FRCM confined concrete elements. *Composites: Part B*, 45, 1351-1359.

Verna, J. & Stelson, T. (1962, Oct). Failure of Small Reinforced Concrete Beams Under Repeated Loads. *ACI Journal, Proceedings*, 59(10), 1489-1503.

Xiao-dong, D., Xiao-hui, W., & Xin-jian, K. (2013). Bond Behavior of Corroded Reinforcement in Concrete Wrapped with Carbon Fiber Reinforced Polymer Under Cyclic Loading. J.*Shanghai Jiotong Univ. (Sci.),* 18(3), 271-277.

Yalciner, H. et al. (2012). An experimental study on the bond strength between reinforcement bars and concrete as a function of concrete cover, strength and corrosion level. *Cement and Concrete Research.* 42, 643-655.

Yasojima, A. & Kanakubo, T. (2004, Aug). Effect of lateral confinement in bond splitting behavior of RC members. *13th World Conference on Earthquake Engineering*, Paper No. 644.

Yi, W., et al. (2010, Sept/Oct). Fatigue Behavior of Reinforced Concrete Beams with Corroded Steel Reinforcement. *ACI Structural Journal*, 107(5), 526-533.

Zanuy, C., Albajar, L. & Fuente, P. (2010). On the cracking behaviour of the reinforced concrete tension chord under repeated loading. *Materials and Structures*, 43, 611-632.

Appendix A

Diagram of Accelerated Corrosion Wiring

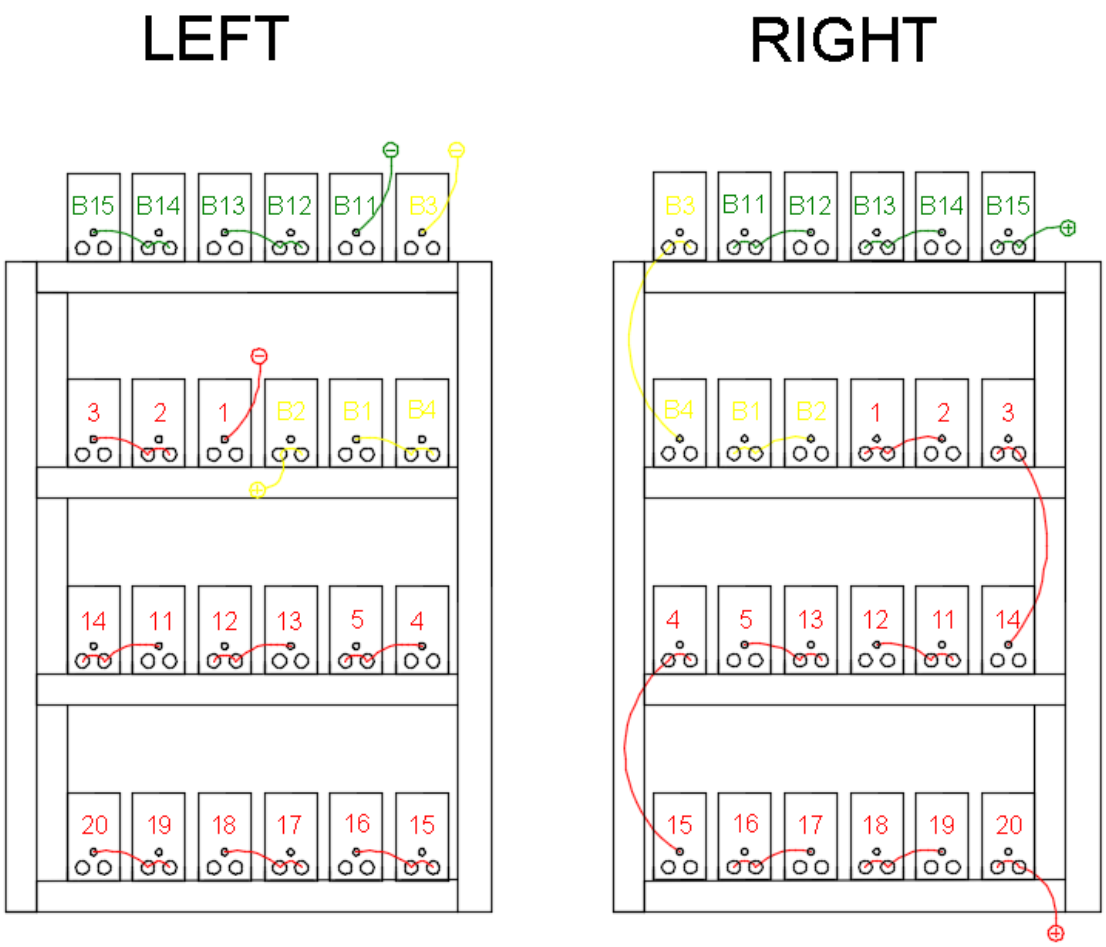

Figure A.1: Diagram of Accelerated Corrosion Wiring

Appendix B

Calculation of the Induced Corrosion Level

The time required to achieve the theoretical mass loss was calculated using Faraday's Law.

- Current Density: i = 967.5 μA/in^2 (150 μA/cm^2)
- Surface Area: $A_s = \pi dL$ x 2 bars = 74.18 in^2

  Where: d = bar diameter = 0.75 in

  L = bonded length = 7.875 in x 2 sides = 15.75 in
- Required Current: $I = i * A_s$
- Faraday's Law: $m = \frac{Ita}{ZF}$

  Where: m = mass loss (g)

  I = corrosion current (A)

  t = corrosion time (s)

  a = atomic weight (56 g for iron)

  Z = valence of the corroding metal (2 for iron)

  F = Faraday's constant (96,500 A.s.)
- Required Time: $t = \frac{mZF}{Ia\,(3600*24)}$
- Mass: $m = \rho AL$

  Where: ρ = density (0.282 lb/in^3 (7.8 g/cm^3 for steel))

  A = cross-sectional area (0.44 in^2)

  L = length (7.875 in)
- The mass multiplied by the desired percent mass loss was used in the time equation.

Mass Loss (%)	t (days)
5	50
15	148

Appendix C

Experimental Mass Loss Analysis

Mass loss analysis was performed on the corroded bars in order to determine actual mass loss compared to the theoretical mass loss predicted using Faraday's Law. The chemical cleaning procedure performed for the analysis was based on ASTM G1-03 (2011).

Items required:

- Chemical fume hood
- 1 liter beaker
- Acid resistant basin
- Tongs
- Bristle (nonmetallic brush)
- Stirring plate
- Dryer
- Scale
- Proper disposal of acid solution
- Face protection
- Gloves

Chemical reagents used:

- Distilled water
- Concentrate hydrochloric acid (HCL)
- Hexamethylenetetramine

Procedure

1. Cut the bar to a length that captures the length exposed to corrosion.
2. Remove concrete from surface of bar by scrubbing with a bristle brush.
3. Measure and record the length and the weight of the steel bar after it is cut and cleaned.
4. Place the steel bars into an acid resistant basin.
5. Place a 1 liter beaker on a stirring plate in a fume hood.
6. Pour 500 mL of distilled water into the beaker followed by 500 mL of HCL.
7. Stir the solution for one minute.
8. Add 3.5 g of hexamethylenetetramine to the solution and stir for an additional minute or until the buffer is completely dissolved.
9. Carefully pour the solution into the acid resistant basin.
10. If bars are not fully submerged, repeat steps 5 to 8 until they are fully submerged.
11. Allow the bars to remain in the acid bath for a minimum of 10 minutes or until the reaction is completed. Bars with high levels of corrosion may require longer times.
12. Clean the bars with the bristle brush.
13. Allow bars to fully dry. The use of an electric dryer can expedite this process.
14. Measure and record the weight of the steel bar after the completed cleaning cycle.
15. Repeat the procedure until the weight of the steel bars becomes constant.

Mass Loss Calculation

In order to determine correct the corrosion mass loss for the loss of the cleaning procedure, a control bar must be utilized. The same procedure used on the corroded bars should be used for an uncorroded bar. Based on the mass and volume from the cleaned control bar, a control density can be determined.

Appendix D

Static Test Individual Beam Details

Beam N-U-S

Beam N-U-S, uncorroded and unrepaired, was tested monotonically to failure. A vertical crack formed at midspan (Figure D.1 and Figure D.2) of the beam at 5.52 kips and 0.04 in. midspan deflection causing the first drop in load to 4.25 kips and 0.06 in. The load continued to increase until reaching its peak at 16.4 kips with a midspan deflection of 0.23 in. The second drop occurred at this time due to shear cracking forming in both sides of the right support. The load dropped to 10.9 kips with midspan deflection of 0.24 in. With further load increase, the bond of the reinforcement to the concrete was lowered near the shear crack resulting in a combination of shear and bond failure (Figure D.3, Figure D.4, and Figure D.5). There was some concrete crushing at the top of the beam at the right support. The load reached 60% of the peak load and the test stopped. The load was 9.71 kips and the midspan deflection was 0.745 in at the end of the test.

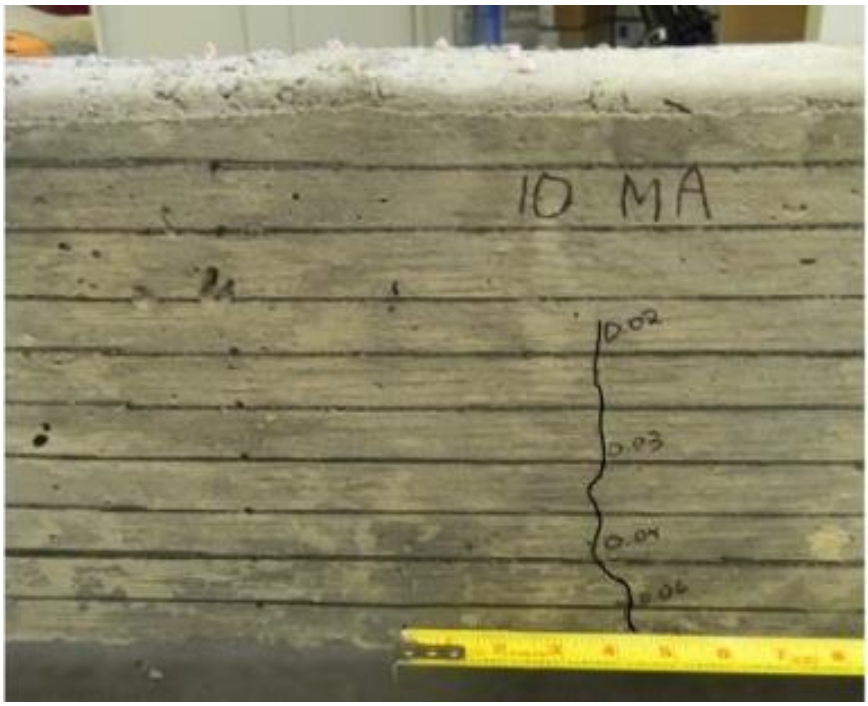

Figure D.1: Flexural crack at midspan of Beam N-U-S (Side A)

Figure D.2: Flexural crack at midspan of Beam N-U-S (Side B)

Figure D.3: Shear/splitting bond failure at right support of Beam N-U-S (Side A)

Figure D.4: Shear/splitting bond failure at right support of Beam N-U-S (Side B)

Figure D.5: Failure at right support of Beam N-U-S

Beam H-U-S-1

Beam H-U-S-1, mild corroded and unrepaired, was tested monotonically to failure. A flexural crack formed to the right of midspan (Figure D.6 and Figure D.7) at roughly 4.5 kips and midspan deflection of 0.03 in. Shear cracks formed on both sides of the beam at the left support around 9 kips. The load peaked at 10.1 kips and midspan deflection of 0.17 in. The shear cracks continued to grow until the bars slipped significantly, hitting the limit and preventing the test from reaching 60% of the peak load. The midspan deflection was 0.729 in. at the end of the test. The beam failed in a combination shear and splitting bond failure (Figure D.8 and Figure D.9).

Figure D.6: Flexural crack at mid-span of Beam H-U-S-1 (Side A)

Figure D.7: Flexural crack at midspan of Beam H-U-S-1 (Side B)

Figure D.8: Shear/splitting bond failure at right support of Beam H-U-S-1 (Side A)

Figure D.9: Shear/splitting bond failure at right support of Beam H-U-S-1 (Side B)

Beam H-U-S-2

Beam H-U-S-2, high corroded and unrepaired, was tested monotonically to failure. A shear crack formed in side B at the right support (Figure D.13) at around 4 kips and 0.015 in. midspan deflection. A flexural crack formed to the right of midspan (Figure D.10 and Figure D.11) at around 6.5 kips and 0.1 in. midspan deflection. The shear crack continued to grow in side B of the right support. The load peaked at 13.54 kips and midspan deflection of 0.25 in. At this time, a shear crack became visible on side A of the right support (Figure D.12), as well as both sides of the left support (Figure D.14 and Figure D.15). The shear crack at the left support ended up growing larger than the right support. The test was stopped when the load reached 60% of the peak load. The midspan deflection was 0.665 in. at the end of the test.

Figure D.10: Flexural crack at mid-span of Beam H-U-S-2 (Side A)

Figure D.11: Flexural crack at midspan of Beam H-U-S-2 (Side B)

Figure D.12: Shear crack at right support of Beam H-U-S-2 (Side A)

Figure D.13: Shear crack at right support of Beam H-U-S-2 (Side B)

Figure D.14: Shear/splitting bond failure at left support of Beam H-U-S-2 (Side A)

Figure D.15: Shear/splitting bond failure at left support of Beam H-U-S-2 (Side B)

Beam N-R1-S

Beam N-R1-S, high corroded and unrepaired, was tested monotonically to failure. A flexural crack formed to the left of midspan (Figure D.16) at around 5.5 kips. The first drop in the load at 20 kips and 0.2 in midspan deflection was from the bars on the left end slipping slightly. Shortly after the first drop, a crack formed in the cementitious mortar of the repair at the right support causing another drop in load. This indicates cracking of the beam beneath the repair that are propagating through the mortar. After the second drop, the load continued to increase up to the peak load of 22.44 kips. At this time, the fibers in the right repair snapped causing another drop (Figure D.17 and Figure D.19). For the remainder of the test, the bars at the right end continued to slip until the load reached 60% of the peak load. The midspan deflection was 0.656 in. at the end of the test. Figure D.18 and Figure D.20 show the right support with the repair removed.

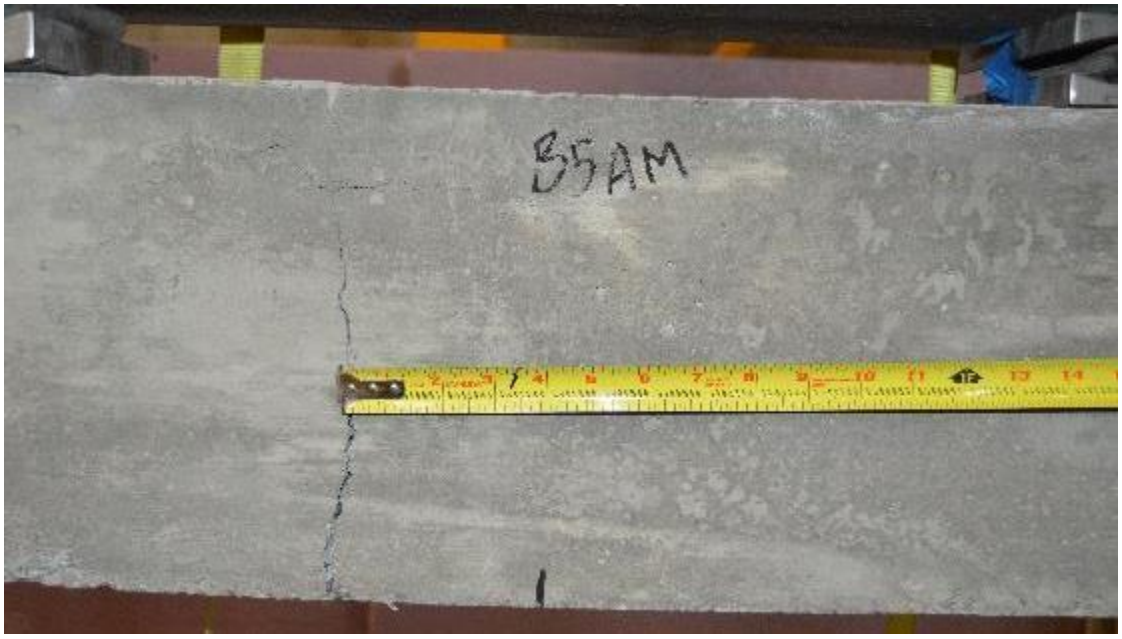

Figure D.16: Flexural crack at mid-span of Beam N-R1-S (Side A)

Figure D.17: Shear/pullout bond failure at right support of Beam N-R1-S (Side A)

Figure D.18: Repair removed at right support of Beam N-R1-S (Side A)

Figure D.19: Shear/pullout bond failure at right support of Beam N-R1-S (Side B)

Figure D.20: Repair removed at right support of Beam N-R1-S (Side A)

Beam H-R1-S

Beam H-R1-S, high corroded and repaired, was tested monotonically to failure. A flexural crack formed to the left of midspan (Figure D.21) at around 6.5 kips. At roughly 19.2 kips and 0.05 in. midspan deflection, cracks began to form in the repair at the left support (Figure D.22 and Figure D.23). The load peaked at 19.4 kips. After the peak, the bar at the left end began slipping and kept slipping until the end of the test. Towards the end of the test a second flexural crack formed below the right loading point. The test ended when the load reached 60% of the peak load. The midspan deflection was 0.507 in. at the end of the test.

Figure D.21: Flexural crack at mid-span of Beam H-R1-S (Side A)

Figure D.22: Shear/splitting bond failure at left support of Beam H-R1-S (Side A)

Figure D.23: Shear/splitting bond failure at left support of Beam H-R1-S (Side B)

Beam N-U-F-1

Beam N-U-F-1 was fatigued using a load range of 11.69 kips, which was 71% of the static capacity. This beam failed at 1078 cycles. A flexural crack formed to the right of midspan at the start of the test, which grew throughout the duration of the test. A shear crack near the right support caused the failure of the beam (Figure D.24 and Figure D.25). As the crack grew, the bars pulled through the concrete and the concrete cover below the reinforcement detached. The crack grew to the compression zone of the beam and resulted in concrete crushing of the concrete. No damage occurred near the left support.

Figure D.24: Failure at right support of Beam N-U-F-1 (Side A)

Figure D.25: Failure at right support of Beam N-U-F-1 (Side B)

Appendix E

Uncorroded Unrepaired Fatigue Test Individual Beam Details

Beam N-U-F-2

Beam N-U-F-2 was fatigued using a load range of 10.86 kips, which was 66% of the static capacity. This beam failed at 29,931 cycles. At the start of the test, a flexural crack formed to the right of midspan. A shear crack near the left support caused the beam to fail (Figure E.1 and Figure E.2). The concrete lugs were still intact, which indicates a splitting bond failure (Figure E.3). The concrete cover remained intact after failure, but the crack size prevented the development of a sufficient bond between the reinforcement and the concrete. No damage occurred near the right support.

Figure E.1: Failure at left support of Beam N-U-F-2 (Side A)

Figure E.2: Failure at left support of Beam N-U-F-2 (Side B)

Figure E.3: Beam N-U-F-2 concrete keys. Top is Side B and bottom is Side A.

Beam N-U-F-3

Beam N-U-F-3 was fatigued using a load range of 10.69 kips, which was 65% of the static capacity. This beam failed at 227,123 cycles. At the start of the test, a flexural crack formed at the left of midspan. A second flexural crack formed below the right loading point during the test. The crack at midspan continued to grow throughout the test, but the crack below the right loading point grew insignificantly. Towards the end of the test a third flexural crack formed on side B near the first midspan crack. A combination shear/bond failure occurred near the left support (Figure E.4 and Figure E.5). As the shear crack, grew to the top of the beam, the concrete cover below the bars detached caused a loss of bond. Figure E.6 shows the concrete after the reinforcement is removed. On side B, there was some crushing of the concrete keys. The rest of the area was destroyed in the failure.

Figure E.4: Failure at left support of Beam N-U-F-3 (Side A)

Figure E.5: Failure at left support of Beam N-U-F-3 (Side B)

Figure E.6: Beam N-U-F-3 concrete keys. Top is Side B and bottom is Side A.

Beam N-U-F-4

Beam N-U-F-4 was fatigued using a load range of 10.52 kips, which was 64% of the static capacity. This beam failed at 460,564 cycles. At the start of the test, a flexural crack formed to the left of midspan. During the test, a second flexural crack formed below the right loading point. Both cracks grew throughout the duration of the test. Several shear cracks formed on side B at the right support (Figure E.7). The cracks caused a loss of bond of the bar on this side and failure of the beam at this end.

Figure E.7: Shear/bond failure at right support of Beam N-U-F-4 (Side B)

Side A had a vertical crack originating from the corner of the pocket; however, the bar on this side did not slip as significantly as the bar on side B (Figure E.8).

Figure E.8: Crack at right support of Beam N-U-F-4 (Side A)

The concrete interface above the bars showed that the bar on side B sheared off the concrete lugs, whereas the bar on side A did not cause damage to the concrete lugs (Figure E.9).

Figure E.9: Beam N-U-F-4 concrete keys. Top is Side A and bottom is Side B.

Appendix F

Corroded Unrepaired Fatigue Test Individual Beam Details

Beam H-U-F-1

Beam H-U-F-1 reached one million cycles when fatigued using load ranges of 6.01 kip (44% of static capacity), 6.21 kip (38% of static capacity), 6.61 kip (40% of static capacity), and 7.12 kip (43% of static capacity). The beam failed prematurely due to a power outage when tested at 7.72 kip (47% of static capacity). A flexural crack formed at the right of midspan at the start of the test. A second fatigue crack formed below the left loading point. This beam reached the maximum fatigue life of one million cycles four times. During the 5th test, the power went out at around 340,000 cycles, which caused a large force to be applied to the beam resulting in failure. This failure included a combination shear/bond failure at the right support. There was concrete crushing of the compression zone above the right notch.

Figure F.1: Failure at right support of Beam H-U-F-1 (Side A)

Figure F.2: Failure at right support of Beam H-U-F-1 (Side B)

Beam H-U-F-2

Beam H-U-F-2 was fatigued using a load range of 8.43 kips, which was 51% of the static capacity. The beam failed due to a power outage, so the results were inconclusive. A flexural crack formed at the right of center at the start of the test. A second fatigue crack formed below the left loading point. The power went out some time into the test causing a large force to be applied to the beam, which resulted in failure. This failure included a flexure failure at midspan and a combination shear/bond failure at the right support. At midspan there was concrete crushing of the compression zone. A similar crushing occurred above the right notch. At the right support, there was a loss of concrete cover below the bars and a sharp shear crack towards the center. No damage occurred near the left support.

Figure F.3: Failure at right support of Beam H-U-F-2 (Side A)

Figure F.4: Failure at right support of Beam H-U-F-2 (Side B)

Beam H-U-F-3

Beam H-U-F-3 reached one million cycles when fatigued using a load range of 8.43 kip (51% of static capacity). The beam failed prematurely due to a controller accident when tested at 8.98 kip (55% of static capacity). A flexural crack formed at the right of center at the start of the test. During the second test, the controller was accidently turned off which caused a large force to be applied to the beam, which in turn caused the beam to fail. This occurred at around 520,000 cycles. The loss of concrete cover below the bars occurred at the right of the beam.

Figure F.5: Failure at right support of Beam H-U-F-3 (Side A)

Figure F.6: Failure at right support of Beam H-U-F-3 (Side B)

Beam H-U-F-4

Beam H-U-F-4 reached one million cycles when fatigued using load ranges of 7.58 kip (59% of static capacity) and 7.68 kip (60% of static capacity). When the beam was fatigued using a load range of 10.65 kips, which was 89% of the static capacity, the beam failed at 539,753 cycles. A flexural crack at the right of center formed at the start of the test first test. Shortly before failure, a second flexural crack occurred below the left loading point. A shear crack began to propagate from the left support towards the center of the beam. As this crack grew, the concrete cover spalled off, which caused a loss of bond and ultimately the failure of the beam (Figure F.7 and Figure F.8). The right end of the beam did see some additional cracking, but the slip of the bars on that end did not slip. Due to the excessive spalling during failure, the concrete keys below the bars at the left support were difficult to inspect for bond failure (Figure F.9).

Figure F.7: Failure at left support of Beam H-U-F-4 (Side A)

Figure F.8: Failure at left support of Beam H-U-F-4 (Side B)

Figure F.9: Beam H-U-F-4 concrete keys. Top is Side B and bottom is Side A.

Beam H-U-F-5

Beam H-U-F-5 was fatigued using a load range of 8.84 kips, which was 88% of the static capacity. The beam failed at 65 cycles. A flexural crack formed at the right of midspan at the start of the test. The bond of the reinforcement was lost at the left end of the beam shortly after the test began resulting in a failure. The concrete cover beneath the bars was pushed off by growing cracks near the support. No failure occurred at the right end of the beam.

Figure F.10: Failure at left support of Beam H-U-F-5 (Side A)

Figure F.11: Failure at left support of Beam H-U-F-5 (Side B)

Figure F.12: Beam H-U-F-5 concrete keys. Top is Side A and bottom is Side B.

Beam H-U-F-6

Beam H-U-F-6 was fatigued using a load range of 8.41 kips, which was 83% of the static capacity. The beam failed at 88 cycles. A flexural crack formed at the right of center at the start of the test. A crack propagated from the corner of the left pocket at a sharp angle towards the center of the beam. At the same time, the crack from the corrosion at this end increased in width until the bottom cover fell off. This loss of bond caused the bars at this end to slip and fail the beam with a splitting bond failure.

Figure F.13: Failure at left support of Beam H-U-F-6 (Side A)

Figure F.14: Failure at left support of Beam H-U-F-6 (Side B)

Figure F.15: Beam H-U-F-6 concrete keys. Top is Side A and bottom is Side B.

Beam H-U-F-7

Beam H-U-F-7 was fatigued using a load range of 5.6 kips, which was 55% of the static capacity. The beam failed due to a power outage, so the results were inconclusive. A flexural crack formed at the left of center at the start of the test. The power went out at around 280,000 cycles caused a large force to be applied to the beam, which resulted in

failure. This failure included a flexure failure at midspan and a combination shear/bond failure at the right support. At midspan there was concrete crushing of the compression zone. At the right support there was a loss of concrete cover below the bars and a sharp shear crack towards the center (Figure F**.16** and Figure F**.17**).

Figure F.16: Failure at right support of Beam H-U-F-7 (Side A)

Figure F.17: Failure at right support of Beam H-U-F-7 (Side B)

Appendix G

Corroded Repaired Fatigue Test Individual Beam Details

Beam H-R1-F-1

Beam H-R1-F-1 was fatigued using a load range of 12.83 kips. The beam failed at 3695 cycles. At the start of the test, a flexural crack formed at the right of midspan. During the test, a second crack developed beneath the left loading point. This crack was more diagonal indicating that it was likely due to shear instead of flexure. Near the left support, cracks occurred beneath the repair, which showed through the repair. The repair effectively held the concrete cover below the bars forcing a pullout bond failure to occur instead of a splitting bond failure. After removal of the bars, it was found that the concrete lugs were sheared off, which confirms the pullout bond failure (Figure G.3). The repair near the right support showed some cracking, but no indication of failure.

Figure G.1: Failure at left support of Beam H-R1-F-1 (Side A)

Figure G.2: Failure at left support of Beam H-R1-F-1 (Side B)

Figure G.3: Beam H-R1-F-1 concrete keys. Top is Side B and bottom is Side A.

Beam H-R1-F-2

Beam H-R1-F-2 was fatigued using a load range of 12.33 kips and failed at 894 cycles. At the start of the test, a flexural crack formed to the right of midspan. A shear crack originating at the corner of the pocket near the left support formed during the test. The cracks did not show through the mortar. Towards the end of the test the repair lost bond with the surface and popped off. Without the confining pressure of the repair, the bars slipped and failed the beam. At the time of failure, the flexural crack near midspan caused some concrete crushing of the compression zone.

Figure G.4: Failure at right support of Beam H-R1-F-2 (Side A)

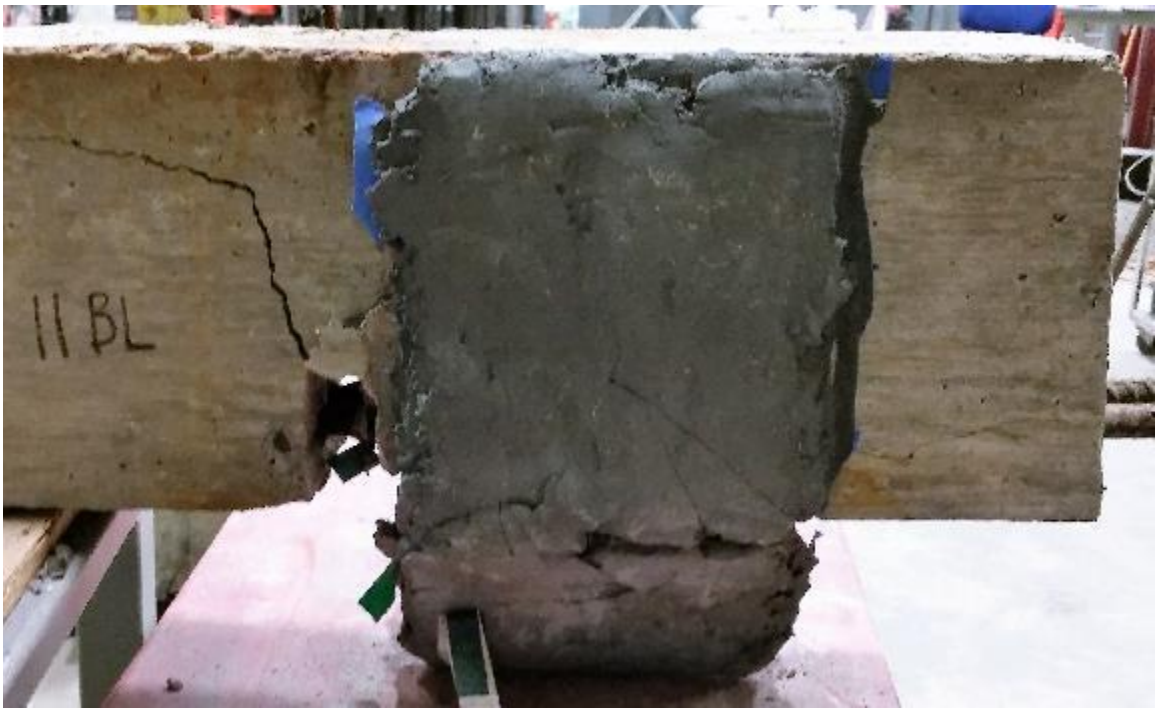

Figure G.5: Failure at right support of Beam H-R1-F-2 (Side B)

Figure G.6: Beam H-R1-F-2 concrete keys. Top is Side A and bottom is Side B.

Beam H-R1-F-3

Beam H-R1-F-3 was fatigued using a load range of 12.33 kips. The beam failed at 149,407 cycles. At the start of the test, a flexural crack formed at the left of midspan. During the test, a second flexural crack developed beneath the right loading point. The failure occurred at the left support. The repair was pushed away from the beam on both sides from the force of the shear crack. The bond of the repair to the concrete surface failed, which allowed the concrete cover to be released at the bottom of the beam. This caused the bond between the reinforcement and the concrete to suffer and lead to bar slip. The data shows that the initial slip of the bars at the left end occurred at 40% of the fatigue life. The repair allowed the beam to continue to be loaded after initial bar slip.

Figure G.7: Failure at right support of Beam H-R1-F-3 (Side A)

Figure G.8: Failure at right support of Beam H-R1-F-3 (Side B)

Beam H-R1-F-4

Beam H-R1-F-4 was fatigued using a load range of 11.83 kips and failed at 55,109 cycles. At the start of the test, a flexural crack formed to the right of midspan. During the test several shear cracks formed at the right support and showed through the repair. The repair remained bonded to the concrete surface throughout the test. The confinement applied from the repair forced the beam to exhibit a pullout bond failure at the right support. The bar slip at the right end increased slowly throughout the test and increased sharply at failure. No failure occurred at the left support.

Figure G.9: Failure at right support of Beam H-R1-F-4 (Side A)

Figure G.10: Failure at right support of Beam H-R1-F-4 (Side B)

Figure G.11: Failure at right support of Beam H-R1-F-4 (Side C)

Figure G.12: Beam H-R1-F-4 concrete keys. Top is Side A and bottom is Side B.

Beam H-R1-F-5

Beam H-R1-F-5 reached one million cycles when fatigued using load ranges of 11.33 kip and 11.58 kip. When the load range was increased to 11.73 kips, the beam failed at 244,982 cycles. At the start of the test, a flexural crack formed to the right of midspan. Cracks in the right support repair formed around 160,000 cycles. As the test continued,

the cracks grew and the repair slowly lost bond with the concrete surface. It eventually detached from the beam, which caused the loss of reinforcement bond and failure of the beam. No failure occurred at the left support.

Figure G.13: Failure at right support of Beam H-R1-F-5 (Side A)

Figure G.14: Failure at right support of Beam H-R1-F-5 (Side B)

Figure G.15: Failure at right support of Beam H-R1-F-5 (Side C)

Figure G.16: Beam H-R1-F-5 concrete keys. Top is Side A and bottom is Side B.

Beam H-R1-F-6

Beam H-R1-F-6 was fatigued using a load range of 11.58 kips and beam failed at 29,223 cycles. At the start of the test, a flexural crack formed to the left of midspan. During the test, shear cracks began to form near both supports that propagated through the repair. As the cracks grew, the repair was effective in holding the concrete cover and extending the life of the beam. The bond of the repair to the concrete remained intact throughout the duration of the test. A pullout bond failure at the left support caused the beam to fail. A small level of bar slip occurred near the right support, but the bar slip at the left support was more significant. There was an issue with the data recording during this test, so there are no data results.

Figure G.17: Failure at left support of Beam H-R1-F-6 (Side A)

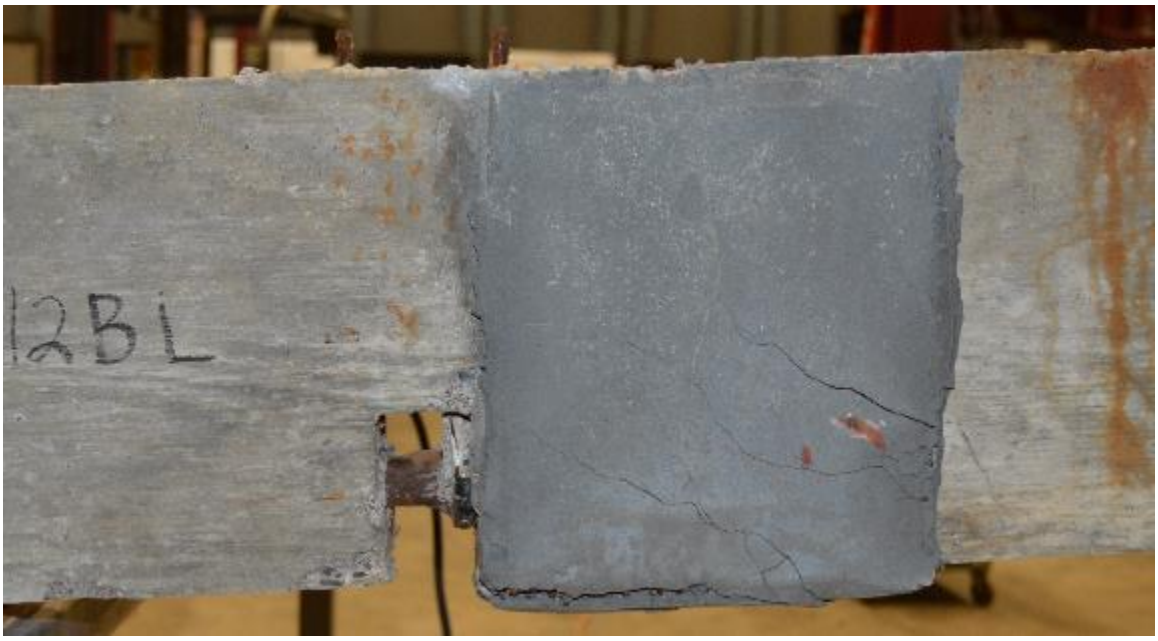

Figure G.18: Failure at left support of Beam H-R1-F-6 (Side B)

Figure G.19: Failure at left support of Beam H-R1-F-6 (Side C)

Figure G.20: Beam H-R1-F-6 concrete keys. Top is Side A and bottom is Side B.

Beam H-R1-F-7

Beam H-R1-F-7 was fatigued using a load range of 11.58 kips and failed at 613 cycles. At the start of the test, a flexural crack formed to the left of midspan, which grew throughout the duration of the test. Throughout the test the bond of the repair to the beam on side A at the left support was decreasing until it eventually detached from the surface. There were longitudinal cracks beneath the repair on side A at the left support; however, these cracks did not show through the repair. On side B at the left support, there was a shear crack that showed through the repair and another shear crack originating from the notch. The repair remained fully bonded to the beam surface on side B at the left support. No damage occurred at the right support at failure. There was concrete crushing in the compression zone at midspan.

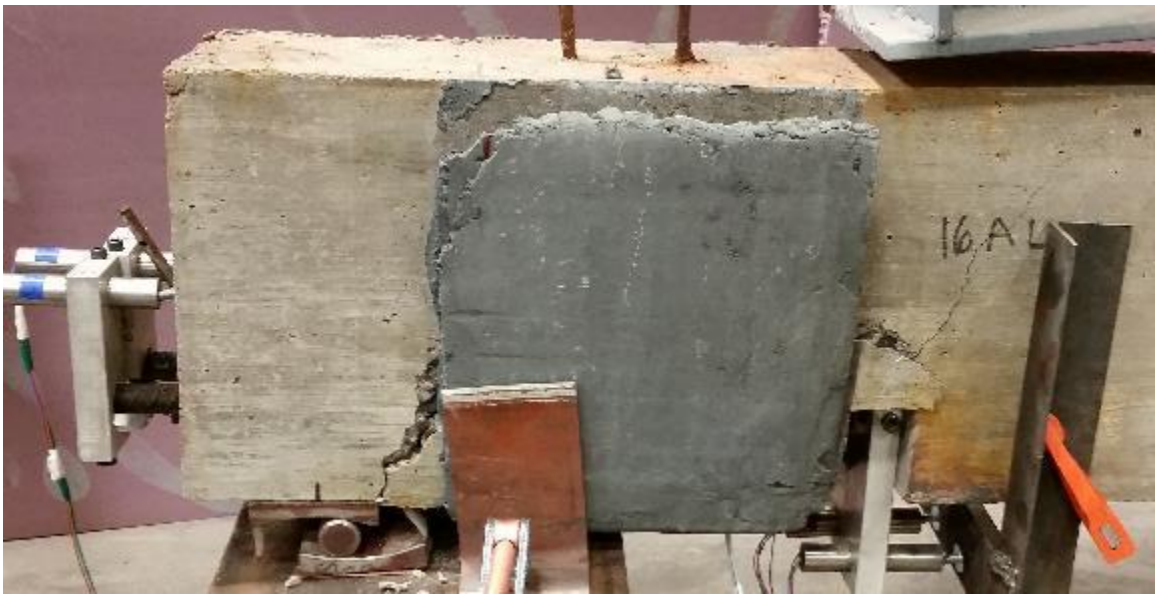

Figure G.21: Failure at left support of Beam H-R1-F-7 (Side A)

Figure G.22: Failure at left support of Beam H-R1-F-7 (Side B)

Figure G.23: Beam H-R1-F-7 concrete keys. Top is Side A and bottom is Side B.

Beam H-R1-F-8

Beam M-R1-F-1 was fatigued using a load range of 12.58 kips. The beam failed at 4198 cycles. At the start of the test, a flexural crack formed at the left of midspan. During the test a second flexural crack developed beneath the right loading point. Around 600 cycles, the left support showed cracks alongside the repair, but the repair continued to hold the cover from releasing. The initial bar slip occurred at about 10% of the fatigue life, but the repair effectively confined the cover below the bars, increasing the life of the beam. The repair slid vertically as the beam was being fatigued, until the bond eventually was broken and the repair popped off of the surface of the beam.

Figure G.24: Failure at left support of Beam H-R1-F-8 (Side A)

Figure G.25: Failure at left support of Beam H-R1-F-8 (Side B)

Figure G.26: Failure at left support of Beam H-R1-F-8 with repair removed (Side A)

Figure G.27: Beam M-R1-F-1 concrete keys. Top is Side B and bottom is Side A.

Beam H-R1-F-9

Beam H-R1-F-9 reached one million cycles when fatigued using a load range of 11.33 kips. The load range was increased to 12.33 kips for a second test. Under this load range, the beam failed at 3695 cycles. At the start of the test, a flexural crack formed at the left of midspan. Shear cracks formed across the repair at the left support. The bond between the repair and the concrete surface was lowered throughout the test, but full release did not occur. The confining pressure provided by the repair caused a pullout bond failure, which was confirmed by inspection of the crushed concrete lugs below the bars. The longitudinal crack from the corrosion expansion propagated through the repair near the right support, but no failure occurred at this end.

Figure G.28: Failure at left support of Beam H-R1-F-9 (Side A)

Figure G.29: Failure at left support of Beam H-R1-F-9 (Side B)

Figure G.30: Beam H-R1-F-9 concrete keys. Top is Side B and bottom is Side A.

Beam H-R2-F-1

Beam H-R2-F-1 was fatigued using a load range of 11.33 kips and failed at 1,915 cycles. At the start of the test, a flexural crack formed at the right of midspan. The bond of the repair to the beam at the right support decreased throughout the duration of the test. Side A fully debonded and side B slightly debonded from the surface of the beam. A shear crack had formed beneath the repair on side B, but did not show through the repair. The bars started to slip at the right end at 20% of the fatigue life and continued to slip until the failure of the beam. No failure occurred at the left support.

Figure G.31: Failure at left support of Beam H-R2-F-1 (Side A)

Figure G.32: Failure at left support of Beam H-R2-F-1 (Side B)

Figure G.33: Failure of Beam H-R2-F-1 with repair removed (Side B)

Figure G.34: Beam H-R2-F-1 concrete keys. Top is Side B and bottom is Side A.

Beam H-R2-F-2

Beam H-R2-F-2 was fatigued using a load range of 11.08 kips and failed at 38,506 cycles. At the start of the test, a flexural crack formed at the left of midspan. A shear crack formed in the repair at the left support. The repair remained bonded to the beam throughout the duration of the test, but the bars slipped at a constant rate as the crack grew. As the crack widened, the fabric became exposed, but there was no visible damage to the fibers. The concrete lugs below the bars were sheared, which indicates a pullout bond failure. The confinement of the repair switched the failure mode from splitting to pullout. No failure occurred at the right support.

Figure G.35: Failure at left support of Beam H-R2-F-2 (Side A)

Figure G.36: Repair removed at left support of Beam H-R2-F-2 (Side A)

Figure G.37: Failure at left support of Beam H-R2-F-2 (Side B)

Figure G.38: Beam H-R2-F-2 concrete keys. Top is Side A and bottom is Side B.

Beam H-R2-F-3

Beam H-R2-F-3 was fatigued using a load range of 10.58 kips and failed at 39,023 cycles. At the start of the test, a flexural crack formed to the left of midspan, which grew in width throughout the test. Several shear cracks began to form in the repair around 5000 cycles. The repair effectively confined the concrete cover below the bars to extend the life of the beam. The bar slip initiated around 70% of the fatigue life and increased up to failure. The repair caused the beam to fail in a pullout bond failure. Inspection of the concrete below the bars indicates that a pullout failure did occur. No failure occurred at the left support.

Figure G.39: Failure at right support of Beam H-R2-F-3 (Side A)

Figure G.40: Failure at right support of Beam H-R2-F-3 (Side B)

Figure G.41: Repair removed at left support of Beam H-R2-F-3 (Side B)

Figure G.42: Failure at right support of Beam H-R2-F-3 (Side C)

Figure G.43: Beam H-R2-F-3 concrete keys. Top is Side B and bottom is Side A.

Beam H-R2-F-4

Beam H-R2-F-4 was fatigued using a load range of 11.58 kips and failed at 42,081 cycles. At the start of the test, a flexural crack formed to the right of midspan. A second flexural crack formed around 13,000 cycles. A shear crack formed at the left support and propagated through the mortar (Figure G.44 and Figure G.46). As the crack grew, the fabric became exposed. It withheld the load, but started to fray towards the end of the test. As the shear crack in the concrete grew, the bond of the reinforcement to the concrete was decreased, which eventually resulted in a splitting bond failure. This failure caused a sharp slip of the bar at the end of the test. No failure occurred at the right support. Figure G.45 and Figure G.47 show the beam with the repair removed, which shows that the cracking beneath the repair shows through the repair surface.

Figure G.44: Failure at left support of Beam H-R2-F-4 (Side A)

Figure G.45: Repair removed at left support of Beam H-R2-F-4 (Side A)

Figure G.46: Failure at left support of Beam H-R2-F-4 (Side B)

Figure G.47: Repair removed at left support of Beam H-R2-F-4 (Side B)

Figure G.48: Beam H-R2-F-4 concrete keys. Top is Side A and bottom is Side B.